



TECHNISCHE
UNIVERSITÄT
DARMSTADT

Binding Proteins and Receptor Binding Domains as Sensor Elements for Biological and Artificial Nanopores

vom Fachbereich Biologie
der Technischen Universität Darmstadt

zur Erlangung des Grades

Doctor rerum naturalium

Dissertation

von

Max Bernhard

Erstgutachter: Prof. Dr. Bodo Laube

Zweitgutachter: Prof. Dr. Gerhard Thiel

Darmstadt 2021

Bernhard, Max: „ Binding Proteins and Receptor Binding Domains as Sensor Elements for Biological and Artificial Nanopores “

Darmstadt, Technische Universität Darmstadt

Jahr der Veröffentlichung der Dissertation auf TUpriints: 2021

URN: nbn:de:tuda-tuprints-85562

Tag der mündlichen Prüfung: 06.05.2021

Veröffentlicht unter CC BY-SA

International <https://creativecommons.org/licenses/>

Ehrenwörtliche Erklärung:

Ich erkläre hiermit ehrenwörtlich, dass ich die vorliegende Arbeit entsprechend den Regeln guter wissenschaftlicher Praxis selbstständig und ohne unzulässige Hilfe Dritter angefertigt habe.

Sämtliche aus fremden Quellen direkt oder indirekt übernommenen Gedanken sowie sämtliche von Anderen direkt oder indirekt übernommenen Daten, Techniken und Materialien sind als solche kenntlich gemacht. Die Arbeit wurde bisher bei keiner anderen Hochschule zu Prüfungszwecken eingereicht.

Darmstadt, den

Max Bernhard

I Summary	1
II Zusammenfassung	3
1. Introduction	5
1.1. Nanopores and Electrical Biosensors	5
1.2. Substrate Binding Proteins and Substrate Binding Domains	7
1.3. Ligand-Gated Ion Channels	9
1.4. Structure and Activation of Ionotropic Glutamate Receptors.....	9
1.5. Structure and Activation of Glycine Receptors.....	13
1.6. Aims and Outline	15
2. Studies	22
Chapter I: Thermophoretic analysis of ligand-specific conformational states of the inhibitory glycine receptor embedded in copolymer nanodiscs	23
Chapter II: The N-terminal domain of the GluN3A subunit determines the efficacy of glycine-activated NMDA receptors.....	35
Chapter III: Gating the channel pore of ionotropic glutamate receptors with bacterial substrate binding proteins: functional coupling of the ectoine binding protein EhuB to GluR0.....	45
Chapter IV: Electrical Sensing of Phosphonates by Functional Coupling of Phosphonate Binding Protein PhnD to Solid-State Nanopores	73
4. General Discussion and Conclusion	82
III Abbreviations	88
IV Acknowledgement	90
V Curriculum vitae	91

I Summary

Miniaturized electrical biosensors have become a promising tool for monitoring and analyzing biologically relevant substances by converting a biological signal into an electric current. Despite great progress in the analysis of macromolecules, the detection of small molecules that are of particular interest for medical and environmental analytics still remains a challenge. Here, the functional connection of a sensing element to an electrical switch is a bottleneck in biosensor design. Bacterial substrate binding proteins (SBPs) and ligand gated ion channels (LGICs) evolved over billions of years to recognize a variety of biologically relevant molecules with high selectivity and sensitivity. While SBPs are involved in the uptake of substances across bacterial cell membranes, LGICs mediate neuronal excitation in the central nervous system of vertebrates. The ancient binding modules of these two protein families share a conserved clamshell-like structure and entrap the ligand in their inter-lobe cleft by inducing a large conformational transition between the open- and closed- cleft states in a venus flytrap-like mechanism. In this work, i) the underlying mechanisms of ligand recognition and functional adaptability of LGICs and SBPs are investigated and exploited to ii) couple SBPs as sensor domains to biological and solid-state nanopores to build new types of electrical biosensors for the specific detection of biologically relevant small molecules.

Despite their intrinsic capability to convert a chemical signal into an electrical signal, LGICs are only now gradually being used for biosensor design since core aspects in the mechanistic understanding of ligand recognition, modulation and activation in different receptor subtypes are poorly understood. Here we investigated the structural impact and mechanism(s) of full and partial agonism in glycine receptors (GlyRs) in its native lipid environment and the modulatory role of the amino terminal domain (NTD) in GluN1/GluN3 NMDA receptor auto-inhibition after glycine binding to the low affinity GluN1 subunit. We show that the full agonist glycine and the partial agonist taurine induce different conformational transitions of the $\alpha 1$ GlyR. In addition, we show that the expression system dependent variability of agonist affinity in HEK293 cells and *Xenopus* oocytes is not mediated by an altered conformational change. Furthermore, we report that the GluN3A NTD has a major role in GluN1/GluN3A receptor regulation by reducing the efficacy of glycine-dependent receptor activation by agonist-evoked auto-inhibition. This effect is possibly mediated by the subunit interface and the NTD-LBD linkers of the GluN3A NTD. These insights into the conformational changes and structural adaptability have been further exploited to use bacterial SBPs and SBDs from LGICs as a molecule detector when connected

to an electrical switch by coupling the ectoine binding protein EhuB to the channel pore of the ionotropic glutamate receptor GluR0 to design receptor-based biosensor and by coupling the phosphonate binding protein PhnD inside a single track-etched solid-state nanopore that combines the high affinity and selectivity of SBPs with the robustness of artificial nanopores. These new classes of electrical biosensors are characterized by a high ligand-affinity and specificity with concentration-dependent changes in the (nanopore) current after Ligand binding.

The results in this work provide an excellent foundation for the use of SBPs and LGICs as sensor domains to develop new classes of electric biosensors with high specificity and affinity for detection of biologically relevant small molecules. Moreover, our approaches and insights into ligand recognition and modulation enhance the repertoire of biophysical methods and may deepen the understanding of the functions of LGICs at the molecular, synaptic and systemic level.

II Zusammenfassung

Miniaturisierte elektrische Biosensoren sind zu einem vielversprechenden Werkzeug für die Überwachung und Analyse biologisch relevanter Substanzen geworden, indem sie ein biologisches Signal in einen elektrischen Strom konvertieren. Trotz großer Fortschritte bei der Analyse von Makromolekülen bleibt die Detektion von niedermolekularen Verbindungen, die für die Medizin- und Umweltanalytik von besonderem Interesse sind, eine Herausforderung. Die funktionelle Kopplung eines Sensorelements an einen elektrischen Schalter ist hierbei ein Knackpunkt im Biosensoren-Design. Bakterielle Substratbindeproteine (SBP) und Liganden-gesteuerte Ionenkanäle (LGICs) haben sich über Milliarden von Jahren entwickelt, um eine Vielzahl biologisch relevanter Moleküle mit hoher Selektivität und Sensitivität zu erkennen. Während SBP am Transport von Substanzen durch bakterielle Zellmembranen beteiligt sind, vermitteln LGICs die neuronale Erregung im zentralen Nervensystem von Wirbeltieren. Die archaischen Bindungsmodule beider Proteinfamilien teilen eine konservierte muschelartige Struktur; der Ligand wird zwischen den zwei Subdomänen gebunden und löst einen großen Konformationsübergang zwischen dem offenen und geschlossenen Zustand in einem Venusfliegenfallen-ähnlichen Mechanismus aus. In dieser Arbeit werden i) die zugrundeliegenden Mechanismen der Ligandenerkennung und die funktionelle Anpassungsfähigkeit von LGICs und SBPs untersucht und ausgenutzt um ii) SBP an biologische und artifizielle Nanoporen zu koppeln mit dem Ziel neuartige elektrische Biosensoren für den spezifischen Nachweis von biologisch relevanten Substanzen zu entwickeln.

Trotz ihrer intrinsischen Fähigkeit ein chemisches Signal in ein elektrisches Signal umzuwandeln, werden LGICs erst allmählich für das Design von Biosensoren genutzt, da Schlüsselaspekte im mechanistischen Verständnis der Ligandenbindung, -modulation und Rezeptoraktivierung in verschiedenen Rezeptorsubtypen unzureichend verstanden sind. In dieser Arbeit untersuchten wir die strukturellen Auswirkungen und die zugrundeliegenden Aktivierungsmechanismen von vollen und partiellen Agonisten in Glycinrezeptoren (GlyRs) in ihrer nativen Lipidumgebung, sowie die Funktion der aminoterminalen Domäne (NTD) in der GluN1/GluN3 NMDA-Rezeptor Autoinhibition nach Glycinbindung an die GluN1-Untereinheit. Wir können zeigen, dass der volle Agonist Glycin und der partielle Agonist Taurin unterschiedliche Konformationsübergänge im $\alpha 1$ GlyR induzieren. Darüber hinaus legen wir dar, dass die vom Expressionssystem abhängige Variabilität der Agonistenaffinität in HEK293-Zellen und *Xenopus* Oozyten nicht durch eine veränderte

Konformationsänderung vermittelt wird. Des Weiteren zeigen wir, dass die GluN3A-NTD eine wichtige Rolle in der Regulation von GluN1/GluN3A NMDA-Rezeptor Subtypen spielt, indem sie die Wirksamkeit der Glycin-abhängigen Rezeptoraktivierung durch Agonisten- ausgelöste Autoinhibition reduziert. Dieser Effekt wird möglicherweise durch das Subunit-Interface und den NTD-LBD-Linker der GluN3A-NTD vermittelt.

Die vertieften Erkenntnisse über die Konformationsänderungen und die strukturelle Anpassungsfähigkeit dieser Bindedomänen wurden weiter genutzt, um bakterielle SBP und LGIC SBD in Kombination mit einem elektrischen Schalter als Moleküldetektor zu verwenden. Hierfür wurde das Ectoin-Bindeprotein EhuB an die Kanalpore des ionotropen Glutamatrezeptors GluR0 gekoppelt, um einen rezeptorbasierten Biosensor zu konstruieren, sowie das Phosphonatbindeprotein PhnD innerhalb von einzelnen Festkörper-Nanoporen gekoppelt, mit dem Ziel die hohe Affinität und Selektivität von SBPs mit der Robustheit von künstlichen Nanoporen zu kombinieren. Diese neuen Biosensor-Klassen zeichnen sich durch eine hohe Ligandenaffinität und Spezifität, als auch durch eine konzentrationsabhängige Änderung des (Nanoporen-)Stroms nach Ligandenbindung aus.

Die Ergebnisse dieser Arbeit bieten eine profunde Grundlage um SBP und LGIC als Sensordomänen für die Entwicklung neuartiger elektrischer Biosensoren mit hoher Spezifität und Affinität für den Nachweis biologisch relevanter Moleküle zu nutzen. Darüber hinaus erweitern die hier gezeigten Ansätze und Erkenntnisse zur Ligandenerkennung und -Rezeptormodulation das Repertoire biophysikalischer Methoden und könnte das Verständnis der Funktionen von LGIC auf molekularer, synaptischer und systemischer Ebene vertiefen.

1. Introduction

The specific recognition of ligands by specialized proteins is a key feature for various biological functions in all domains of life and is associated with signal transduction, substrate transport and gene regulation. A common representative of ancient binding modules are clamshell-like domains that can be found in prokaryotes as well as metazoan organisms. These binding domains simply function by entrapping the ligand in their inter-lobe cleft, inducing a large conformational transitions between the open- and closed- states¹⁻³. Two examples of these specialized protein domains are substrate binding proteins (SBPs) and ligand gated ion channels (LGICs). Bacterial SBPs are mainly involved in the uptake and transport of substances across the cell membrane whereas LGICs are involved in neuronal excitation by converting a chemical signal into an electrical signal. Here, the extracellular binding domains of LGICs are responsible for ligand recognition. Both protein families evolved over billions of years to recognize biologically relevant molecules with a high selectivity and sensitivity. Therefore, due to their binding characteristics, the ligand induced conformational change and high structural adaptability, SBPs and substrate binding domains (SBDs) of LGICs could be exploited in the design of new membrane receptors and sensor domains for the development of biosensors for medical diagnostic and environmental analysis⁴.

1.1. Nanopores and Electrical Biosensors

Cells contain a wide range of different types of nanopores, which control the passive or active transport of ions and molecules across the cell membranes. Some nanopores such as ion channels and receptors are highly selective pores and are gated by various external stimuli and ligands⁵, whereas other nanopores like β -barrel pore forming toxins promote the unselective transport of ions and small molecules⁶. In the last decade, several nanopore systems that mimic the characteristics of ion channels have emerged as powerful tools for the label-free analysis of biological relevant molecules and physicochemical conditions. Depending on the used material and approach, nanopores can range between a few nanometres to several micrometres in diameter⁷⁻⁹. In principle, the signal is given by the ion flux through individual nanopores under an externally applied voltage and molecules can be detected by the current change through the nanopore when they enter or interact with the pore surface^{9,10}. Previous work focused on the detection of single-(macro)molecules¹¹⁻¹⁴, DNA sequencing¹⁵, recognition of physicochemical stimuli like changes in pH, temperature

and light¹⁶⁻¹⁸, as well as the investigation of chemical reaction mechanisms¹⁹. A key step in the design and miniaturization is thereby the conversion of a biological signal into an electrical current. Nevertheless, beside the stunning progress in this field, the development and coupling of specific molecule detectors to an electric switch is still a major challenge. Nanopores can be fabricated in different materials and are further divided into (i) artificial solid-state nanopores, (ii) biological nanopores and (iii) hybrid-nanopores that combine solid-state nanopores with biological units. Solid-state nanopores can be fabricated in different insulating materials such as polymers (PET, PC, PI), graphene, glass (borosilicate or quartz) and other silicon-based materials (SiN, SiO₂). They have the advantage of high stability, a variable and readily controllable pore size and material thickness, as well as the possibility to chemically modify their surface properties. In addition, solid-state nanopores can be directly integrated into miniaturized electronic devices and arrays^{8,20}. So far, various routes are described in the fabrication of pores with nanometre dimensions. In the etching method, the pore is simply etched into the insulating layer, as for instance in glass slides²¹. The more advanced track-etching technique uses multiple or a single high-energy heavy metal ion to create a defect path by shooting the accelerated ions through the insulating polymer layer. This latent track is further used to guide the etching-process preferentially along the damaged pathway. The size and shape of the nanopores can be adjusted by the etching time, temperature and solution concentration. This allows the fabrication of symmetrical cylindrical-shaped or asymmetrical conical-shaped pores with diameters down to 2 nm. Importantly, the pore formation can be monitored through the ion current across the membrane during the etching process²²⁻²⁴. Further techniques like the ion-beam sculpting technique use a focused ion-beam to mill single nanometre sized pores into the insulating membrane⁷. However, unmodified solid-state nanopores lack the selectivity of proteins and protein domains and are unresponsiveness against stimuli. Further, the reproducible fabrication of artificial pores is still a challenge. In contrast, biological nanopores can be reproducibly manufactured and engineered with atomic level precision. Porins, such as α -haemolysin or ClyA, are the most frequently used biological nanopores in single molecule analysis and have been used for single molecule detection and DNA-sequencing^{11,15}. They assemble as multimers forming barrel-like pore structure with pore-sizes ranging between 1 – 2 nm⁹. Other biological nanopores and biosensors use ion channels and receptors for small molecule and light detection by coupling sensor domains to ion channels or manipulating the ligand binding domain^{14,25-27}. Nevertheless, biological nanopores exhibit a number of disadvantages such as a fixed size and have limited stability in response to changes in

external parameters like pH, temperature, salt concentration, and mechanical stress. Further, most biological nanopores or sensors are membrane proteins that must be embedded into a lipid bilayer. The combination of proteins and protein domains as sensor element to solid-state nanopores, so called hybrid nanopore systems, combine the advantages of both systems and are widely used for the sensing of large macromolecules such as antibodies, toxins and other proteins^{13,28,29}.

1.2. Substrate Binding Proteins and Substrate Binding Domains

Substrate binding proteins (SBPs) and substrate binding domains (SBDs) represent a widely distributed protein superfamily in pro- and eukaryotes that are characterized by a common globular clamshell-like structure^{1,3,30}. In Prokaryotes, they are primarily part of ABC transporters and facilitate the uptake of various substances, including amino acids, saccharides, ions and a variety of organic compounds³⁰⁻³². SBDs are also associated with other membrane protein complexes (Fig. 1) and are part of prokaryotic secondary tripartite ATP-independent periplasmic transporters (TRAP transporters)³³, tripartite tricarboxylate transporters (TTT)³⁴ as well as two-component systems that are involved in signal transduction³⁵. Furthermore, SBDs serve as the extracellular ligand binding domain in eukaryotic ionotropic (ion channel-containing) and metabotropic (G protein-coupled) glutamate receptors^{1,36,37}. In addition, SBDs are part of prokaryotic gene regulators³⁸. Although SBPs and SBDs often display a low sequence identity <20%, their three-

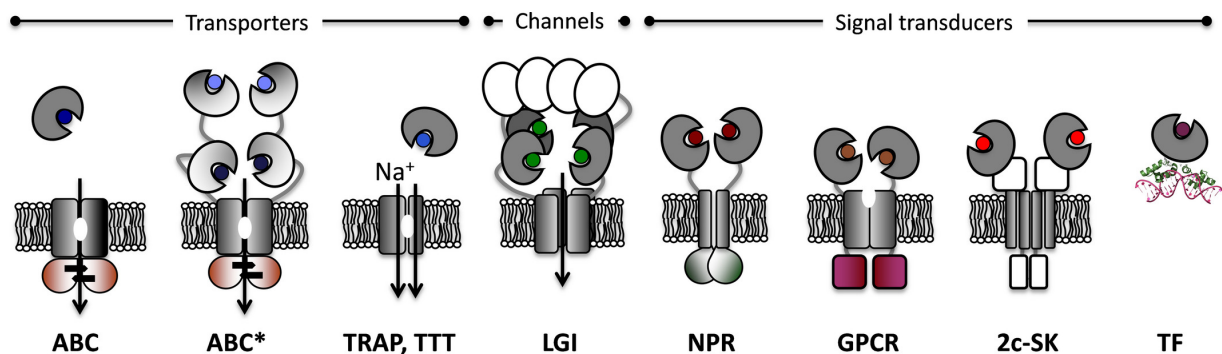


Figure 1. Overview of pro- and eukaryotic SBPs and SBDs associated with membrane proteins. ABC and ABC*: bacterial ABC importer; TRAP: secondary tripartite ATP-independent periplasmic transports; TTT: tripartite tricarboxylate transporters; LGI: ligand gated ion channels with the cytoplasmatic ATD (white) and LBD (grey); NPR: Natriuretic peptide receptors; GPCR: G-protein coupled receptors include metabotropic glutamate receptors with the cytoplasmatic binding domain; 2c-SK: two-component sensor kinase; TF: transcription factors. SBPs and SBDs are represented in grey and ligands are indicated with a small circle (different colours). Figure is adapted from Scheepers et al., 2016³⁹.

dimensional structures are highly conserved. They consist of two lobes (D1 and D2) that are tethered by a flexible hinge region, with the ligand-binding site buried between the two subdomains. Based on the topology of the central β -sheets, SBPs can be divided into two classes (Fig. 2a) with a sheet topology of $\beta_2\beta_1\beta_3\beta_4\beta_5$ for class I SBPs and for $\beta_2\beta_1\beta_3\beta_n\beta_4$ class II SBPs⁴⁰. Recent classifications based on more general three-dimensional features subdivide SBPs and SBDs into seven clusters^{3,39}. Despite their diverse biological functions and the variety of recognized ligands, these ancient protein modules share the same mode of ligand binding. SBPs and SBDs can adopt two major conformations: an open unliganded and a closed ligand-bound conformation (Fig. 2b). In the absence of a ligand the two lobes are separated from each other (open clamshell) and can flexibly rotate around the hinge. Ligand binding takes place in the inter-lobe cleft and stabilizes the closed conformation, thus inducing a large conformational transition around the hinge by rotating the D1 and D2 lobes towards each other⁴¹⁻⁴³. Structural analysis revealed that the closing-angle upon ligand binding differs dramatically among SBPs, varying from small domain closures of 35° ⁴⁴ to big transitions up to 70° ⁴⁵. This process of clamshell closure is termed the ‘Venus Fly-trap’ mechanism¹.

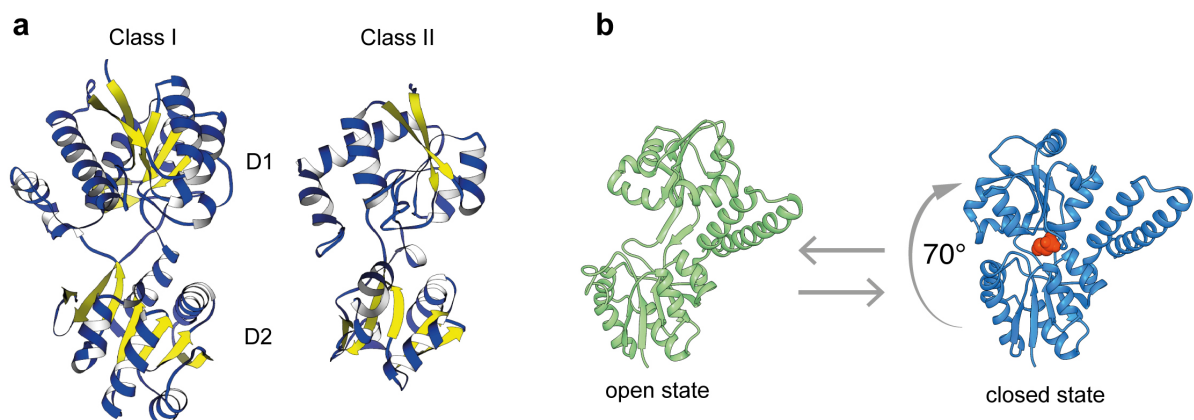


Figure 2. Structure and binding mechanism of SBPs and SBDs. **a** Structural classification according to Fukami-Kobayashi et al., 1999. Class I SBPs (left, PDB ID 2liv) are characterized by a β -sheet topology of $\beta_2\beta_1\beta_3\beta_4\beta_5$. Class III SBPs (right, PDB ID 2lao) are characterized by a β -sheet topology of $\beta_2\beta_1\beta_3\beta_n\beta_4$. **b** Schematic binding mechanism of SBPs, displaying the open, ligand-free (green; PDB 3S4U) and closed, ligand-bound conformation (blue; PDB 3P7I). Ligand (red) binding takes place between the interface of the two lobed subdomains and induces a large conformational change by rotating the lower domain towards the upper domain. Figure b is adapted from Bernhard et al., 2020¹⁰.

1.3. Ligand-Gated Ion Channels

Ligand-gated ion channels (LGICs) are present in all metazoans^{46,47} and homologues can be found in plants⁴⁸ and bacteria^{49,50}. In vertebrates, they mediate fast excitatory and inhibitory synaptic neurotransmission in the central nervous system and are crucial for brain function, sensation and locomotion^{51,52}. Dysfunctions within LGICs are further associated with neuronal diseases^{51,53}, rendering them an important target for therapeutics⁵⁴. Based on their structural characteristics, LGICs can be subdivided into three major classes: ionotropic glutamate receptors (iGluRs), Cys-loop receptors (CLRs) and ATP-binding receptors and acid-sensing receptors (P2XRs). Despite their structural, functional and pharmacological differences, all LGICs are composed of an extracellular ligand-binding domain that is coupled to a transmembrane spanning ion channel. They control the ion flux through the plasma membrane by converting a chemical signal into an electrical signal upon the binding of a wide range of ligands (neurotransmitters), connecting neurotransmitter signalling or exogenous stimuli to cell excitation⁴⁷. The binding to the orthostatic binding site is always associated with a conformational change that subsequently results in channel gating. The following subchapters will mainly focus on the structure and activation mechanism of AMPA-, NMDA- and glycine receptors that are further used in this work.

1.4. Structure and Activation of Ionotropic Glutamate Receptors

iGluRs mediate the majority of excitatory neurotransmission in the central nervous system and are associated in all aspects of neuronal development and function, behaviour and cognition⁵¹. The iGluR family includes four major subtypes with several subunits: AMPA- (GluA1-4), kainite- (GluK1-5), NMDA- (GluN1, GluN2A-D and GluN3A-B) and δ -receptors (GluD1-2). As their name indicates, all iGluRs are activated by the neurotransmitter glutamate, with the exception of NMDA receptors, which require the simultaneous binding of glutamate and glycine for activation. In addition, NMDA receptors composed of GluN1 and GluN3 subunits are activated by glycine alone. Whereas AMPA- and kainite receptors assemble as homo- and heterotetramers, NMDA receptors function as an assembly of two GluN1 with either two GluN2 or GluN3 or one GluN2 and GluN3 subunit. Despite their diverse pharmacological properties, kinetics and physiological functions, all iGluRs share a common modular architecture (Fig. 3a) and are composed of four domains⁵⁵⁻⁵⁷. (i) The amino-terminal domain (ATD) plays a fundamental role in subtype specific receptor assembly, trafficking^{58,59} and is associated in allosteric modulation in NMDA receptors^{60,61}. Further, the

ATD displays a typical clamshell-like structure that is homologous to bacterial class I SBPs³. (ii) The LBD is responsible for agonist and antagonist recognition. Each LBD has a typical clamshell-like bi-lobed structure and is comprised of two polypeptide stretches (D1/S1 and D2/S2), which are connected by three linkers (S1-M1, M3-S2 and S2-M4) to the transmembrane domain^{36,55}. Further, based on their primary sequence and general topology, iGluR LBDs are homologous to bacterial class II SBPs^{1,62}. (iii) The TMD of each subunit is composed of three transmembrane helices (M1, M3, M4) and a central pore loop (M2), forming the ion channel. (iv) The intracellular C-terminal domain (CTD) is involved in synaptic localization, trafficking and receptor modulation⁶³. Based on their common modular design, sequence and topological similarities, it is thought that simple iGluRs, such as GluR0, arose from the fusion of SBP and potassium channels^{49,64–66}. The general structure of tetrameric iGluRs has a characteristic Y-shape with a unique four-fold rotational symmetry in the TMD layer and a two-fold rotational symmetry in the extracellular domains (Fig. 3b). The individual ATDs and LBDs form two pairs of dimers each and swap between the ATD (AB and CD) and LBD dimers (AD and BC) in a back-to-back arrangement⁵⁵.

The term gating in iGluRs refers to a series of conformational changes upon ligand binding to open or close the channel pore and affect the adopted functional states. iGluR gating comprises receptor activation, desensitization and deactivation and can be described by a simple kinetic model that includes a closed unliganded state, a pre-activated liganded state, an open, ligand-bound state and a desensitized ligand-bound state (Fig. 4). In the absence of a ligand, the receptor lingers in a resting, nonconductive state with an open unliganded LBD and a closed channel pore. Ligand binding to the LBD induces the closure of the clamshell, entrapping the ligand between the D1 and D2 domain, placing the receptor in a pre-activated state with a closed channel pore. The pre-activated state is a turning point at which the receptor can either convert to the open state or adopt a ligand-bound but non-conducting state (desensitized). Since the transition between the pre-activated and the open state is much faster than the transition between pre-activated and desensitized state, most of the receptors are activated after ligand binding. However, the general equilibrium of the agonist-bound conformations lies strongly on the desensitized state that the majority of the receptors undergo desensitization after activation^{63,67}. For receptor activation, the formation and maintenance of the back-to-back dimer arrangement by the D1-D1 interface is crucial to transduce the conformational change of the LBD after ligand binding towards the ion channel. The adherence of two adjacent LBDs allows the separation of the D2 lobes from each other. This energy can be further transferred by the linkers towards the TMD to open

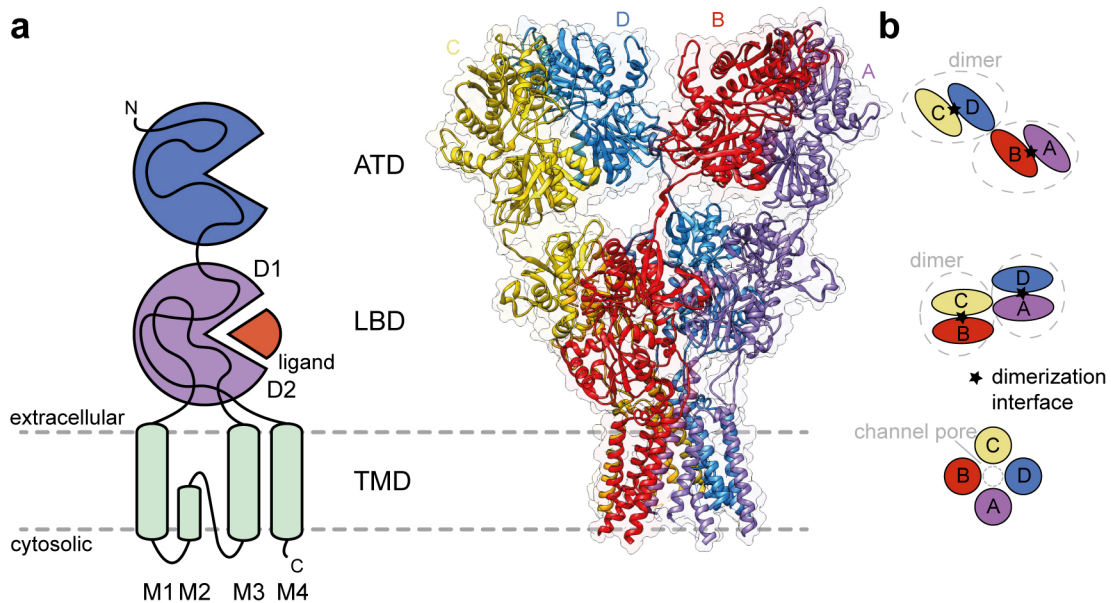


Figure 3. General structure and subunit arrangement of iGluRs. **a** Topology of an individual iGluR subunit (right), composed of an extracellular ATD, an extracellular LBD and the transmembrane spanning TMD. Crystal structure of the GluA2 receptor (3kg2) in a closed state. The individual subunits (A-D) are coloured differently. **b** Subunit arrangement of the ATD-, LBD- and TMD-layers. The ATD-, and LBD-layer showing a local 2-fold symmetry, whereas the TMD has a local 4-fold symmetry. Local dimerization interfaces are indicated with black asterisk, grey ovals indicate dimer pairs in the ATD and LBD, as well as the ion channel pore in the TMD.

the ion channel for conductance^{55,68,69}. In contrast, the same force that is created by the separation of the D2 lobes can lead to a rearrangement or rupture of the dimerization interface. This allows the channel pore to adopt a closed conformation that disengages the ligand induced clamshell closure of the LBD from channel gating. It is notable that the receptor cannot be reactivated in the desensitized state and must undergo substantial rearrangements within the LBD layer to transit into the pre-activated state^{57,68,70}. After the agonist is removed from the agonist-bound state, the receptor undergoes recovery to adopt the resting, closed state, where it can be activated again.

In addition, NMDA receptors display several unique features that distinguish them from AMPA and kainate receptors, including a voltage dependent block by extracellular Mg^{2+} , a high permeability to Ca^{2+} and the requirement for binding a co-ligand, glutamate and glycine (or D-serine) for channel activation⁵¹. In contrast to other iGluRs, the ATDs (also called amino-terminal domain or NTD) of NMDA receptors provide binding sites for allosteric modulators like Zn^{2+} or ifenprodil^{71,72} and are strongly involved in modulating NMDA receptor function by influencing the agonist potency, open probability and deactivation time⁷³⁻⁷⁵. The ATDs associate in a unique back-to-side heterodimer fashion that are formed

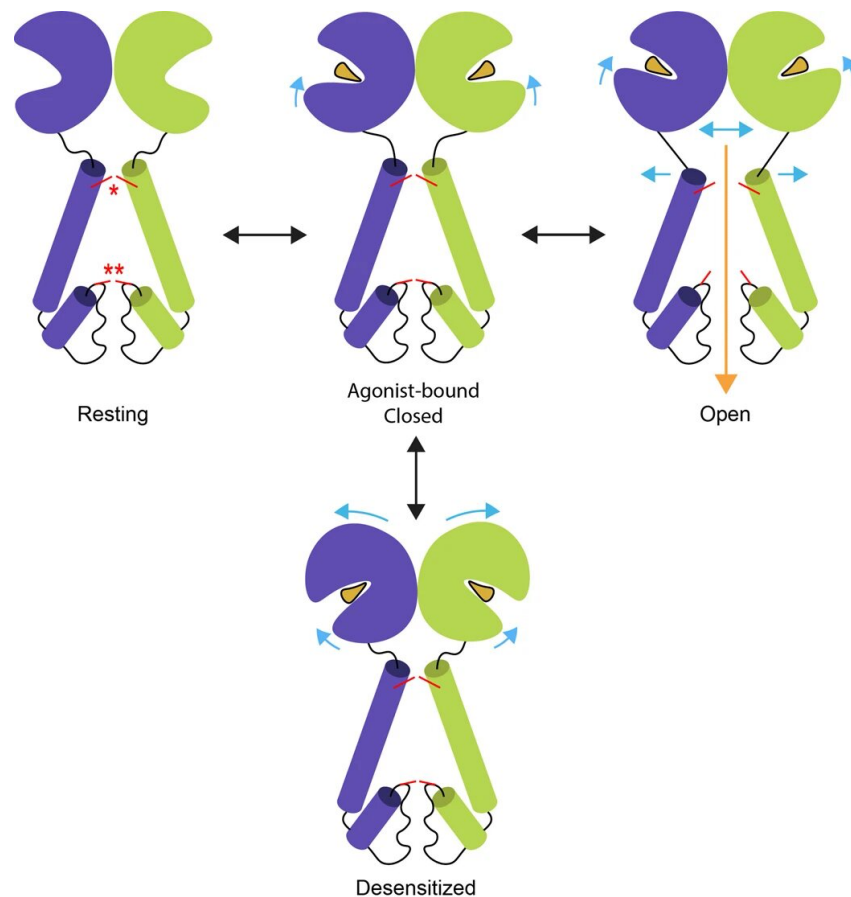


Figure 4. General gating mechanism of iGluRs. iGluRs can adopt four major conformational states: resting state with a unliganded open LBD and a closed ion channel; pre-activated state (Agonist-bound and closed); open state with a ligand bound LBD and an open ion channel; desensitized state with a ligand bound LBD and a closed channel pore. In the absence of a ligand, the receptor resides in a resting state, where the LBD clamshell is maximally open and the channel pore is closed. Binding of a ligand to the LBD induces a closure of the clamshell structure, leading to a transition to the pre-activated state, where the ion channel is still closed. Maximal closure of the LBD clamshell leads to either transferring the force towards the TMD that lead to ion channel opening or a rupture of the D1-D1 LBD dimerization interface and a desensitization of the receptor. In the desensitized state, the receptor has a maximal closed LBD while the channel pore is closed. Black arrows indicate transitions between the different receptor states and conformational changes within the receptor domains are indicated with blue arrows. The ion channel gates are indicated with a red line and the ligand is displayed as a red triangle. Figure is adapted from Twomey et al., 2017⁷⁶.

exclusively by the upper lobes and they display extended intra-subunit interactions between the ATDs and the upper lobes of the LBDs^{56,77}. Although not much is known about how the ATD controls receptor function, the underlying mechanism presumably involves allosteric intra- and inter-subunit interactions between the ATDs and the LBDs that influences the LBD configurations and thereby impact channel activation. However, the activation mechanism itself is similar to AMPA and kainite receptors and binding of glutamate and glycine to the

back-to-back arranged LBDs leads to a closure of the LBDs that provides sufficient conformational strain to initiate channel opening^{56,71,78,79}.

1.5. Structure and Activation of Glycine Receptors

Glycine receptors (GlyRs) belong to the superfamily of pentameric ligand-gated ion channels and mediate, together with GABA receptors, the majority of fast inhibitory neurotransmission in the central nervous system⁵². They are implicated in several functional aspects of sensation and locomotion including audition and vision⁵². Dysfunctions within the GlyR family are further associated with neuronal diseases like hyperekplexia^{52,80} and forms of epilepsy⁸¹. GlyRs assemble as homopentamers of α -subunits (α 1-4) or heteropentamers, containing both α - and β -subunits⁸² and are composed of an extracellular, orthosteric ligand binding site (ECD), a transmembrane spanning ion-channel (TMD) consisting of four α -helices (M1-4, with M2 lining the channel-pore and forming the upper and lower gate) and an intracellular domain (ICD) with variable length⁸³ (Fig. 5). However, although iGluRs and glycine receptors both entrap the ligand in their extracellular ligand bound site, closure of the binding domains occurs in different ways. The ligand-binding site of GlyRs is formed between the ECDs of two adjacent subunits by the C loops of the principal subunit and three

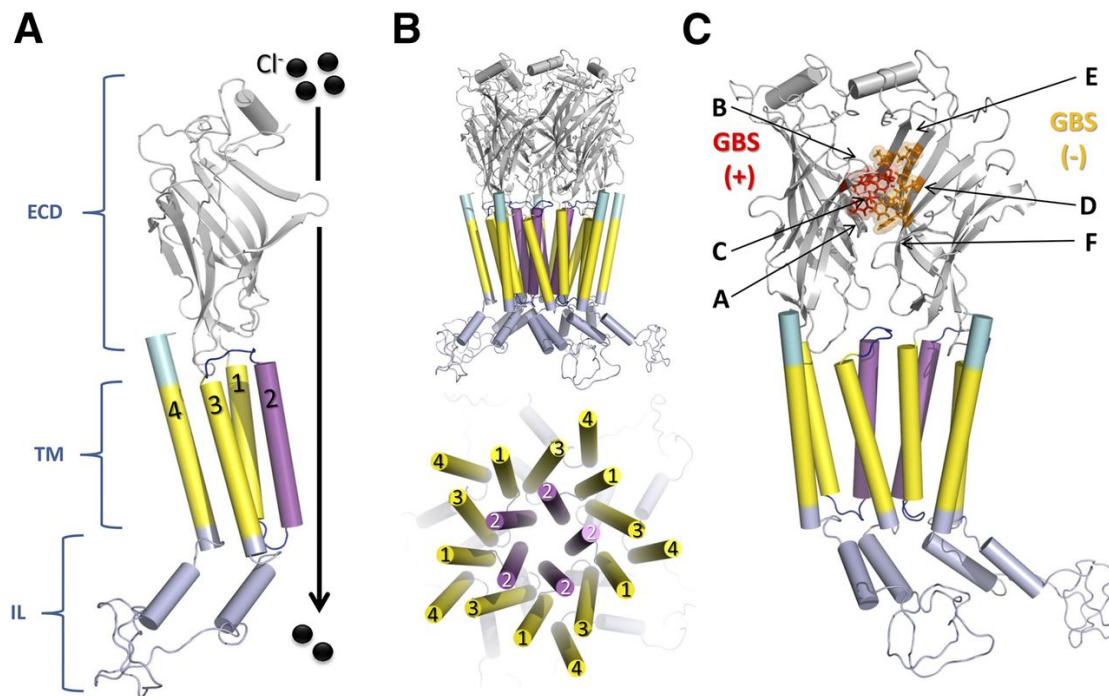


Figure 5. Architecture of pentameric GlyRs. **a** Subunits are composed of a barrel-shaped extracellular domain (ECD) that bind the ligand, a transmembrane domain (TMD) that form the ion pore, and an intracellular domain (ICD). **b** pentameric arrangement of the GlyR. **c** Ligand binding site that is located between the C loop (A-C) and β -barrels (D-F) of two adjacent subunits. Figure is adapted from Burgos et al., 2016⁸⁴.

β -strands of the complementary subunit^{83,85}. In the absence of a ligand, the receptor remains in an apo state, where the channel pore is closed (Fig. 6). Agonist binding closes the C loop thumb and induces an anticlockwise contraction of the ECD around the central pore axis. This promotes the receptor transition from the apo state to the closed state, where the ligand is bound and the channel is closed. This partially activated receptor state is also referred to as ‘flipped’⁸⁶ or ‘primed’⁸⁷ state. The rotation within the ECD layer is transmitted towards the TMD, to open the pore in an iris-like mechanism, where the upper part of TM2 rotates outward to open the upper channel-gate and subsequently open the channel pore (active-state)⁸³. Thereby, the activation efficiency of the receptor can differ between different ligands. Agonists with low efficiency are termed partial agonists. Recent findings suggest that partial agonism arises in the ECD, leading to a shift of the equilibrium towards the pre-activated state. However, the underlying molecular mechanism is still unclear^{47,86,88}. After activation, prolonged binding of the agonist induces a further transition of the receptor from the active state into the desensitized state by closing the lower pore gate^{83,89}.

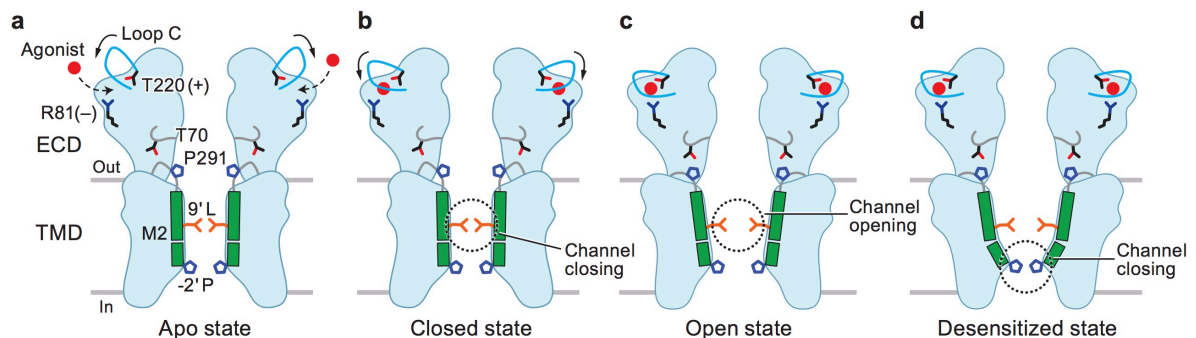


Figure 6. Schematic gating mechanism of GlyRs. After Ligand binding at the ECD, the receptor transit from the apo state with a unliganded ECD and a closed channel pore, to the intermediate closed state with a contracted ECD and a closed channel pore. The ECD further promotes the transition from the closed state to the ion conducting open state by an outward rotation of the TMD and a subsequent opening of the upper channel gate (orange Y). Prolonged agonist binding leads to a closure of the lower channel pore gate (blue polygon) and receptor desensitization. Agonist is displayed as a red circle and important residues for receptor gating as well as helix M2 are highlighted. Figure is adapted from Jie Yu et al., 2020⁹⁰.

1.6. Aims and Outline

In the last decade, miniaturized electrical biosensors have become promising tools for analysing and monitoring biologically relevant substances^{8,9}. Thereby, the conversion of biological signals into an electrical current enables real-time, label-free assay systems with a high signal to noise ratio. Despite great progress in the analysis of macromolecules like DNA or peptides, the detection of small molecules, that are in particular interest for medical and environmental analysis, lag behind⁸. Hereby, the functional connection of a sensing element to an electrical switch remains a bottleneck in biosensor design. Specialized proteins like SBPs or LGICs can be considered to function as natural recognition elements, since the highly specific and affine binding of ligands is associated with a large conformational transition. Furthermore, LGICs combine the natural ability to directly convert a biological signal (neurotransmitter) into an electrical signal that is proportional to its ligand concentration. However, although structural and functional studies provide a detailed view about the binding and activation mechanism, as well as modulation in some LGIC subtypes, such as AMPA-, kainite- or acetylcholine-receptors⁴⁷, the underlying mechanisms in physiological and therapeutic relevant NMDA- and glycine receptors remain unclear.

In this study, we investigated the potential of ligand-mediated conformational changes in bacterial SBPs and LGIC binding domains to design new classes of biosensors and receptors with new binding properties. Therefore, we studied i) the underlying mechanisms of full- and partial agonism in GlyRs and ii) the modulatory role of the NTDs in the auto-inhibition of GluN1/GluN3 NMDARs after glycine binding to the low-affinity GluN1.

To exploit SBPs and the SBDs of LGICs as natural building blocks in biosensor design, we iii) investigated the functional compatibility of iGluRs and SBPs by replacing an iGluR LBD with a structure homologue bacterial SBP, to design an artificial receptor with new binding properties. Furthermore, we iv) tethered SBPs directly into solid-state nanopores to construct a sensing system that combine both, the selectivity and sensitivity of biological units with the robustness of solid-state nanopores.

To address these questions, the thesis is divided into four chapters. Every chapter has been published in a peer reviewed journal or is available as a preprint.

Chapter I presents a new approach to study the structural impact of full and partial agonists in GlyRs in their native lipid environment using SMA-copolymer nanodiscs and microscale thermophoresis. Here, we investigate different conformational transitions upon the binding

of glycine and taurine. Furthermore, we analyse the conformational impact on the variability of agonist efficiency observed in HEK293 cells and *Xenopus* oocytes.

Chapter II presents the examination of the modulatory role of the NTD in glycinergic GluN1/GluN3 subtype NMDA receptors that are, in contrast to other iGluRs and NMDA receptors, only activated by glycine. Remarkably, glycine binding to the high affinity GluN3 subunit promotes activation whereas glycine binding to the low affinity GluN1 subunit inhibits the maximal inducible receptor current. By deleting the NTD of the GluN1 and GluN3A subunit and crosslinking the NTD inter-subunit interface, the modulatory impact of the GluN3A NTD in GluN1/GluN3 receptor function is investigated.

Chapter III presents a study to investigate the functional compatibility between SBPs and iGluRs by replacing the LBD of GluR0 with the bacterial ectoine SBP EhuB. Here, we analyse basic aspects of the gating mechanism and modular design of iGluRs, as well as the molecular preconditions that facilitated the evolution of iGluRs from SBPs and potassium channels. Further, we examine the ability of SBPs to serve as molecular recognition element in a new class of receptor inspired biosensors.

Chapter IV presents a proof-of-principle study that SBPs can be directly incorporated into solid-state nanopores as a new approach to design hybrid electrical biosensors. Here, the phosphonate binding protein PhnD is tethered via primary amines to the reactive NHS groups of P(DMAA-co-NMAS) polymers into track-etched single solid-state nanopores.

1. Felder, C. B., Graul, R. C., Lee, a Y., Merkle, H. P. & Sadee, W. The Venus flytrap of periplasmic binding proteins: an ancient protein module present in multiple drug receptors. *AAPS PharmSci* **1**, 7–26 (1999).
2. Acher, F. C. & Bertrand, H.-O. Amino acid recognition by Venus flytrap domains is encoded in an 8-residue motif. *Biopolymers* **80**, 357–366 (2005).
3. Berntsson, R. P. a, Smits, S. H. J., Schmitt, L., Slotboom, D. J. & Poolman, B. A structural classification of substrate-binding proteins. *FEBS Lett.* **584**, 2606–2617 (2010).
4. Dwyer, M. a. & Hellinga, H. W. Periplasmic binding proteins: A versatile superfamily for protein engineering. *Curr. Opin. Struct. Biol.* **14**, 495–504 (2004).
5. Zheng, J. & Trudeau, M. C. *Handbook of Ion Channels*. (CRC Press, 2015).
6. Song, L. *et al.* Structure of staphylococcal α -hemolysin, a heptameric transmembrane pore. *Science (80-.)*. **274**, 1859–1866 (1996).
7. Li, J. *et al.* Ion-beam sculpting at nanometre length scales. *Nature* **412**, 166–169 (2001).
8. Dekker, C., Article, R. & Dekker, C. Solid-state nanopores. *Nat. Nanotechnol.* **2**, 209–215 (2007).
9. Willems, K., Meervelt, V. Van, Wloka, C., Maglia, G. & Maglia, G. Single-molecule nanopore enzymology. *Philos. Trans. R. Soc. B-BIOLOGICAL Sci.* **372**, (2017).
10. Bernhard, M., Diefenbach, M., Biesalski, M. & Laube, B. Electrical Sensing of Phosphonates by Functional Coupling of Phosphonate Binding Protein PhnD to Solid-State Nanopores. *ACS Sensors* **5**, 234–241 Article (2020).
11. Soskine, M., Biesemans, A. & Maglia, G. Single-molecule analyte recognition with ClyA nanopores equipped with internal protein adaptors. *J. Am. Chem. Soc.* **137**, 5793–5797 (2015).
12. Galenkamp, N. S., Soskine, M., Hermans, J., Wloka, C. & Maglia, G. Direct electrical quantification of glucose and asparagine from bodily fluids using nanopores. *Nat. Commun.* **9**, 1–8 (2018).
13. Yusko, E. C. *et al.* nanopores with bio-inspired fluid walls. **6**, 253–260 (2011).
14. Moreau, C. J., Dupuis, J. P., Revilloud, J., Arumugam, K. & Vivaudou, M. Coupling ion channels to receptors for biomolecule sensing. *Nat. Nanotechnol.* **3**, 620–625 (2008).
15. Venkatesan, B. M. & Bashir, R. Nanopore sensors for nucleic acid analysis. *Nat. Publ. Gr.* **6**, 615–624 (2011).
16. Lepoitevin, M. *et al.* Fast and reversible functionalization of a single nanopore based on layer-by-layer polyelectrolyte self-assembly for tuning current rectification and designing sensors. *RSC Adv.* **6**, 32228–32233 (2016).
17. Hou, X. *et al.* A biomimetic asymmetric responsive single nanochannel. *J. Am. Chem. Soc.* **132**, 11736–11742 (2010).
18. Zhang, M. *et al.* Light and pH cooperative nanofluidic diode using a spiropyran-functionalized single nanochannel. *Adv. Mater.* **24**, 2424–2428 (2012).
19. Luchian, T., Shin, S.-H. & Bayley, H. Single-Molecule Covalent Chemistry with Spatially Separated Reactants. *Angew. Chemie Int. Ed.* **42**, 3766–3771 (2003).
20. Lepoitevin, M., Ma, T., Bechelany, M., Janot, J. M. & Balme, S. Functionalization of single solid state nanopores to mimic biological ion channels: A review. *Adv. Colloid Interface Sci.* **250**, 195–213 (2017).
21. Schmidt, C., Mayer, M. & Vogel, H. A chip-based biosensor for the functional analysis of single ion channels. *Angew. Chemie - Int. Ed.* **39**, 3137–3140 (2000).
22. Siwy, Z. & Fuliński, A. Fabrication of a Synthetic Nanopore Ion Pump. *Phys. Rev. Lett.* **89**, (2002).

23. Apel, P. Track etching technique in membrane technology. in *Radiation Measurements* **34**, 559–566 (2001).
24. Apel, P. Y. *et al.* Factors determining pore shape in polycarbonate track membranes. *Colloid J.* **66**, 649–656 (2004).
25. Janovjak, H., Szobota, S., Wyart, C., Trauner, D. & Isacoff, E. Y. A light-gated, potassium-selective glutamate receptor for the optical inhibition of neuronal firing. *Nat. Neurosci.* **13**, 1027–1032 (2010).
26. Volgraf, M. *et al.* Allosteric control of an ionotropic glutamate receptor with an optical switch. *Nat. Chem. Biol.* **2**, 47–52 (2006).
27. Ohndorf, U. M. & MacKinnon, R. Construction of a cyclic nucleotide-gated KcsA K⁺ channel. *J. Mol. Biol.* **350**, 857–865 (2005).
28. Sexton, L. T. *et al.* Resistive-pulse studies of proteins and protein/antibody complexes using a conical nanotube sensor. *J. Am. Chem. Soc.* **129**, 13144–13152 (2007).
29. Ding, S., Gao, C. & Gu, L. Capturing Single Molecules of Immunoglobulin and Ricin with an Aptamer-Encoded Glass Nanopore. **81**, 6649–6655 (2009).
30. Higgins, C. F. ABC Transporters: From Microorganisms to Man. *Annu. Rev. Cell Biol.* **8**, 67–113 (1992).
31. Tam, R. & Saier, M. H. Structural, functional, and evolutionary relationships among extracellular solute-binding receptors of bacteria. *Microbiol. Rev.* **57**, 320–346 (1993).
32. Fulyani, F. *et al.* Functional diversity of tandem substrate-binding domains in ABC transporters from pathogenic bacteria. *Structure* **21**, 1879–1888 (2013).
33. Fischer, M., Zhang, Q. Y., Hubbard, R. E. & Thomas, G. H. Caught in a TRAP: Substrate-binding proteins in secondary transport. *Trends in Microbiology* **18**, 471–478 (2010).
34. Winnen, B., Hvorup, R. N. & Saier, M. H. The tripartite tricarboxylate transporter (TTT) family. *Res. Microbiol.* **154**, 457–465 (2003).
35. Neiditch, M. B. *et al.* Ligand-Induced Asymmetry in Histidine Sensor Kinase Complex Regulates Quorum Sensing. *Cell* **126**, 1095–1108 (2006).
36. Armstrong, N., Sun, Y., Chen, G. Q. & Gouaux, E. Structural of a glutamate-receptor ligand-binding core in complex with kainate. *Nature* **395**, 913–917 (1998).
37. O’Hara, P. J. *et al.* The ligand-binding domain in metabotropic glutamate receptors is related to bacterial periplasmic binding proteins. *Neuron* **11**, 41–52 (1993).
38. Lewis, M. *et al.* Crystal structure of the lactose operon repressor and its complexes with DNA and inducer. *Science (80-)*. **271**, 1247–1254 (1996).
39. Scheepers, G. H., Lycklama a Nijeholt, J. A. & Poolman, B. An updated structural classification of substrate-binding proteins. *FEBS Lett.* **590**, 4393–4401 (2016).
40. Fukami-Kobayashi, K., Tateno, Y. & Nishikawa, K. Domain dislocation: a change of core structure in periplasmic binding proteins in their evolutionary history. *J. Mol. Biol.* **286**, 279–290 (1999).
41. Tang, C., Schwieters, C. D. & Clore, G. M. Open-to-closed transition in apo maltose-binding protein observed by paramagnetic NMR. **449**, 1078–1082 (2007).
42. Boer, M. De *et al.* Conformational and dynamic plasticity in substrate-binding proteins underlies selective transport in ABC importers. *Elife* **8**, 1–28 (2019).
43. Quioco, F. a. & Ledvina, P. S. Atomic structure and specificity of bacterial periplasmic receptors for active transport and chemotaxis: Variation of common themes. *Mol. Microbiol.* **20**, 17–25 (1996).
44. Karpowich, N. K., Huang, H. H., Smith, P. C. & Hunt, J. F. Crystal structures of the

- BtuF periplasmic-binding protein for vitamin B12 suggest a functionally important reduction in protein mobility upon ligand binding. *J. Biol. Chem.* **278**, 8429–8434 (2003).
45. Alicea, I. *et al.* Structure of the Escherichia coli phosphonate binding protein PhnD and rationally optimized phosphonate biosensors. *J. Mol. Biol.* **414**, 356–369 (2011).
 46. Ramos-Vicente, D. *et al.* Metazoan evolution of glutamate receptors reveals unreported phylogenetic groups and divergent lineage-specific events. *Elife* **7**, 1–36 (2018).
 47. Plested, A. J. R. Structural mechanisms of activation and desensitization in neurotransmitter-gated ion channels. *Nat. Struct. Mol. Biol.* **23**, 494–502 (2016).
 48. Lam, H. M. *et al.* Glutamate-receptor genes in plants. *Nature* **396**, 125–126 (1998).
 49. Chen, G. Q., Cui, C., Mayer, M. L. & Gouaux, E. Functional characterization of a potassium-selective prokaryotic glutamate receptor. *Nature* **402**, 817–821 (1999).
 50. Bocquet, N. *et al.* A prokaryotic proton-gated ion channel from the nicotinic acetylcholine receptor family. *Nature* **445**, 116–119 (2007).
 51. Traynelis, S. F. *et al.* Glutamate Receptor Ion Channels: Structure, Regulation, and Function. *Pharmacol. Rev.* **62**, 405–496 (2010).
 52. Lynch, J. Molecular structure and function of the glycine receptor chloride channel. *Physiol. Rev.* **84**, 1051–1095 (2004).
 53. Laube B, Langosch D, Betz H, S. V. Hyperekplexia mutations of the glycine receptor unmask the inhibitory subsite for beta-amino-acids. *Neuroreport* **6**, 897–900 (1995).
 54. Overington, J. P., Al-lazikani, B. & Hopkins, A. L. How many drug targets are there? *Nat. Rev. Drug Discov.* **5**, 993–996 (2006).
 55. Sobolevsky, A. I., Rosconi, M. P. & Gouaux, E. X-ray structure, symmetry and mechanism of an AMPA-subtype glutamate receptor. *Nature* **462**, (2009).
 56. Lee, C.-H. *et al.* NMDA receptor structures reveal subunit arrangement and pore architecture. *Nature* **511**, 191–197 (2014).
 57. Meyerson, J. R. *et al.* Structural basis of kainate subtype glutamate receptor desensitization. *Nature* **537**, 1–16 (2016).
 58. Ayalon, G. & Stern-Bach, Y. Functional assembly of AMPA and kainate receptors is mediated by several discrete protein-protein interactions. *Neuron* **31**, 103–113 (2001).
 59. Rossmann, M. *et al.* Subunit-selective N-terminal domain associations organize the formation of AMPA receptor heteromers. *EMBO J.* **30**, 959–971 (2011).
 60. Zhu, S., Stroebel, D., Yao, C. A., Taly, A. & Paoletti, P. Allosteric signaling and dynamics of the clamshell-like NMDA receptor GluN1 N-terminal domain. *Nat. Struct. Mol. Biol.* **20**, 477–485 (2013).
 61. Hansen, K. B., Furukawa, H. & Traynelis, S. F. Control of assembly and function of glutamate receptors by the amino-terminal domain. *Mol. Pharmacol.* **78**, 535–49 (2010).
 62. Stern-Bach, Y. *et al.* Agonist selectivity of glutamate receptors is specified by two domains structurally related to bacterial amino acid-binding proteins. *Neuron* **13**, 1345–1357 (1994).
 63. Sobolevsky, A. I. Structure and Gating of Tetrameric Glutamate Receptors. *J. Physiol.* **593**, 29–38 (2013).
 64. Tikhonov, D. B. & Magazanik, L. G. Origin and molecular evolution of ionotropic glutamate receptors. *Neurosci. Behav. Physiol.* **39**, 763–773 (2009).
 65. Wood, M. W., Vandongen, H. M. A. & Vandongen, A. M. J. Structural conservation of ion conduction pathways in K channels and glutamate receptors. *Proc. Natl. Acad. Sci. USA* **92**, 4882–4886 (1995).

66. Schönrock, M., Thiel, G. & Laube, B. Coupling of a viral K⁺-channel with a glutamate-binding-domain highlights the modular design of ionotropic glutamate-receptors. *Commun. Biol.* **2**, (2019).
67. Twomey, E. C. & Sobolevsky, A. I. Structural Mechanisms of Gating in Ionotropic Glutamate Receptors. *Biochemistry* **57**, 267–276 (2018).
68. Dürr, K. *et al.* Structure and Dynamics of AMPA Receptor GluA2 in Resting, Pre-Open, and Desensitized States. *Cell* **158**, 778–792 (2014).
69. Yelshanskaya, M. V., Li, M. & Sobolevsky, A. I. Structure of an agonist-bound ionotropic glutamate receptor. *Science (80-.)*. **345**, 1070–1074 (2014).
70. Armstrong, N., Jasti, J., Beich-Frandsen, M. & Gouaux, E. Measurement of Conformational Changes accompanying Desensitization in an Ionotropic Glutamate Receptor. *Cell* **127**, 85–97 (2006).
71. Karakas, E., Simorowski, N. & Furukawa, H. Structure of the zinc-bound amino-terminal domain of the NMDA receptor NR2B subunit. *EMBO J.* **28**, 3910–3920 (2009).
72. Karakas, E., Simorowski, N. & Furukawa, H. Subunit arrangement and phenylethanolamine binding in GluN1/GluN2B NMDA receptors. *Nature* **475**, 249–253 (2011).
73. Yuan, H., Hansen, K. B., Vance, K. M., Ogden, K. K. & Traynelis, S. F. Control of NMDA receptor function by the NR2 subunit amino-terminal domain. *J. Neurosci.* **29**, 12045–12058 (2009).
74. Gielen, M. *et al.* Structural Rearrangements of NR1/NR2A NMDA Receptors during Allosteric Inhibition. *Neuron* **57**, 80–93 (2008).
75. Hansen, K. B. *et al.* Structure, function, and allosteric modulation of NMDA receptors. *J. Gen. Physiol* **150**, 1081–1105 (2018).
76. Twomey, E. C., Yelshanskaya, M. V., Grassucci, R. A., Frank, J. & Sobolevsky, A. I. Channel opening and gating mechanism in AMPA-subtype glutamate receptors. *Nature* **549**, 60–65 (2017).
77. Karakas, E. & Furukawa, H. Crystal structure of a heterotetrameric NMDA receptor ion channel. *Science (80-.)*. **344**, 992–997 (2014).
78. Regan, M. C. *et al.* Structural Mechanism of Functional Modulation by Gene Splicing in NMDA Receptors. *Neuron* **98**, 521-529.e3 (2018).
79. Khatri, A. *et al.* Structural determinants and mechanism of action of a GluN2C-selective NMDA receptor positive allosteric modulator. *Mol. Pharmacol.* **86**, 548–560 (2014).
80. Legendre, P. The glycinergic inhibitory synapse P. *Cell. Mol. Life Sci.* **58**, 760–793 (2001).
81. Lehmann, T., Gloveli, T., Grantyn, R. & Meier, J. C. Glycinergic tonic inhibition of hippocampal neurons with depolarizing GABAergic transmission elicits histopathological signs of temporal lobe epilepsy. *J. Cell. Mol. Med.* **12**, 2848–2866 (2008).
82. Langosch, D., Thomas, L. E. O. & Betz, H. Conserved quaternary structure of ligand-gated ion channels : The postsynaptic glycine receptor is a pentamer. *Proc .Natl. Acad. Sci. USA* **85**, 7394–7398 (1988).
83. Du, J., Lu, W., Wu, S., Cheng, Y. & Gouaux, E. Glycine receptor mechanism elucidated by electron cryo-microscopy. *Nature* **526**, 224–229 (2015).
84. Burgos, C. F., Yévenes, G. E. & Aguayo, L. G. Structure and Pharmacologic Modulation of Inhibitory Glycine Receptors. 318–325 (2016).

-
85. Huang, X., Chen, H., Michelsen, K., Schneider, S. & Shaffer, P. L. Crystal structure of human glycine receptor- $\alpha 3$ bound to antagonist strychnine. *Nature* **526**, 277–280 (2015).
 86. Lape, R., Colquhoun, D. & Sivilotti, L. G. On the nature of partial agonism in the nicotinic receptor superfamily. *Nature* **454**, 722–727 (2008).
 87. Purohit, P., Mitra, A. & Auerbach, A. A stepwise mechanism for acetylcholine receptor channel gating. *Nature* **446**, 930–933 (2007).
 88. Colquhoun, D. & Lape, R. Allosteric coupling in ligand-gated ion channels. *J. Gen. Physiol.* **140**, 599–612 (2012).
 89. Kumar, A. *et al.* Mechanisms of activation and desensitization of full-length glycine receptor in lipid nanodiscs. *Nat. Commun.* **11**, 1–14 (2020).
 90. Yu, J. *et al.* Mechanism of gating and partial agonist action in the glycine receptor. preprint at <https://biorxiv.org/content/10.1101> (2019).

2. Studies

Chapter I: Thermophoretic analysis of ligand-specific conformational states of the inhibitory glycine receptor embedded in copolymer nanodiscs

This chapter has been published in:

Bernhard M, Laube B. *Thermophoretic analysis of ligand-specific conformational states of the inhibitory glycine receptor embedded in copolymer nanodiscs*. Sci Rep. 2020;10(1):16569.

doi:10.1038/s41598-020-73157-2

Contributions:

M.B. hat das Manuskript geschrieben. M.B. hat alle Abbildungen erstellt. M.B. hat alle Experimente und Analysen durchgeführt.

M.B. und B.L. waren an der Konzipierung der Experimente beteiligt.

B.L. betreute das Projekt und überarbeitete das Manuskript.



OPEN Thermophoretic analysis of ligand-specific conformational states of the inhibitory glycine receptor embedded in copolymer nanodiscs

Max Bernhard¹ & Bodo Laube^{1,2}✉

The glycine receptor (GlyR), a member of the pentameric ligand-gated ion channel family (pLGIC), displays remarkable variations in the affinity and efficacy of the full agonist glycine and the partial agonist taurine depending on the cell system used. Despite detailed insights in the GlyR three-dimensional structure and activation mechanism, little is known about conformational rearrangements induced by these agonists. Here, we characterized the conformational states of the $\alpha 1$ GlyR upon binding of glycine and taurine by microscale thermophoresis expressed in HEK293 cells and *Xenopus* oocytes after solubilization in amphipathic styrene-maleic acid copolymer nanodiscs. Our results show that glycine and taurine induce different conformational transitions of the GlyR upon ligand binding. In contrast, the variability of agonist affinity is not mediated by an altered conformational change. Thus, our data shed light on specific agonist induced conformational features and mechanisms of pLGIC upon ligand binding determining receptor activation in native environments.

The superfamily of pentameric ligand-gated ion channels (pLGIC) mediates excitatory and inhibitory synaptic neurotransmission in the central nervous system¹ and is the target for many therapeutic agents². The knowledge of the underlying mechanisms determining apparent affinity and efficacy of small ligands acting on these receptors is fundamental for the understanding of their physiological and pharmacological properties under developmental, normal and pathological conditions of the brain. One of the most pressing questions regarding ligand-specific activity concerns the underlying mechanisms by which partial and full agonists possess variable half-maximal effective concentration (EC_{50}) values and amplitude responses under different cellular conditions. Despite detailed insights into their three-dimensional structures and general activation mechanisms, an accurate knowledge of the underlying structural confinements determining the affinity and efficacy of agonists at pLGICs is still lacking^{1,3}. The inhibitory glycine receptor (GlyR), a member of the pLGICs, is an outstanding example displaying exceptional variations in the affinity and efficacy of its agonists⁴. GlyRs mediate, together with GABA receptors, the majority of fast inhibitory neurotransmission in the central nervous system and are implicated in neuronal diseases like hyperekplexia^{4,5} and forms of epilepsy⁶. GlyRs assemble as homopentamers of α -subunits ($\alpha 1-4$) or heteropentamers, containing both α - and β -subunits⁷ and are composed of an extracellular orthosteric ligand binding site (ECD), a transmembrane spanning ion-channel (TMD) and an intracellular domain (ICD). GlyR activation upon agonist binding induces a contraction within the ECD that is transmitted to the TMD leading to the opening of the chloride selective intrinsic channel pore⁸. Remarkably, the efficacy to open the ion channel depends on the agonist used, i.e. glycine acts as a full agonist inducing maximal current responses with opening times of 95–98% seen in single-channel recordings⁹, whereas taurine acts as a partial agonist producing a decreased maximal response relative to the effect produced by glycine that is reflected by lower open-channel probabilities¹⁰. However, both the efficacy and affinity of glycine and taurine also strongly depend

¹Department of Biology, Neurophysiology and Neurosensory Systems, Technical University of Darmstadt, Schnittpahnstrasse 3, 64287 Darmstadt, Germany. ²Centre for Synthetic Biology, Technical University of Darmstadt, 64283 Darmstadt, Germany. ✉email: laube@bio.tu-darmstadt.de

on the expression system used^{4,11} and can vary up to an order of magnitude when heterologously expressed in HEK293 cells^{12,13} and *X. laevis* oocytes^{14,15}. Further, the relative efficacy of taurine of heterologous expressed $\alpha 1$ GlyR is directly correlated with its apparent affinity¹⁵ indicating a dependency of taurine-affinity and -efficacy in heterologous expression systems. Interestingly, these results cannot be dismissed as expression system dependent phenomena because the taurine efficacy and affinity similarly varies in magnitude in different brain regions^{16–18}, indicating that mechanisms regulating the efficacy of the partial agonist taurine in the brain are related to differences also seen in heterologous expression systems. However, despite several available crystal structures of glycine receptors^{8,19} and extended kinetic models based on single-channel recordings^{10,20}, so far little is known about the specific conformational rearrangements of the GlyR during receptor activation induced by full and partial agonists and even less which conformations can be adopted during activation in different cell systems. Thus, structural aspects of the relative affinity and efficacy of ligands to open the intrinsic ion channel within specific native environments, a core question in receptor pharmacology, may be ideally investigated at the GlyR by analyzing ligand-specific conformational states under native conditions.

Here we report the combination of detergent-free isolation of the heterologous expressed $\alpha 1$ GlyR in HEK293 cells and *X. laevis* oocytes by amphipathic styrene-maleic acid (SMA)-copolymers with microscale thermophoresis (MST) as a new approach to study structural impacts of full and partial agonists for the GlyR conformation. Upon successful solubilization of $\alpha 1$ GlyR from HEK293 cells and *X. laevis* oocytes in nanodiscs we can show by MST that both the affinity and efficacy of the full agonist glycine to induce a conformational change was identical in both expression systems although the respective electrophysiological EC₅₀ values differed by an order of magnitude. In contrast, the partial agonist taurine stabilized a distinct conformational state that can be clearly distinguished from the conformational state adopted after glycine binding. Thus, we provide experimental evidence for the underlying mechanism of partial agonism at the GlyR and that variations in EC₅₀ values observed in different expression systems are likely mediated by an impaired ability of the receptor to open the channel once the agonist has bound.

Materials and methods

GlyR constructs. For heterologous expression in HEK293 cells and *X. laevis* oocytes, human his tagged $\alpha 1$ -His GlyR²¹ and N-terminal GFP fused $\alpha 1$ -GFP GlyR was cloned into pCDNA3.1(+) vector by using NotI and NheI (Thermo Fisher Scientific, Waltham, MA, USA). All constructs were confirmed by sequencing (Seqlab, Göttingen, Germany).

Heterologous expression of $\alpha 1$ GlyR in HEK293 cells. HEK293 cells were cultured in minimum essential medium (MEM) supplemented with 10% (v/v) FCS, 2 mM L-glutamine and streptomycin (100 μ g/ml) at 37 °C and 5% CO₂. For transfection, 14–20 $\times 10^6$ cells were diluted in electroporation buffer 1 M (5 mM KCl, 15 mM MgCl₂, 120 mM Na₂HPO₄/NaH₂PO₄ pH 7.2, 50 mM mannitol) at a final concentration of 1 $\times 10^6$ cells per 100 μ l and 500 ng per 100 μ l of the respective plasmid was added. Electroporation was performed using the Amaxa Nucleofector II S system (Lonza, Basel, Switzerland). After transfection, cells were reseeded in 75 cm² flasks with MEM and incubated for 48 h.

Ethical approval. All methods involving animals were carried out in accordance with the guidelines and regulations of the local animal care and use committee. Methods were approved by the Technical University of Darmstadt (II25.3-19c20/15, RP Darmstadt, Germany).

Heterologous expression of $\alpha 1$ -GFP GlyR in *X. laevis* oocytes. cRNA was synthesized using the AmpliCap-Max T7 High Yield Message Maker Kit (CellsScript, Madison, WI, USA). Therefore GFP-GlyR $\alpha 1$ in pCDNA3.1(+) was linearized with NotI. Oocytes were surgically taken from female *X. laevis* after anesthesia with 0.1% Tricaine in water. For SMA-copolymer solubilization, 300–400 oocytes were injected with 50 ng in a volume of 50.6 nl of cRNA. After injection the oocytes were incubated in ND-96 solution (96 mM NaCl, 2 mM KCl, 1 mM CaCl₂, 1 mM MgCl₂, 5 mM HEPES, pH 7.4) at 18 °C for 1–2 days.

SMA-copolymer solubilization of $\alpha 1$ GlyR. For SMA copolymer solubilization of the heterogeneous expressed $\alpha 1$ GlyR in HEK293 cells, cells were washed with PBS, subsequently scraped off and resuspended in 2 ml PBS. Cells were washed and resuspended in 150 mM NaCl, 50 mM Tris/HCl pH 8.0 and lysed by sonification. Membranes are separated by ultracentrifugation at 100,000g for 1.5 h and 4 °C. For $\alpha 1$ GlyR expressed in oocytes, cells were resuspended in 20 mM Tris-HCl, pH 8.0 and mechanically homogenized by pipetting. To remove cell debris, cells were centrifuged at 1000 \times g for 15 min at 4 °C. Membranes were separated by ultracentrifugation at 100,000 \times g for 1 h at 4 °C. To remove additional yolk proteins²², pellet was washed with 1 M NaCl, 20 mM Tris-HCl, pH 8.0, followed by an additional ultracentrifugation step as written above. The membrane pellet was resuspended in SMA-solubilization buffer (150 mM NaCl, 10% glycerol, 50 mM Tris/HCl pH 8.0, SIGMAFAST Protease Inhibitor Cocktail (Sigma-Aldrich, St. Louis, MO, USA) to a concentration of 80 mg/ml. A freshly prepared 4% (w/v) SMA copolymer solution (Lipodisq Styrene:Maleic Anhydride Copolymer 3:1, Pre-hydrolyzed, Sigma-Aldrich) in SMA-solubilization buffer was slowly dropped under stirring to the membrane suspension in a 1:1 ratio and was solubilized for 1 h at room temperature. To remove all non-solubilized cell fragments, the suspension was centrifuged at 100,000g for 45 min and 4 °C.

Ni-NTA purification and size exclusion chromatography. The $\alpha 1$ -His GlyR SMA copolymer nanodiscs containing supernatant was incubated with pre-equilibrated 0.2 ml HisPur Ni-NTA spin columns (Thermo

Fisher Scientific) overnight at 4 °C under gentle rotation. Spin columns were washed three times with SMA-solubilization buffer supplemented with 25 mM imidazole and α 1-His GlyR SMALPs were eluted in SMA-solubilization buffer supplemented with 400 mM imidazole. For separation of the previously purified α 1 GlyR nanodiscs from other soluble proteins and for further analysis, pooled elution fractions were loaded on a Superdex 200 increase 10/300 GL (GE Healthcare, Chicago, IL, USA) connected to an Äkta pure (GE Healthcare) and buffer was exchanged to 50 mM Tris/HCl pH 7.4 and 150 mM NaCl. Estimation of the molecular weight (MW) was based on a calibration curve by a linear fit of proteins of known MW (Aldolase, Ovalbumin, Conalbumin, Cyanocobalamin, Thyroglobulin) versus the partition coefficient k_{av} ($k_{av} = V_{el} - V_0/V_t - V_0$, where V_{el} is the elution volume of the protein, V_t is the total column volume and V_0 is the void volume). The hydrodynamic radii (R_s , Stokes radius) were calculated, according to the Stokes–Einstein relation²³, by a linear fit of the Stokes radii of known proteins versus the square root of the negative decadic logarithm of the k_{av} .

SDS-PAGE and western blot. SDS-PAGE and western blot analysis was performed as described elsewhere²⁴. In brief, proteins were separated using a 10% sodium dodecyl sulfate polyacrylamide gel electrophoresis (SDS-PAGE). For SDS-PAGE analysis, the gel was stained with Pierce Silver Stain Kit (Thermo Fisher Scientific). For western blot analysis, separated proteins were transferred to a PVDF membrane (Bio-Rad, Feldkirchen, Germany) and the membrane was blocked for 1 h in TBS-T supplemented with 5% skim milk. Afterwards, the membrane was incubated with 1:500 primary eGFP Polyclonal antibody (CAB4211, Thermo Fisher Scientific) in TBS-T containing 1% skim milk over night at 4 °C. The membrane was washed 3 times for 10 min with TBS-T and incubated with the goat anti-rabbit IgG-HRP (sc-2054, Santa Cruz Biotechnology, Dallas, TX, USA) in TBS-T containing 1% skim milk for 1 h at room temperature. The membrane was washed 3 times for 10 min in TBS-T and protein bands were visualized by adding Pierce Western Blotting Substrate (Thermo Fisher Scientific) and detected with a CCD camera.

Microscale thermophoresis. Microscale thermophoresis (MST) analysis was performed using a NanoTemper Monolith NT.115 instrument (NanoTemper Technologies, Munich, Germany). Therefore, purified α 1-His GlyR nanodiscs or total solubilized cell membranes with α 1-GFP GlyR were diluted to a concentration of 400 nM in PBS. α 1-His GlyR was fluorescence-labeled using the Monolith NT His-Tag Labeling Kit RED-tris-NTA (NanoTemper Technologies). Labeled GlyR α 1 SMALPs were added in a 1:1 ratio to a 1:2 dilution series with a final concentration of 3 mM down to 0.73 μ M for glycine or 12.5 mM down to 6 μ M for taurine, as well as 0 μ M for each ligand as an internal control and loaded into standard capillaries (Monolith NT.115 Capillaries, NanoTemper Technologies). Thermophoresis was measured at 21 °C for 15 or 20 s with 40% LED power and 60% infrared laser power. For MST experiments $n = 3-4$ independent technical measurements were collected from $N = 2-3$ independent oocyte or HEK293 cell batches.

Electrophysiological recordings. 1–2 days after injection of α 1 GlyR cRNA in *X. laevis* oocytes, whole-cell currents were recorded by two-electrode voltage-clamp using an Axoclamp 900A amplifier and a Digidata 1550A digitizer. Data were sampled at 5 kHz after low-pass filtering at 200 Hz and recorded with Clampex 10.7 (Molecular Devices, San Jose, USA). For recordings, oocytes were clamped at -70 mV in external Ringer solution (115 mM NaCl, 1 mM KCl, 0.9 mM CaCl₂, 10 mM HEPES, pH 7.4). For HEK293, whole-cell recordings of GlyR α 1 transfected cells were carried out as described in Laube et al. 2000²⁵. In brief, whole cell currents were recorded 2 days after transfection using an EPC-9 amplifier (HEKA, Ludwigshafen, Germany) and data were sampled at 20 Hz. Patch pipettes contained 120 mM CsCl, 20 mM TEA-Cl, 1 mM CaCl₂, 2 mM MgCl₂, 11 mM EGTA, 10 mM HEPES, pH 7.2. Membrane potential was clamped at -70 mV and cells were perfused with external solution (137 mM NaCl, 5.4 KCl, 1.8 mM CaCl₂, 1 mM MgCl, 5 mM HEPES, pH 7.4). Increasing glycine concentrations were applied using a microcapillary application system (DAD-12, Adams and List, Westbury, NY, USA).

Data and statistical analysis. For electrophysiological dose–response analysis, normalized current responses were plotted against the agonist concentration and fitted with a sigmoidal Hill equation $I/I_{max} = 100 \times c^n / (c^n + aEC_{50}^n)$ in GraphPad Prism 8 (GraphPad Software Inc., La Jolla, USA), where I/I_{max} is the normalized current, c the concentration, n the Hill coefficient and aEC_{50} the agonist concentration resulting in a half-maximal response. For thermophoretic binding experiments, the relative thermophoretic fluorescence signal F_{norm} was calculated as ratio of the initial fluorescence ($F_{cold} = 1$ s) and fluorescence after thermodiffusion ($F_{hot} = 15$ s) using the following equation in MO.Affinity Analysis software (NanoTemper Technologies): $F_{norm} = F_{hot}/F_{cold} = 1 + (\partial F/\partial T - S_T)\Delta T$, where $\partial F/\partial T$ is the fluorescence change due to the fluorophore's temperature dependence and S_T the Soret coefficient. For thermophoretic dose–response analysis, the normalized relative fluorescences were plotted against the agonist concentration and fitted with the sigmoidal Hill equation $F_{norm}/F_{norm,max} = 100/(1 + (cEC_{50}/c)^n)$, where $F_{norm}/F_{norm,max}$ is the normalized relative fluorescence, cEC_{50} the agonist concentration resulting in a half-maximal response and n the Hill coefficient. All values are given in mean \pm SEM, unless indicated otherwise. Statistical significance was determined using a Student's two-tailed, unpaired two-side t test with * $p < 0.05$, ** $p < 0.01$, and *** $p < 0.001$ levels. Equality of variances was confirmed using a F test.

Results

Detergent-free purification of homomeric α 1 GlyR in SMA-copolymer nanodiscs. To probe the general potential of SMA-solubilized GlyRs for pharmacological analysis we solubilized a His-tag fused α 1 construct (α 1-His) by incubating SMA copolymers with the isolated membrane fraction of α 1-His overexpressing

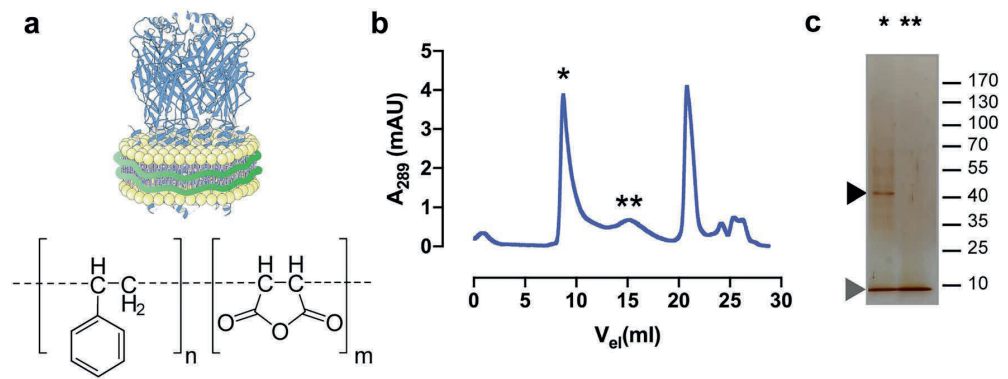


Figure 1. Purification and functional characterization of the $\alpha 1$ -His GlyR in SMA-copolymer nanodiscs. (a) Schematic representation of GlyR (PDB: 3JAE) in native nanodiscs (upper) and chemical structure of SMA-copolymer (lower) with a ratio of n:m of 2:1 used in this study. Size exclusion chromatogram (b) and SDS-PAGE analysis (c) showing an efficient separation of $\alpha 1$ -His GlyR nanodiscs. Peak fraction (*) shows a clear band (black arrow) between 40 and 55 kDa, corresponding to the $\alpha 1$ GlyR (MW: 48 kDa) and a band migrating at ~ 10 kDa corresponding to SMA copolymer. Gel image was cropped, indicated by a grey cropping line. Subfigure (a) was created using Adobe Illustrator CC version 24.3 (<https://www.adobe.com/kr/products/illustrator.html>).

HEK293 cells (Fig. 1a). The $\alpha 1$ -His containing nanodiscs (Fig. 1a) were further isolated with Ni-affinity chromatography, followed by size-exclusion chromatography (SEC). SDS-PAGE analysis of peak fraction one (Fig. 1b) shows a clear band, migrating at ~ 48 kDa, corresponding to the molecular weight of the $\alpha 1$ GlyR monomer (Fig. 1, Supplementary Fig. S1). The SMA copolymer runs at an expected lower molecular weight²⁶ of approximately 10 kDa. The second SEC peak (Fig. 1b) reveals only SMA copolymer without any additional protein band, which represent probably free polymer that was interacting with the Ni-affinity columns. The molecular weight and size of the purified $\alpha 1$ GlyR nanodiscs were further investigated by the generated SEC data. Thus, the nanodiscs having an average molecular weight of 495 kDa with a calculated stoke radius of 13.2 nm, which is in good agreement with previous studies^{26–28}. Since the pentameric receptor has a molecular weight of 240 kDa and no accessory proteins in the purified fraction can be detected, we conclude that the residual molecular weight of the nanodiscs must result from its lipid bilayer. We therefore showed that the SMA copolymer solubilization of $\alpha 1$ GlyR in nanodiscs was successful and suitable for further investigation.

Functional characterization of $\alpha 1$ GlyR nanodiscs by microscale thermophoresis. To examine the functionality of the purified $\alpha 1$ GlyR nanodiscs, we intended to analyze concentration-dependent conformational changes upon binding of the agonist glycine by microscale thermophoresis (MST). Therefore, we diluted the fluorescence labeled $\alpha 1$ -His GlyR containing nanodiscs (see “Materials and Methods” section) to a final concentration of 400 nM and added a glycine dilution series of 3 mM down to 0.73 μ M. Samples were loaded into glass capillaries and get focused by an infrared (IR) laser, creating a spatial temperature gradient. Thermophoretic movement of the fluorescence labeled $\alpha 1$ -His GlyR nanodiscs was measured by fluorescence emission coupled into the IR laser path²⁹. We found that addition of glycine to the receptor complex was sufficient to induce a change in thermophoretic mobility of the complex (Fig. 2a). Increasing glycine concentrations resulted in a concentration-dependent shift of the thermophoretic signal saturating at 500 μ M glycine (Fig. 2b). Because no concentration-dependent fluorophore quenching could be observed (Fig. 2c), we concluded that the purified SMA copolymer nanodiscs must contain functional pentameric $\alpha 1$ GlyR receptors and that the alterations in particle movement obtained must be due to a glycine-induced alteration of the conformation, size, charge and/or hydration shell³⁰ of the GlyR. This is consistent with the findings at native GlyRs where (i) pentameric assembly of the GlyR is required for the proper formation of the specific glycine-binding site at the interface of adjacent subunits and (ii) binding of glycine induces a significant conformational rearrangement of the ECD. Analyzing the glycine depended shift of the thermophoretic movements revealed an EC_{50} value of 65 ± 22.8 μ M (mean \pm SEM; $n = 4$; Fig. 2d), which is similar to the apparent EC_{50} value obtained by electrophysiology in $\alpha 1$ GlyR expressing HEK293 cells^{12,13}. To distinguish electrophysiological and MST-determined EC_{50} values, we termed them in the following as aEC_{50} (a for apparent; e-phys) and cEC_{50} (c for conformation, MST), respectively. In conclusion, our results obtained upon analyzing glycine concentration-dependent conformational changes of the GlyR by MST embedded in SMA copolymer nanodiscs, indicate that the glycine-induced contraction within the ECD leading to a highly efficient gating of the channel pore, resulting in a 1:1 ratio of cEC_{50} and aEC_{50} values.

Characterization of glycine binding to $\alpha 1$ GlyR obtained from HEK293 cells and *X. laevis* oocytes. One key advantage of solubilizing membrane proteins in SMA copolymer nanodiscs is the retention of their native lipid surrounding, enabling the analysis of ligand-induced conformational changes while preserving the influence of the native membrane environment in in vivo-like conditions. Homomeric $\alpha 1$ GlyR exhibit a major discrepancy concerning their glycine affinity with aEC_{50} values of 212.9 ± 21 μ M and 68.8 ± 7.4 μ M when

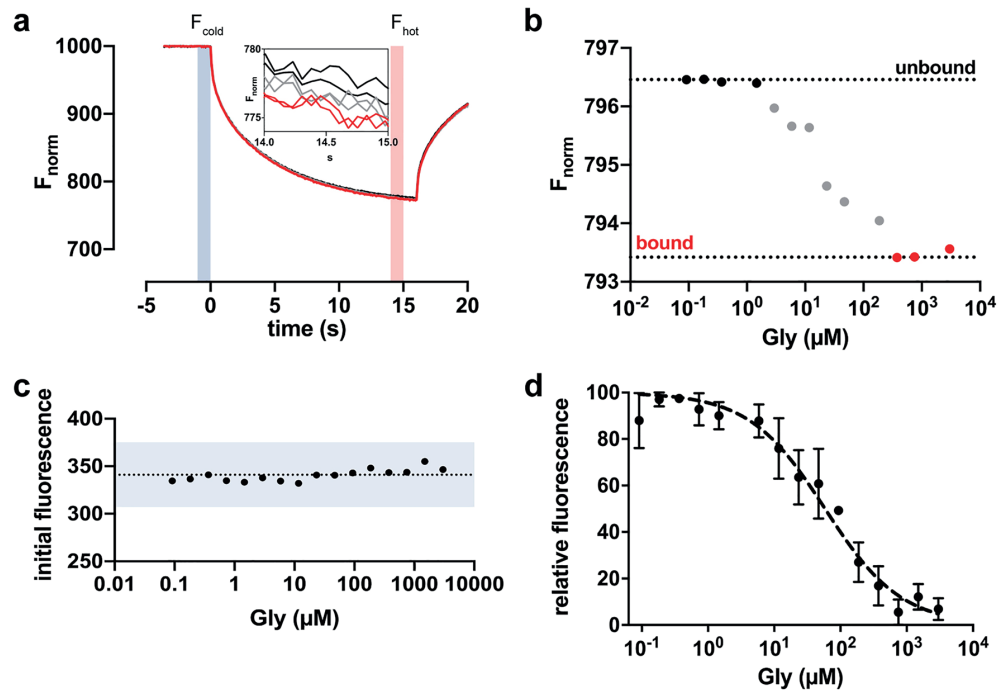


Figure 2. Functional characterization of SMA copolymer solubilized $\alpha 1$ -His GlyR. (a) Example trace of primary thermophoresis data. Thermophoretic movement of $\alpha 1$ -His GlyR nanodiscs is expressed as the change in fluorescence signal between initial fluorescence F_{cold} (0 s) and fluorescence after thermodiffusion F_{hot} (15 s) and was calculated as ratio of both values as described in the “Materials and Methods” section. Inset shows an amplification of representative fluorescence traces of the thermophoretic movement of the fluorescence labeled $\alpha 1$ -His GlyR between 14 and 15 s (F_{hot}) obtained at different glycine concentrations [0 and 1 (black), 10 and 100 (gray) and 1000 and 3000 μM glycine (red)]. (b) The change in thermophoretic movement upon binding of increasing concentrations of Gly results in a change of the relative fluorescence between the unbound state (black) and glycine-bound state (red) after 15 s. (c) Initial fluorescence count distribution for each concentration is under 10% and showing no ligand-dependent fluorescence quenching. (d) Dose–response curve obtained from MST experiments of $\alpha 1$ -His GlyR. Binding of glycine to fluorescence-labeled $\alpha 1$ -GlyR was obtained with a titration series from 3 mM to 0.73 μM in PBS buffer, pH 7.4. The change in thermophoretic signal leads to a cEC_{50} of $65 \pm 22.8 \mu\text{M}$. Error bars represent SEM between $n = 3$ independent experiments.

heterologously expressed in *X. laevis* oocytes or HEK293 cells, respectively (Fig. 3a). The root cause and underlying mechanism of these variations in the efficiency of receptor activation across different expression systems is still unknown. To further explore this concept we analyzed the binding affinity for $\alpha 1$ GlyR extracted from HEK293 cells and oocytes. To maximally mimic the complex environmental conditions found in the cells and to simplify the analytical process, we used an N-terminal GFP fused receptor ($\alpha 1$ -GFP GlyR) construct, that was directly measured after SMA-solubilization within the total nanodiscs fraction, that has previously reported for soluble GFP fused proteins²⁹. Western blot analysis (Fig. 3b, Supplementary Fig. S2) of the solubilized membrane fractions indicates an adequate incorporation of GlyRs into SMA copolymer nanodiscs. For comparable results, we first probed the binding affinity for glycine from HEK293 cell lysate. $\alpha 1$ -GFP GlyRs also showed a concentration-dependent shift in their thermophoretic mobility, similar to purified and fluorescence labeled His-tagged $\alpha 1$ GlyR, with a cEC_{50} value of $40.9 \pm 13.4 \mu\text{M}$ ($p = 0.22$, $n = 4$). A concentration-dependent GFP quenching was not detected as well (not shown). Thus our GFP tagged $\alpha 1$ GlyR yield similar cEC_{50} values compared to pure $\alpha 1$ GlyR nanodiscs and was suitable for the comparative analysis of $\alpha 1$ GlyRs expressed in oocytes. Next we analyzed the apparent glycine binding affinities of $\alpha 1$ GlyR extracted from oocyte membranes (Fig. 3a,c). The determined cEC_{50} of $52.6 \pm 40.8 \mu\text{M}$ ($n = 4$) for glycine reveals no significant difference ($p = 0.58$; Fig. 3c) compared with the cEC_{50} value obtained from HEK293 cells. Thus, the cEC_{50} value obtained from HEK293 cells is identical with the aEC_{50} ($p = 0.23$), whereas the cEC_{50} value obtained from oocytes is about 4 times lower than the aEC_{50} ($p < 0.01$). Furthermore, the similar thermophoretic signal amplitudes ($p = 0.41$; Fig. 3d) obtained from both expression systems indicate that the GlyR adopts the same ECD configuration with a similar degree of domain-closure upon glycine binding. These findings implicate, that the efficiency of glycine to induce the conformational change within the ECD is identical in both expression systems and the increased aEC_{50} observed in oocytes must be linked to an impaired channel opening.

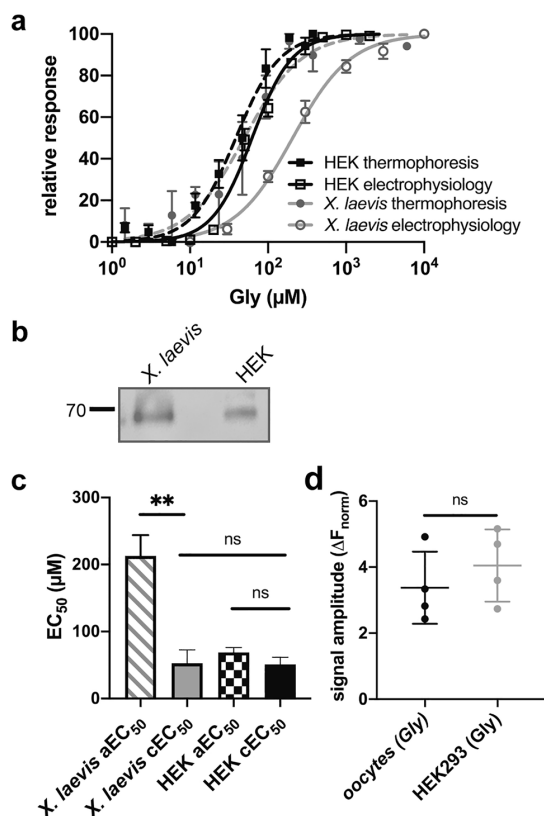


Figure 3. Functional analysis of $\alpha 1$ -GFP GlyR nanodiscs from HEK293 cells and *X. laevis* oocytes. **(a)** Dose-response relationship of $\alpha 1$ -GFP GlyR obtained by MST experiments and electrophysiological recordings from HEK293 cells and oocytes. MST data points were inversely normalized for better comparison with dose-response curves obtained from electrophysiological measurements. Data are shown in mean \pm SEM. **(b)** Western blot of SMA-copolymer solubilized GFP-GlyR $\alpha 1$ obtained from the membrane fractions of oocytes and HEK293 cells, show a single band at the calculated molecular weight below 70 kDa. Western blot image was cropped, indicated by a grey cropping line. **(c)** Electrophysiological experiments obtained from oocytes and HEK293 cells revealed a EC_{50} values $212.9 \pm 21 \mu\text{M}$ and $68.8 \pm 7.4 \mu\text{M}$, respectively. c EC_{50} values of $52.6 \pm 40.8 \mu\text{M}$ ($n = 4$) and $40.9 \pm 13.4 \mu\text{M}$ ($n = 4$) obtained from oocytes and HEK293 cells showing no significant difference ($p = 0.41$). The a EC_{50} obtained from is significantly higher ($p < 0.01$) than the measured c EC_{50} , while the a EC_{50} and c EC_{50} obtained from HEK293 cells show no difference ($p = 0.23$). Error bars represent SEM between independent experiments. **(d)** Signal amplitudes obtained from MST experiments reveal no differences between HEK293 cells (signal amplitude = 4.04 ± 1.09) and oocytes (signal amplitude = 3.38 ± 1.09 ; $p = 0.41$, $n = 4$). Data are shown in mean \pm SD. Unpaired two-side t test for statistics.

Conformational changes induced by binding of the partial agonist taurine. Taurine acts as a partial agonist on $\alpha 1$ GlyR in oocytes with an a EC_{50} value of $843 \pm 16 \mu\text{M}$ ($n = 3$) and a maximal current of 61% compared to glycine (Fig. 4a). To investigate how taurine influences the ECD conformation and if glycine may act as a partial agonist in oocytes, we analyzed the conformational transformation of $\alpha 1$ -GFP GlyR containing SMA nanodiscs in response to taurine by MST, as well. As expected, the c EC_{50} value of $473.8 \pm 66.1 \mu\text{M}$ ($n = 3$; Fig. 4b) is much higher than for glycine and is approximately half as much as the obtained a EC_{50} value ($n = 3$; $p < 0.05$). Also the Hill coefficient of 0.8 decreased for taurine, which is in good agreement with previous studies, reporting a decrease for less efficient agonists^{15,31}. Since the binding of the partial agonist taurine might stabilize a conformational state with an altered ECD closure, we analyzed the discrepancies in thermophoretic movement between the unbound and agonist bound states. We found, that the signal amplitude between glycine and taurine significantly decreases ($p < 0.05$, Fig. 4c,d) from 3.38 ± 1.09 to 1.32 ± 0.17 , respectively. This finding implicates, that taurine stabilizes a distinct conformational state under saturating conditions that can be clearly distinguished from the conformational state adopted after glycine binding. In contrast, binding of glycine to the GlyR induces in both expression systems the same overall conformational configuration, leading to the conclusion that glycine acts not as a partial agonist in oocytes like taurine.

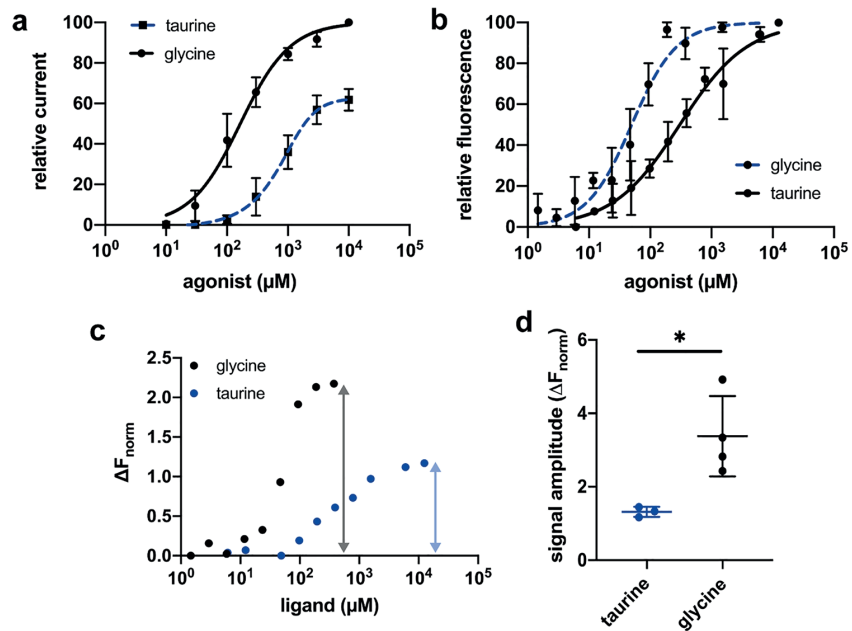


Figure 4. Binding characteristics of the partial agonist taurine to $\alpha 1$ -GFP GlyR nanodiscs. (a) Dose–response data for glycine and taurine of heterologous expressed $\alpha 1$ GlyR from *X. laevis* oocytes. Taurine acts as a partial agonist with an aEC_{50} value of $843 \pm 16 \mu M$ reaching a maximum current of 61% compared to glycine ($n = 3$). Taurine currents are normalized to the maximum glycine currents for each cell. Dose–response data of glycine are the same as shown in Fig. 3. Error bars represent SEM. (b) MST binding experiment of $\alpha 1$ -GFP GlyR with a taurine titration series of 6 μM to 12.5 mM results in a cEC_{50} value of $473.8 \pm 46.1 \mu M$ ($n = 3$). Error bars represent SEM. (c) Exemplary $\alpha 1$ -GFP GlyR MST data of taurine (blue circles) and glycine (black circles) obtained from oocytes displaying a difference in their maximal thermophoretic mobility (grey and blue arrows). (d) Comparison of the signal amplitudes of $\alpha 1$ -GFP GlyR SMALPs expressed in HEK293 cells and oocytes for glycine and taurine. Binding of taurine leads to a significant decreased thermophoretic movement ($p = 0.024$, unpaired two-side t test, $n = 3$) with signal amplitudes of 1.32 ± 0.14 compared to glycine-bound receptors with signal amplitudes of 3.38 ± 1.09 . Data are shown in mean \pm SD.

Discussion

In this study, we characterized the conformational states of the homomeric $\alpha 1$ GlyR in SMA copolymer nanodiscs by MST during receptor activation by glycine and the partial agonist taurine upon heterologous expression in HEK293 cells and *Xenopus* oocytes. Our results indicate that in the GlyR (i) partial and full agonists induce different conformational transitions and (ii) conformational transitions after agonist-binding affect apparent affinity. Thus our data shed light on the conformational features and mechanisms determining receptor activation by different agonists in different cell systems in the pLGIC superfamily.

In principle, two different models for the conformational states induced by a full and partial agonist at pLGICs can be envisaged. First, binding of the agonist simply shifts the equilibrium between the closed state and the open state of the channel. This model is based on the initial work by del Castillo and Katz³², where it has been supposed that full and partial agonists differ in their efficiency to activate a receptor, implying that both partial and full agonists stabilize the same open conformational state of the receptor. Consequently, a full agonist would promote efficient channel opening, while a partial agonist would be less effective in stabilizing the open state. Second, it can be assumed that a full and a partial agonist can adopt different conformational states in the agonist binding domain which are correlated to the extent of channel opening, mainly depending on the specific stereochemical properties of the ligand. Recent studies at the GlyR indicate that receptor activation includes one or more intermediate states, so called flipped or primed states, where the ECD is closed but the channel is still shut^{9,10,20}. In this model, the origin of partial agonism would be related to a reduced ability of the receptor to reach an intermediated pre-open state, rather than a reduced ability to fully activate the receptor, when the intermediated is reached^{10,33}. Nevertheless, little is known if the altered receptor kinetic for partial agonists is also reflected by distinct conformational states, as seen in ionotropic glutamate receptors^{34,35}.

Our thermophoretic analysis during receptor activation induced by agonists reveals large conformational changes of the GlyR. We attribute the detected agonist-induced rearrangements to a contraction within the ECD entrapping the ligand between adjacent subunits^{8,36,37}, rather than structural changes within the channel pore itself, which are masked by the surrounding lipid-bilayer of the nanodisc. This is consistent with a recent finding that, although full and partial agonists of the GlyR have the same orientation within the ECD upon binding,

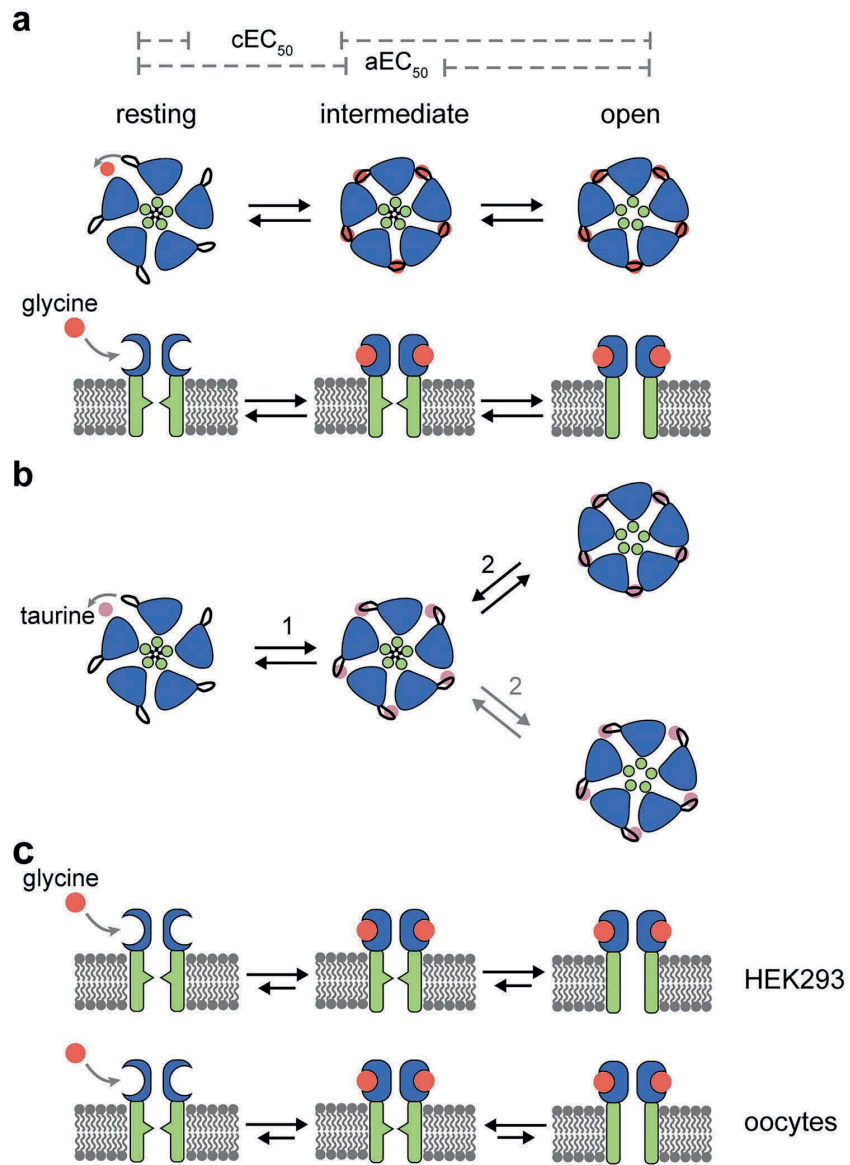


Figure 5. Schematic model of the activation mechanism of GlyRs for full and partial agonists. **(a)** The general activation mechanism of GlyRs includes at least three conformational states, whereby two conformations adopting a contracted ligand-bound ECD. Binding of a full agonist (red dot) induced an ECD closure of the resting receptor, while the ion channel is still shut (intermediate state). This ECD closure finally opens the ion channel and activates the receptor (open state). The ability of an agonist to change the conformation within the ECD (cEC_{50}) was measured by MST, while the general ability to activate the receptor (aEC_{50}) was determined by electrophysiological methods. **(b)** Binding of a partial agonist (purple) initiate an incomplete closure of the ECD (1). The receptor is either activated by a further ECD closure (2, grey) that leads to an ion channel opening (open state) or can directly open with a less contracted ECD (2, black). **(c)** GlyR activation in HEK293 cells and oocytes. Glycine binding to GlyRs in HEK293 cells is characterized by a contraction of the ECD and a rapid channel opening, reflected by similar cEC_{50} and aEC_{50} values. Binding of glycine to GlyRs in oocytes is also characterized by an efficient reorientation of the ECD with an impaired channel opening, possibly stabilizing an intermediate state with a contracted ECD and a closed channel pore. Figure was drawn using Adobe Illustrator CC version 24.3 (<https://www.adobe.com/kr/products/illustrator.html>).

interactions between the amino groups of the agonists and receptor residues differ remarkably resulting in a different extent of ECD contraction with the volume of the agonist binding pocket smallest in the glycine-bound structure³⁸. Since our measurements were performed under equilibrium conditions, our thermophoretic data therefore most likely reflect structural changes between the resting conformation, with an open ECD, and one or multiple intermediate states, as well as the open state, were the ECD is contracted (Fig. 5a). Thus, our MST measurements would reflect exclusively the agonist-induced conformational change within the ECD, whereas the electrophysiological measurements determine the general ability of the agonist to open the ion channel (aEC₅₀ value). Most strikingly, our MST measurements revealed different conformational changes of the ECD induced by taurine compared to the full agonist glycine. Therefore, we assume that the interactions between taurine and the ECD loops result in a lesser extent of ECD contraction, and therefore to the observed decreased thermophoretic mobility. This indicates that glycine- and taurine-binding induces a different degree of conformational change in the ECD and that the extent of agonist-induced ECD closure is correlated with the efficacy of agonists.

Since we cannot discriminate in our MST measurements between distinct closed ECD conformations, two general activation models for partial agonists can be envisaged (Fig. 5b). First, the taurine-induced conformation reflects a closed intermediate state that further adopts the same closed ECD conformation as seen for glycine during full activation (Fig. 5b, upper row). Second, the taurine-induced conformation reflects the final open conformation, without reaching a fully contracted ECD conformation (Fig. 5b, lower row). However, recent findings support the existence of an intermediated taurine-bound state, that is characterized by a lesser degree of ECD rotation³⁸.

Depending on the cell system analyzed, the GlyR displays in electrophysiological measurements a remarkable difference in the apparent affinity (aEC₅₀) of its agonists⁴. Thus, the apparent affinity of an agonist is not exclusively determined by its specific stereochemical properties. Previous studies supposed that intermolecular cooperativity at higher receptor expression levels may influence agonist affinity in different cell systems³⁹. Our experiments show that the large variability of the aEC₅₀ for glycine observed in different cell systems (HEK293 vs. oocyte) is not correlated with the efficiency to induce a contraction within the ECD (cEC₅₀) after glycine binding. In addition, the cEC₅₀ values in HEK293 and oocytes are similar to the aEC₅₀ value obtained from electrophysiological measurements in HEK293 cells, indicating an efficient receptor activation in HEK293 cells once the ECD has closed, consistent with previous single-channel measurements^{9,10,20}. As a direct consequence, the receptor equilibrium lies strongly on the ligand-bound, open conformation. In contrast, while the cEC₅₀ is unchanged in oocytes, the aEC₅₀ apparent affinity is decreased. We therefore conclude, that the decreased apparent affinity of GlyR in oocytes probably arise from a limited ability to open the channel pore once the ECD is closed, rather than the ability to induce a conformational change in the ECD layer upon glycine binding (Fig. 5c). We speculate that the impaired coupling of the ECD and the TMD is driven (i) by lipid or sterol modulations, as described for other members of pLGICs^{40–42} and supported by recent findings supposing interactions between glycine receptors and cholesterol⁴³ or (ii) by the impact of the ICD⁴⁴. This would explain the high variability of aEC₅₀ values seen upon electrophysiological measurements of GlyRs in the brain and in different heterologous expression systems. Thus, the apparent agonist-affinities of the GlyR obtained in electrophysiological measurements are likely determined by conformational transitions after the agonist-induced ECD closure which is in agreement with several postulated intermediate shut states between the resting and open conformation, as indicated by different primed or flipped schemas. Our data may also have some implications for the understanding of the differential impact of (i) mutations⁴⁵ and modulators²⁵ in the ECD and (ii) the TMD and ICD⁴⁴ at the GlyR in affecting partial agonism. Therefore mutations and modulators acting in the ECD might affect the conformational change in the ECD layer upon agonist binding whereas modulators acting in the TMD and the ICD may alter intermediate shut states between the resting and open conformation. Future work will need to explore these possibilities by testing the effects of mutations, modulators and the ICD on conformational states by thermophoretic analysis of the GlyR extracted in SMA-copolymer nanodiscs enabling the receptor to occupy physiologically relevant states.

In summary, by analyzing conformational states of the GlyR by MST, our results indicate that first partial agonism in the pLGIC family is reflected by the adaption of distinct receptor conformations and second that modulation within the TMD region and/or the ICD causes the variable apparent affinities seen in different cell systems. Therefore, our approach provides an easy access to correlate structural and functional impacts of ligand binding and may also help in the mechanistic understanding of positive allosteric modulators as well as in rationalized drug design.

Data availability

All data supporting the findings of this study are available within the article or are available from the corresponding author upon reasonable request. All cDNA constructs are available from the corresponding author based on reasonable request.

Received: 27 May 2020; Accepted: 10 September 2020

Published online: 06 October 2020

References

1. Plested, A. J. R. Structural mechanisms of activation and desensitization in neurotransmitter-gated ion channels. *Nat. Struct. Mol. Biol.* **23**, 494–502 (2016).
2. Lemoine, D. *et al.* Ligand-gated ion channels: new insights into neurological disorders and ligand recognition. *Chem. Rev.* **112**, 6285–6318 (2012).
3. Colquhoun, D. & Lape, R. Allosteric coupling in ligand-gated ion channels. *J. Gen. Physiol.* **140**, 599–612 (2012).
4. Lynch, J. Molecular structure and function of the glycine receptor chloride channel. *Physiol. Rev.* **84**, 1051–1095 (2004).
5. Legendre, P. The glycinergic inhibitory synapse. *Cell. Mol. Life Sci.* **58**, 760–793 (2001).

6. Lehmann, T., Gloveli, T., Grantyn, R. & Meier, J. C. Glycinergic tonic inhibition of hippocampal neurons with depolarizing GABAergic transmission elicits histopathological signs of temporal lobe epilepsy. *J. Cell. Mol. Med.* **12**, 2848–2866 (2008).
7. Langosch, D., Thomas, L. E. O. & Betz, H. Conserved quaternary structure of ligand-gated ion channels: the postsynaptic glycine receptor is a pentamer. *Proc. Natl. Acad. Sci. USA* **85**, 7394–7398 (1988).
8. Du, J., Lu, W., Wu, S., Cheng, Y. & Gouaux, E. Glycine receptor mechanism elucidated by electron cryo-microscopy. *Nature* **526**, 224–229 (2015).
9. Burzomato, V., Beato, M., Groot-kormelink, P. J., Colquhoun, D. & Sivilotti, L. G. Single-channel behavior of heteromeric $\alpha 1\beta$ glycine receptors: an attempt to detect a conformational change before the channel opens. *J. Neurosci.* **24**, 10924–10940 (2004).
10. Lape, R., Colquhoun, D. & Sivilotti, L. G. On the nature of partial agonism in the nicotinic receptor superfamily. *Nature* **454**, 722–727 (2008).
11. Schmieden, V., Kuhse, J. & Betz, H. A novel domain of the inhibitory glycine receptor determining antagonist efficacies: further evidence for partial agonism resulting from self-inhibition. *Mol. Pharmacol.* **56**, 464–472 (1999).
12. Bormann, J. & Rundstrom, N. Residues within transmembrane segment M2 determine chloride conductance of glycine receptor homo- and hetero-oligomers. *EMBO J.* **12**, 3729–3737 (1993).
13. Lynch, J. W. *et al.* Identification of intracellular and extracellular domains mediating signal transduction in the inhibitory glycine receptor chloride channel. *EMBO J.* **16**, 110–120 (1997).
14. Laube, B., Langosch, D., Betz, H. & Schmieden, V. Hyperekplexia mutations of the glycine receptor unmask the inhibitory subsite for beta-amino-acids. *NeuroReport* **6**, 897–900 (1995).
15. Saint Janan, D., David-watine, B., Korn, H. & Bregestovski, P. Activation of human $\alpha 1$ and $\alpha 2$ homomeric glycine receptors by taurine and GABA. *J. Physiol.* **535**, 741–755 (2001).
16. McCool, B. A. & Botting, S. K. Characterization of strychnine-sensitive glycine receptors in acutely isolated adult rat basolateral amygdala neurons. *Brain Res.* **859**, 341–351 (2000).
17. Hussy, N., Deleuze, C., Pantaloni, A., Desarm, M. G. & Endocrines, N. Agonist action of taurine on glycine receptors in rat supraoptic magnocellular neurones: possible role in osmoregulation. *J. Physiol.* **502**, 609–621 (1997).
18. Wang, D., Xu, T., Pang, Z., Li, J. & Akaike, N. Taurine-activated chloride currents in the rat sacral dorsal commissural neurons. *Brain Res.* **792**, 41–47 (1998).
19. Huang, X., Chen, H., Michelsen, K., Schneider, S. & Shaffer, P. L. Crystal structure of human glycine receptor- $\alpha 3$ bound to antagonist strychnine. *Nature* **526**, 277–280 (2015).
20. Purohit, P., Mitra, A. & Auerbach, A. A stepwise mechanism for acetylcholine receptor channel gating. *Nature* **446**, 930–933 (2007).
21. Haeger, S. *et al.* An intramembrane aromatic network determines pentameric assembly of Cys-loop receptors. *Nat. Struct. Mol. Biol.* **17**, 90–98 (2010).
22. Bergeron, M. J. *et al.* Frog oocytes to unveil the structure and supramolecular organization of human transport proteins. *PLoS ONE* **6**, e21901 (2011).
23. Tayyab, S., Qamar, W. & Islam, M. Size exclusion chromatography and size exclusion HPLC of proteins. *Biochem. Educ.* **19**, 149–152 (1991).
24. Bernhard, M., Diefenbach, M., Biesalski, M. & Laube, B. Electrical sensing of phosphonates by functional coupling of phosphonate binding protein PhnD to solid-state nanopores. *ACS Sensors* **5**, 234–241 (2020).
25. Laube, B., Kuhse, J. & Betz, H. Kinetic and mutational analysis of Zn^{2+} modulation of recombinant human inhibitory glycine receptors. *J. Physiol.* **522**, 215–230 (2000).
26. Dörr, J. M. *et al.* Detergent-free isolation, characterization, and functional reconstitution of a tetrameric K^+ channel: the power of native nanodiscs. *Proc. Natl. Acad. Sci.* **111**, 18607–18612 (2014).
27. Knowles, T. J. *et al.* Membrane proteins solubilized intact in lipid containing nanoparticles bounded by styrene maleic acid copolymer. *J. Am. Chem. Soc.* **131**, 7484–7485 (2009).
28. Long, A. R. *et al.* A detergent-free strategy for the reconstitution of active enzyme complexes from native biological membranes into nanoscale discs. *BMC Biotechnol.* **13**, 41 (2013).
29. Seidel, S. A. I. *et al.* Microscale thermophoresis quantifies biomolecular interactions under previously challenging conditions. *Methods* **59**, 301–315 (2013).
30. Dühr, S. & Braun, D. Why molecules move along a temperature gradient. *Proc. Natl. Acad. Sci. U.S.A.* **103**, 19678–19682 (2006).
31. Farroni, J. S. & McCool, B. A. strychnine-sensitive glycine receptors. *BMC Pharmacol.* **4**, 1–10 (2004).
32. Del Castillo, J. & Katz, B. Interaction at end-plate receptors between different choline derivatives. *Proc. R. Soc. Lond. B* **146**, 369–381 (1957).
33. Corradi, J. & Bouzat, X. C. Unraveling mechanisms underlying partial agonism in 5-HT 3 A receptors. *J. Neurosci.* **34**, 16865–16876 (2014).
34. Jin, R., Banke, T. G., Mayer, M. L., Traynelis, S. F. & Gouaux, E. Structural basis for partial agonist action at ionotropic glutamate receptors. *Nat. Neurosci.* **6**, 803–810 (2003).
35. Salazar, H., Eibl, C., Chebli, M. & Plested, A. Mechanism of partial agonism in AMPA-type glutamate receptors. *Nat. Commun.* **8**, 1–11 (2017).
36. Pless, S. A. *et al.* A cation- π interaction in the binding site of the glycine receptor is mediated by a phenylalanine residue. *J. Neurosci.* **28**, 10937–10942 (2008).
37. Yu, R. *et al.* Agonist and antagonist binding in human glycine receptors. *Biochemistry* **53**, 6041–6051 (2014).
38. Yu, J. *et al.* Mechanism of gating and partial agonist action in the glycine receptor. Preprint at <https://biorxiv.org/content/10.1101/786632v1> (2019).
39. Taleb, O. & Betz, H. Expression of the human glycine receptor $\alpha 1$ subunit in *Xenopus* oocytes: apparent affinities of agonists increase at high receptor density. *EMBO J.* **13**, 1318–1324 (1994).
40. Hénault, C. M. *et al.* A lipid site shapes the agonist response of a pentameric ligand-gated ion channel. *Nat. Chem. Biol.* **15**, 1156–1164 (2019).
41. Baenziger, J. E., Hénault, C. M., Therien, J. P. D. & Sun, J. Nicotinic acetylcholine receptor-lipid interactions: mechanistic insight and biological function. *BBA Biomembr.* **1848**, 1806–1817 (2015).
42. Salari, R., Murlidaran, S. & Brannigan, G. A Predicted binding site for cholesterol on the GABA A receptor. *Biophys. J.* **106**, 1938–1949 (2014).
43. Ferraro, N. A. & Cascio, M. Cross-linking-mass spectrometry studies of cholesterol interactions with human $\alpha 1$ glycine receptor. *Anal. Chem.* **90**, 2508–2516 (2018).
44. Ivica, J. *et al.* The intracellular domain of homomeric glycine receptors modulates agonist efficacy. *J. Biol. Chem.* <https://doi.org/10.1074/jbc.RA119.012358> (2020).
45. Schmieden, V., Kuhse, J. & Betz, H. Mutation of glycine receptor subunit creates beta-alanine receptor responsive to GABA. *Science* **262**, 256–258 (1993).

Acknowledgements

This work has been supported in the frame of the LOEWE project iNAPO by the Hessen State Ministry of Higher Education, Research and the Arts. The authors are grateful to Rajvinder Kaur for critical reading of

the manuscript. The authors acknowledge support by the German Research Foundation and the Open Access Publishing Fund of Technische Universität Darmstadt.

Author contributions

M.B. performed experiments and analyzed the data. M.B. and B.L. wrote the paper.

Funding

Open Access funding enabled and organized by Projekt DEAL.

Competing interests

The authors declare no competing interests.

Additional information

Supplementary information is available for this paper at <https://doi.org/10.1038/s41598-020-73157-2>.

Correspondence and requests for materials should be addressed to B.L.

Reprints and permissions information is available at www.nature.com/reprints.

Publisher's note Springer Nature remains neutral with regard to jurisdictional claims in published maps and institutional affiliations.



Open Access This article is licensed under a Creative Commons Attribution 4.0 International License, which permits use, sharing, adaptation, distribution and reproduction in any medium or format, as long as you give appropriate credit to the original author(s) and the source, provide a link to the Creative Commons licence, and indicate if changes were made. The images or other third party material in this article are included in the article's Creative Commons licence, unless indicated otherwise in a credit line to the material. If material is not included in the article's Creative Commons licence and your intended use is not permitted by statutory regulation or exceeds the permitted use, you will need to obtain permission directly from the copyright holder. To view a copy of this licence, visit <http://creativecommons.org/licenses/by/4.0/>.

© The Author(s) 2020

Chapter II: The N-terminal domain of the GluN3A subunit determines the efficacy of glycine-activated NMDA receptors

This chapter has been published in:

Mesic I, Madry C, Geider K, **Bernhard M**, Betz H, Laube B. *The N-terminal domain of the GluN3A subunit determines the efficacy of glycine-activated NMDA receptors*. *Neuropharmacology*. 2016 Jun; 105:133-141. doi: 10.1016/j.neuropharm.2016.01.014.

Contributions:

M.B. hat die *in silico* Modellierung durchgeführt und analysiert. M.B. hat Figure 3a erstellt.
M.B. hat den Abschnitt 2.5. *in silico* prediction verfasst.

I.M., C.M., K.G. und entwarfen und führten die restlichen Experimente durch.

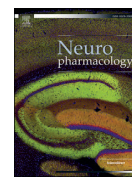
I.M., K.G. und B.L. analysierten die restlichen Daten

I.M., C.M., H.B. und B.L. schrieben das Manuskript



Contents lists available at ScienceDirect

Neuropharmacology

journal homepage: www.elsevier.com/locate/neuropharm

The N-terminal domain of the GluN3A subunit determines the efficacy of glycine-activated NMDA receptors



Ivana Mesic^{a, b, 2}, Christian Madry^{a, 1, 2}, Kirsten Geider^b, Max Bernhard^b, Heinrich Betz^{a, c}, Bodo Laube^{a, b, *}

^a Department of Neurochemistry, Max-Planck-Institute for Brain Research, Deutschordenstrasse 46, 60528 Frankfurt am Main, Germany

^b Department of Neurophysiology and Neurosensory Systems, Technische Universität Darmstadt, Schnittspahnstrasse 3, 64287 Darmstadt, Germany

^c Max-Planck-Institute for Medical Research, Jahnstrasse 29, 69120 Heidelberg, Germany

ARTICLE INFO

Article history:

Received 9 September 2015

Received in revised form

6 January 2016

Accepted 7 January 2016

Available online 9 January 2016

Keywords:

Excitatory glycine receptor
N-methyl-D-aspartate receptor
N-terminal domain
Receptor structure-function
Structural model
Xenopus

ABSTRACT

N-methyl-D-aspartate (NMDA) receptors composed of glycine-binding GluN1 and GluN3 subunits function as excitatory glycine receptors that respond to agonist application only with a very low efficacy. Binding of glycine to the high-affinity GluN3 subunits triggers channel opening, whereas glycine binding to the low-affinity GluN1 subunits causes an auto-inhibition of the maximal glycine-inducible receptor current (I_{max}). Hence, competitive antagonists of the GluN1 subunit strongly potentiate glycine responses of wild type (wt) GluN1/GluN3 receptors. Here, we show that co-expression of N-terminal domain (NTD) deleted GluN1 (GluN1^{ΔNTD}) and GluN3 (GluN3^{ΔNTD}) subunits in *Xenopus* oocytes generates GluN1/GluN3 receptors with a large increase in the glycine-inducible I_{max} accompanied by a strongly impaired GluN1 antagonist-mediated potentiation. Affinity purification after metabolic or surface labeling revealed no differences in subunit stoichiometry and surface expression between wt GluN1/GluN3A and mutant GluN1^{ΔNTD}/GluN3A^{ΔNTD} receptors, indicating a specific effect of NTD deletions on the efficacy of receptor opening. Notably, GluN1/GluN3A^{ΔNTD} receptors showed a similar increase in I_{max} and a greatly reduced GluN1 antagonist-mediated current potentiation as GluN1^{ΔNTD}/GluN3A^{ΔNTD} receptors, whereas the glycine-induced currents of GluN1^{ΔNTD}/GluN3A receptors resembled those of wt GluN1/GluN3A receptors. Furthermore, oxidative crosslinking of the homophilic GluN3A NTD intersubunit interface in mutant GluN1/GluN3A^{R319C} receptors caused both a decrease in the glycine-induced I_{max} concomitantly with a marked increase in GluN1 antagonist-mediated current potentiation, whilst mutations within the intrasubunit region linking the GluN3A NTD to the ligand binding domain had opposite effects. Together these results show that the GluN3A NTD constitutes a crucial regulatory determinant of GluN1/GluN3A receptor function.

© 2016 Elsevier Ltd. All rights reserved.

1. Introduction

Heterooligomeric N-methyl-D-aspartate (NMDA) receptors are members of the tetrameric ionotropic glutamate receptor (iGluR) family that display particular pharmacological and functional properties (Dingledine et al., 1999). A unique feature of conventional NMDA receptors composed of two glycine-binding GluN1

and two glutamate-binding GluN2 subunits (Laube et al., 1998) is that the simultaneous binding of two agonists, glycine and glutamate, is required for efficient channel opening (Kuryatov et al., 1994; Laube et al., 1997). In contrast, NMDA receptors composed of the glycine-binding GluN1 and GluN3 subunits ('excitatory glycine receptors') are activated by glycine alone (Chatterton et al., 2002). However, GluN1/GluN3 receptors generate only rather small currents; this has been attributed to glycine-binding to the GluN1 subunit causing a strong inhibition of receptor function (Awobuluyi et al., 2007; Madry et al., 2007a). Thus, glycine binding to the GluN1 subunit has opposite consequences on GluN1/GluN2 and GluN1/GluN3 receptor function: it is a prerequisite for efficient activation of conventional GluN1/GluN2 receptors (Kuryatov et al., 1994) but inhibits GluN1/GluN3 receptor gating (Madry et al., 2007a). So far,

* Corresponding author. Department of Neurophysiology and Neurosensory Systems, TU-Darmstadt, Schnittspahnstrasse 3, 64287 Darmstadt, Germany.

E-mail address: laube@bio.tu-darmstadt.de (B. Laube).

¹ Present address: Department of Physiology, University College London, Gower Street, London, WC1E 6BT, UK.

² These authors made equal contributions.

the molecular determinants of these differential effects of glycine binding to the GluN1 subunit have not been elucidated.

NMDA receptor subunits share a common modular design characterized by: i) an extracellular N-terminal domain (NTD) of about 400 amino acids, which has been implicated in receptor oligomerization, trafficking and modulation; ii) two extracellular segments (S1S2) forming the ligand binding domain (LBD); iii) three transmembrane domains and an intramembrane re-entrant loop, which determines receptor permeation properties; and iv) an intracellular carboxyterminal tail that interacts with postsynaptic scaffolding and signal transduction proteins (Dingledine et al., 1999). Based on structural and functional studies, a mechanistic model for the activation of the conventional NMDA receptor has emerged during the past years (Mayer, 2006; Lee et al., 2014). Accordingly, agonist occupation of both the GluN1 and GluN2 LBDs, which are arranged as hetero-dimers in a 'back-to-back' fashion (Furukawa et al., 2005; Schuler et al., 2008), leads to the closure of both LBDs and thereby generates sufficient conformational strain to initiate channel opening (Furukawa et al., 2005; Inanobe et al., 2005). The efficacy of conventional NMDA receptors is controlled by the NTDs (Yuan et al., 2009b) and can be modulated upon binding of modulators, resulting in a rearrangement of the dimer interface (Gielen et al., 2008; Borschel et al., 2011). For GluN1/GluN3 receptors, glycine binding to the high-affinity GluN3-3D alone is sufficient to open the ion channel (Madry et al., 2007a). However, glycine binding to the low-affinity GluN1 LBD auto-inhibits GluN1/GluN3 receptor function, thereby reducing ion flux (Wobuluyi et al., 2007; Madry et al., 2007a). Consistent with these differential effects of glycine binding to the GluN1 and GluN3 subunits, antagonists of and mutations within the GluN1 LBD greatly potentiate maximal glycine-inducible GluN1/GluN3 receptor currents (I_{max}) (Madry et al., 2007a).

In this study, we show that deletion of both the GluN1- and GluN3A NTDs potentially increased the glycine-induced I_{max} without affecting receptor assembly and plasma membrane insertion. This increase in I_{max} was accompanied by a reduced potentiation of the glycine-induced currents by the GluN1-specific glycine binding site antagonist MDL-29951 (MDL). Notably, the maximal inducible currents in the presence of both the agonist glycine and the GluN1 binding site antagonist MDL were similar for both wt and NTD-deleted GluN1/GluN3A receptors. Hence, NTD-deletion markedly enhanced GluN1/GluN3A receptor efficacy. Similar effects as seen with GluN1^{ΔNTD}/GluN3A^{ΔNTD} receptors were obtained upon deletion of the GluN3A NTD alone, and when introducing point mutations within the region linking the GluN3A NTD to the adjacent 3D. In contrast, oxidative crosslinking of the putative homophilic intersubunit GluN3A NTD interface had the opposite effect resulting in a reduced glycine I_{max} and an even stronger MDL-potentiation). Together our results indicate that a homophilic intersubunit interaction amongst the GluN3A NTDs and the transition region between GluN3A NTD and -LBD constitute major structural determinants underlying the low efficacy of glycine-activated GluN1/GluN3A receptors.

2. Material and methods

2.1. DNA constructs, oocyte expression and electrophysiology

The GluN1-1a (splice variant 1a), GluN3A, and GluN3B expression constructs in the pNKS2 vector used have been described previously (Madry et al., 2007a). The NTD-deleted GluN1^{ΔNTD} and GluN3A^{ΔNTD} constructs were generated by simply excising the nucleotide sequence encoding the NTD of the respective wt pNKS2 constructs of the GluN1 and GluN3A subunits, respectively, as described previously (Madry et al., 2007b, 2008). The GluN3B^{ΔNTD}

construct in the pNKS2 vector lacks the sequence encoding amino acids 31–396 of the respective mature GluN3B protein. Single point mutations were generated via site-directed mutagenesis (QuikChange XL Site-Directed Mutagenesis Kit, Stratagene) and confirmed by DNA sequencing (Eurofins MWG Operon). All constructs were linearized and transcribed into cRNA (mCAP mRNA Capping Kit, Ambion) as described by Madry et al. (2008). For electrophysiological analysis, *Xenopus laevis* oocytes were injected with 50 ng in a volume of 50 nl of the respective wt or NTD-deleted GluN1 and GluN3 cRNAs at a ratio of 1:3. Oocytes were isolated and maintained as described previously (Laube et al., 1997). 3–4 days after injection, whole-cell currents were recorded by two-electrode voltage-clamp according to Laube et al. (1997). For treatments with dithiothreitol (DTT), oocytes were superfused with 2 mM DTT for 100 s before applying glycine in the presence of 2 mM DTT as described by Lynagh et al. (2013). MDL-29951 was obtained from RBI Sigma (Taufkirchen, Germany).

2.2. Metabolic [³⁵S]methionine labeling, purification and SDS-PAGE of NMDA receptor complexes

After cRNA injection, oocytes were labeled overnight by incubation in [³⁵S]methionine (>40 TBq/mmol, Amersham Biosciences) at ~100 MBq/ml (0.2 MBq per oocyte) and thereafter chased for additional 2 days as described (Schuler et al., 2008). Receptor complexes were purified from dodecylmaltoside extracts of the labeled oocytes via a His₆-tag added to the GluN1 and GluN1^{ΔNTD} C-termini by using Ni²⁺-NTA agarose (Qiagen) chromatography as described previously (Madry et al., 2007b). [³⁵S]-Methionine-labeled protein samples were solubilized in SDS sample buffer containing 20 mM dithiothreitol and electrophoresed in parallel with molecular mass markers (SeeBlue® Plus2 Pre-Stained Standard, Invitrogen) on 8% tricine-SDS-polyacrylamide gels. Gels were blotted, fixed, dried, and exposed to BioMax MR films (Kodak, Stuttgart, Germany) at –80 °C. The radioactivity of individual protein bands was quantified using a PhosphorImager (Molecular Dynamics) and analyzed using the software package ImageQuant.

2.3. Surface labeling with Cy5-NHS-ester

Three days after the injection of cRNAs, the injected and non-injected control oocytes were surface-labeled with 65 μmol of Cy5-NHS-ester dye (Amersham Biosciences) and solubilized for affinity purification as described above. Gels containing Cy5-labeled protein samples were scanned with a gel imager (Typhoon 9400, Amersham Biosciences) as described (Madry et al., 2007b).

2.4. Glycosylation assay

To discriminate between mature and immature receptor complexes, 10 μl of the affinity-purified receptor were incubated in reducing sample buffer (20 mM DTT, 1% (w/v) SDS) containing 1% (w/v) octylglucoside with 5 U endoglycosidase H (Endo H) or peptide:N-glycosidase F (PNGase F; both NEB, Frankfurt, Germany) at 37 °C for 1 h, and protein samples were analyzed by SDS-PAGE as described above.

2.5. In silico prediction

Molecular modeling of the GluN1/GluN3A receptor was based on the crystal structure of the GluN1/GluN2B receptor (Brookhaven Protein Data Bank entry 4TLL) using SWISS-MODEL as described (Bordoli et al., 2009). Local energy minimization and disulfide bond creation were performed using DeepView (<http://www.expasy.org/>)

spdbv/) (Guex and Peitsch, 1997). Figures were made using PyMOL 1.2 (<http://www.pymol.org>). For all analyses, values are given as means \pm SEM. Statistical significance was determined at the $p < 0.05$ (*), $p < 0.01$ (**) and $p < 0.001$ (***) levels using Student's *T*-test.

3. Results

3.1. Deletion of the N-terminal domains of the GluN1 and GluN3 subunits results in an increase of maximal inducible glycine currents

Previous studies have shown that deletion of the N-terminal domains of NMDA receptor subunits does not abrogate the assembly and surface targeting of NMDA receptors in heterologous expression systems (Madry et al., 2007b, 2008; Costa et al., 2011; Smothers et al., 2013). Here, we found that fully NTD-deleted GluN1^{ΔNTD}/GluN3A^{ΔNTD} receptors produced ~13-fold larger maximal glycine-inducible currents (I_{\max}) than wild type (wt) GluN1/GluN3A receptors upon heterologous expression in *Xenopus* oocytes (GluN1/GluN3A: $0.15 \pm 0.02 \mu\text{A}$, vs. GluN1^{ΔNTD}/GluN3A^{ΔNTD}: $1.90 \pm 0.23 \mu\text{A}$, $p < 0.001$; Fig. 1A and Table 1). Similar to GluN1/GluN3A receptors, deletions of the entire NTDs from GluN1/GluN3B receptors also led to a similar increase of the glycine-induced I_{\max} (GluN1/GluN3B: $0.03 \pm 0.002 \mu\text{A}$, GluN1^{ΔNTD}/GluN3B^{ΔNTD}: $0.7 \pm 0.18 \mu\text{A}$; $p < 0.001$; Fig. 1A and Table 1). NTD deletions also caused a decrease of the apparent glycine affinity as indicated by higher EC_{50} values in comparison to the full-length wt receptors (GluN1/GluN3A: $6.5 \pm 1.2 \mu\text{M}$ vs. GluN1^{ΔNTD}/GluN3A^{ΔNTD}: $33 \pm 2.4 \mu\text{M}$, $p < 0.05$; and GluN1/GluN3B: $6.0 \pm 0.3 \mu\text{M}$ vs. GluN1^{ΔNTD}/GluN3B^{ΔNTD}: $11 \pm 0.51 \mu\text{M}$, $p < 0.05$, see Table 1 and Madry et al., 2007a). Thus, deletions of the entire NTDs from both GluN1/GluN3A and GluN1/GluN3B receptors strongly increased their glycine-evoked currents.

To establish whether the enhanced I_{\max} of NTD-deleted GluN1/GluN3 receptors may reflect changes in receptor expression we compared the protein levels and subunit composition of wt GluN1/GluN3A and GluN1^{ΔNTD}/GluN3A^{ΔNTD} receptors. To this end, hexahistidyl-tagged GluN1 (GluN1-His) or GluN1^{ΔNTD} (GluN1^{ΔNTD}-His) subunits were co-expressed with the wt or NTD-deleted GluN3A subunit. Analyses of maximal glycine-inducible currents of GluN1^{ΔNTD}-His/GluN3A^{ΔNTD} receptors revealed that they were potentiated to similar extents as the untagged GluN1^{ΔNTD}/GluN3A^{ΔNTD} receptor (>20-fold; compare Fig. 1A and B). After metabolic labeling of the oocytes with [³⁵S]methionine and affinity purification of the tagged GluN1-His/GluN3A and GluN1^{ΔNTD}-His/GluN3A^{ΔNTD} receptors on Ni²⁺-NTA agarose as described (Schuler et al., 2008), receptor complexes were analyzed by SDS-PAGE and autoradiography. GluN1/GluN3A receptors showed two protein bands (Fig. 1B, right, lane 1) of similar apparent intensities as GluN1^{ΔNTD}/GluN3A^{ΔNTD} receptors (Fig. 1B, right, lane 2). In order to determine the respective subunit stoichiometries, we quantified the relative intensities of the radioactive bands (Fig. 1C, left and middle). Based on the total number of methionine residues per subunit (30 methionines per GluN1 and 33 methionines per GluN3A; 18 methionines per GluN1^{ΔNTD} and 16 methionines per GluN3A^{ΔNTD}), the determined intensities corresponded to ratios for GluN1/GluN3A (1.0:1.07) and GluN1^{ΔNTD}/GluN3A^{ΔNTD} receptors (1.0:0.93) that are consistent with a 2 GluN1: 2 GluN3A subunit stoichiometry of the tetrameric receptor complex (Fig. 1C, right; see also Schuler et al., 2008). Co-expression of a 5-fold excess of the GluN3A or GluN3A^{ΔNTD} subunits over the GluN1 or rather GluN1^{ΔNTD} subunit did not alter the relative subunit ratios, indicating an invariant subunit stoichiometry of both the GluN1/GluN3A and the GluN1^{ΔNTD}/GluN3A^{ΔNTD} receptors (data not shown).

We also examined the cell-surface expression of the wt and the NTD-deleted GluN1-His/GluN3A receptors by cell-surface labeling with the membrane-impermeable Cy5-NHS-ester dye (Schuler et al., 2008). This labeling method resulted in similar band intensities for the surface-exposed wt GluN1/GluN3A and GluN1^{ΔNTD}/GluN3A^{ΔNTD} receptors (Fig. 1D). Differential shifts in molecular masses observed upon treatment with peptide:N-glycosidase F (PNGase F) as compared to those seen with endo-glycosidase H (EndoH, specific for high-mannose type N-glycans in the endoplasmic reticulum) confirmed that both receptor proteins were complex N-glycosylated in the Golgi apparatus and hence located at the cell surface (Fig. 1D). This suggests that the increased function of NTD-deleted GluN1/GluN3A receptors cannot be attributed to enhanced expression or insertion into the plasma membrane, but represents intrinsic changes of receptor properties leading to an increased glycine efficacy.

3.2. Deletion of the NTDs of GluN1/GluN3A receptors differentially affects both GluN1/GluN3A receptor efficacy and potentiation by GluN1 glycine-site antagonists

In previous studies, we and others have shown that preventing glycine binding to the GluN1-LBD by GluN1-specific antagonists strongly potentiates GluN1/GluN3A receptor currents (Awobuluyi et al., 2007; Madry et al., 2007a). To determine whether NTD-deletions also affect GluN1 antagonist-mediated potentiation, we recorded glycine-induced currents in the absence and presence of the specific GluN1 antagonist MDL-29951 (MDL) from wt and NTD-deleted GluN1/GluN3A receptors. We found that the glycine-induced currents of GluN1^{ΔNTD}/GluN3A^{ΔNTD} receptors were only weakly potentiated by $0.2 \mu\text{M}$ MDL (~2-fold; Fig. 2A and Table 1), whereas wt GluN1/GluN3A receptors were strongly potentiated by the antagonist (>20-fold; $p < 0.001$; Fig. 2A,C, and Table 1; see also Madry et al. 2007a). Interestingly, in the presence of saturating glycine and MDL concentrations the I_{\max} values of the wt and NTD-deleted receptors were almost identical (3.4 ± 0.6 and $3.8 \pm 0.5 \mu\text{A}$; $p > 0.05$; Fig. 2D), whereas they differed >12-fold upon application of glycine alone (Fig. 2B). Thus, the NTDs of GluN1/GluN3A receptors determine not only maximal glycine-inducible currents but also antagonist-induced receptor potentiation.

Next, we assessed the impact of single NTD-deletions on glycine-mediated GluN1/GluN3A receptor currents. The I_{\max} values of GluN1/GluN3A^{ΔNTD} receptors were significantly higher ($1.12 \pm 0.25 \mu\text{A}$) than those of GluN1^{ΔNTD}/GluN3A (I_{\max} : $0.15 \pm 0.03 \mu\text{A}$; $p < 0.001$) and of wt GluN1/GluN3A (I_{\max} : $0.15 \pm 0.02 \mu\text{A}$; $p < 0.001$) receptors (Fig. 2A,B, and Table 1), but not significantly different from GluN1^{ΔNTD}/GluN3A^{ΔNTD} receptors (I_{\max} : $1.90 \pm 0.23 \mu\text{A}$, $p > 0.05$). Hence, the GluN1- and GluN3A NTDs influence the function of GluN1/GluN3A receptors differentially. When measuring the extent of MDL potentiation of the singly NTD-deleted receptors, GluN1^{ΔNTD}/GluN3A receptors were still strongly potentiated by MDL (~19-fold; Fig. 2C and Table 1), whereas GluN1/GluN3A^{ΔNTD} receptors showed only weak potentiation (~2-fold; Fig. 2C and Table 1). Again, in the presence of saturating glycine and MDL concentrations maximal inducible currents of all GluN1/GluN3A receptor combinations tested were almost identical (between 2.8 ± 0.9 and $3.8 \pm 0.5 \mu\text{A}$; $p > 0.05$; Fig. 2D). Together these results show that the GluN3A NTDs are major determinants of the efficacy of GluN1/GluN3A receptors, whereas the GluN1-NTDs seem not involved.

Since current potentiation by the GluN1 glycine-site antagonist MDL was drastically impaired in GluN1^{ΔNTD}/GluN3A^{ΔNTD} and GluN1/GluN3A^{ΔNTD} receptors, we asked whether deletion of the GluN3A NTDs affects agonist-evoked auto-inhibition caused by glycine binding to the GluN1 subunit. Co-expression of the glycine

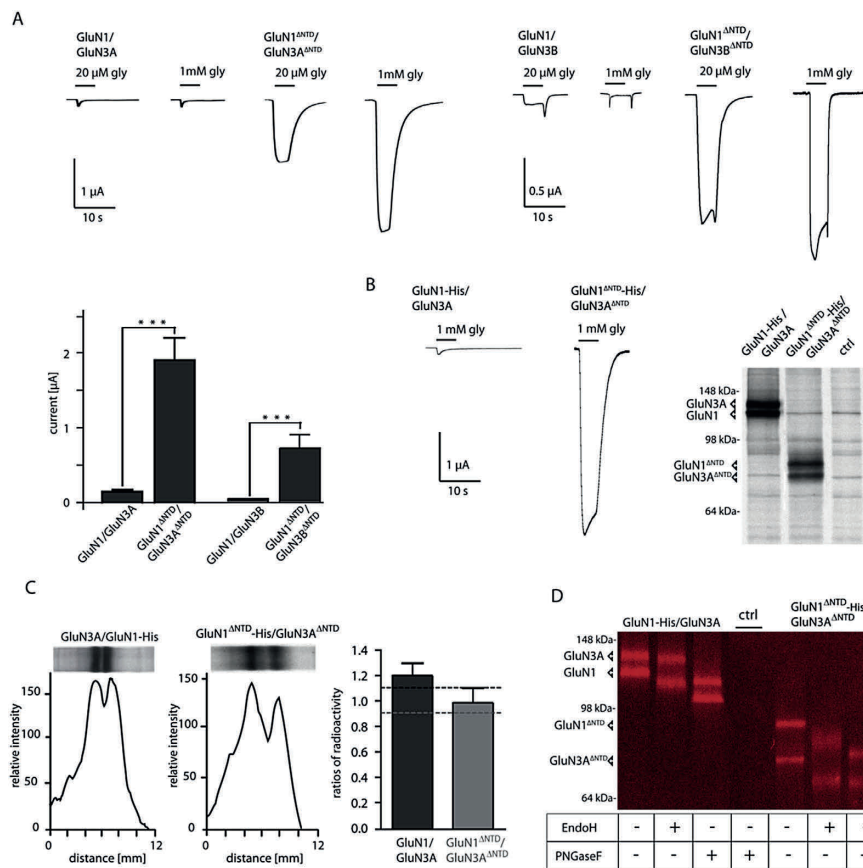


Fig. 1. Functional and biochemical analysis of wt and NTD-deleted GluN1/GluN3 receptors. (A) Example traces illustrating glycine-evoked currents of GluN1/GluN3A vs. GluN1^{NTD}/GluN3A^{NTD} receptors (left) and GluN1/GluN3B vs. GluN1^{NTD}/GluN3B^{NTD} receptors (right) in the presence of 20 μ M and 1 mM glycine, respectively. Quantification of maximal glycine-induced GluN1/GluN3 receptor currents (I_{max} ; ***, $p < 0.001$; $n = 7-16$). Note that the NTD-deleted GluN1/GluN3 receptors showed significantly larger currents compared to respective wt receptors. (B) Example traces illustrating glycine-evoked currents of the GluN1-His/GluN3A and GluN1^{NTD}-His/GluN3A^{NTD} receptors (left) in the presence of 1 mM glycine. Note that the maximal glycine-induced currents of the GluN1-His/GluN3A and GluN1^{NTD}-His/GluN3A^{NTD} receptors were similar to those obtained with the respective tagged wt constructs (see Fig. 1A). Autoradiogram of the SDS-PAGE of metabolically labeled and affinity-purified wt GluN1-His/GluN3A and GluN1^{NTD}-His/GluN3A^{NTD} receptor complexes (right). (C) For analyzing the subunit stoichiometry of wt and NTD-deleted GluN1/GluN3 NMDA receptors, gel lanes containing the [³⁵S]methionine-labeled GluN1/GluN3A-proteins were scanned using a PhosphorImager, and the relative ratios of radioactivities of the GluN1 and GluN3A subunits were determined (left and middle). Measured ³⁵S ratios of wt GluN1/GluN3A and GluN1^{NTD}/GluN3A^{NTD} receptors are in good agreement with the theoretical ratios of 1.07 and 0.93 (dashed lines), respectively, as calculated based on the number of methionine residues present per mature or NTD-deleted GluN1 and GluN3A subunit (right). (D) Comparison of the intensities of affinity-purified ³⁵S surface labeled wt GluN1/GluN3A (lanes 1–3) and GluN1^{NTD}/GluN3A^{NTD} receptors (lanes 4–6) by SDS-PAGE revealed similar surface expression levels. EndoH and PNGaseF treatment is shown below the respective lanes, indicating surface location of wt and NTD-deleted GluN1 and GluN3A subunits. ctrl, Uninjected oocytes.

Table 1
Pharmacology of recombinant wild type and mutant GluN1/GluN3A NMDA receptors.

Subunit composition	I_{max} [μ A]	EC_{50} glycine [μ M]	MDL-potential [x-fold] ^a
GluN1/GluN3A	0.15 \pm 0.02 (16)	6.5 \pm 1.2 (11)	22 \pm 2.6 (9)
GluN1 ^{NTD} /GluN3A	0.15 \pm 0.03 (8)	19 \pm 3.2* (6)	18.8 \pm 4 (6)
GluN1/GluN3A ^{NTD}	1.12 \pm 0.25*** (14)	23 \pm 0.95* (4)	3.5 \pm 0.85*** (4)
GluN1 ^{NTD} /GluN3A ^{NTD}	1.90 \pm 0.23*** (9)	33 \pm 2.4* (10)	2 \pm 0.2*** (7)
GluN1 ^{F466A} /GluN3A	2.47 \pm 0.4*** (5)	82 \pm 11** (4) [§]	1.07 \pm 0.2*** (5)
GluN1 ^{F466A} /GluN3A ^{NTD}	2.24 \pm 0.26*** (6)	69 \pm 10** (3)	1.04 \pm 0.1*** (6)
GluN1/GluN3A ^{R319Cox}	0.039 \pm 0.02** (4)	55 \pm 6.4** (3)	44.4 \pm 5.2*** (5)
GluN1/GluN3A ^{R319Cred}	0.24 \pm 0.09 (4)	5.2 \pm 0.9 (3)	17.5 \pm 3.2 (4)
GluN1/GluN3A ^{E498A}	1.64 \pm 0.29*** (9)	9.4 \pm 1.8 (4)	3.2 \pm 0.8*** (9)
GluN1/GluN3A ^{H509D}	0.48 \pm 0.11*** (8)	11 \pm 2.7 (3)	10.5 \pm 3.3*** (5)
GluN1/GluN3B	0.03 \pm 0.002 (10)	6.0 \pm 0.3 (3)	nd
GluN1 ^{NTD} /GluN3B ^{NTD}	0.7 \pm 0.18*** (9)	11 \pm 0.5* (3)	nd

Values represent means \pm SEM. Numbers of experiments given in parentheses.

* $p < 0.05$; ** $p < 0.01$; *** $p < 0.001$.

^a In the presence of 1 mM glycine and 0.2 μ M MDL-29951. [§] - taken from Madry et al. (2007a); nd – not determined.

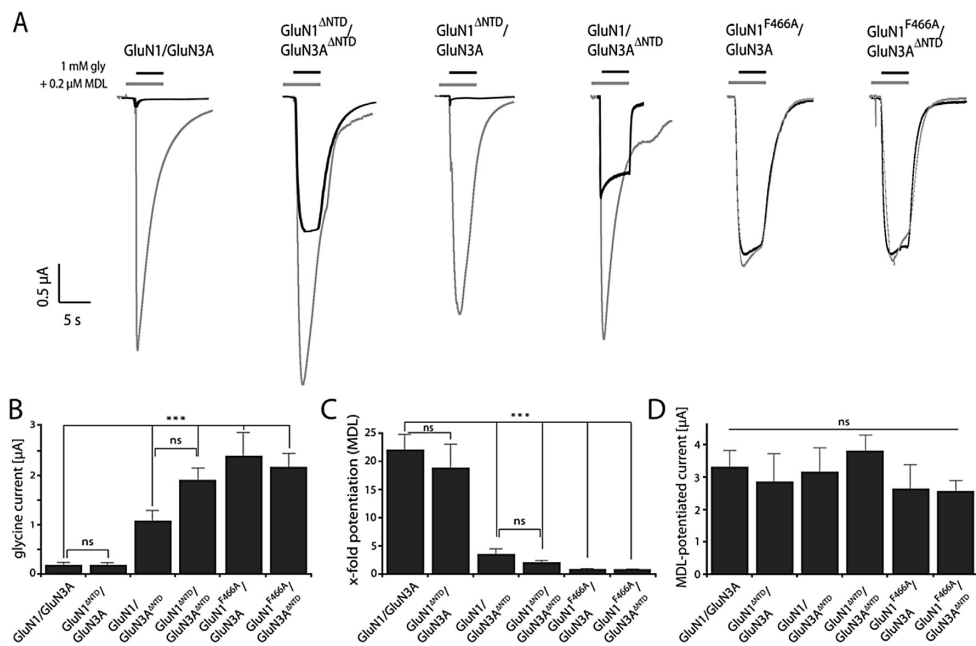


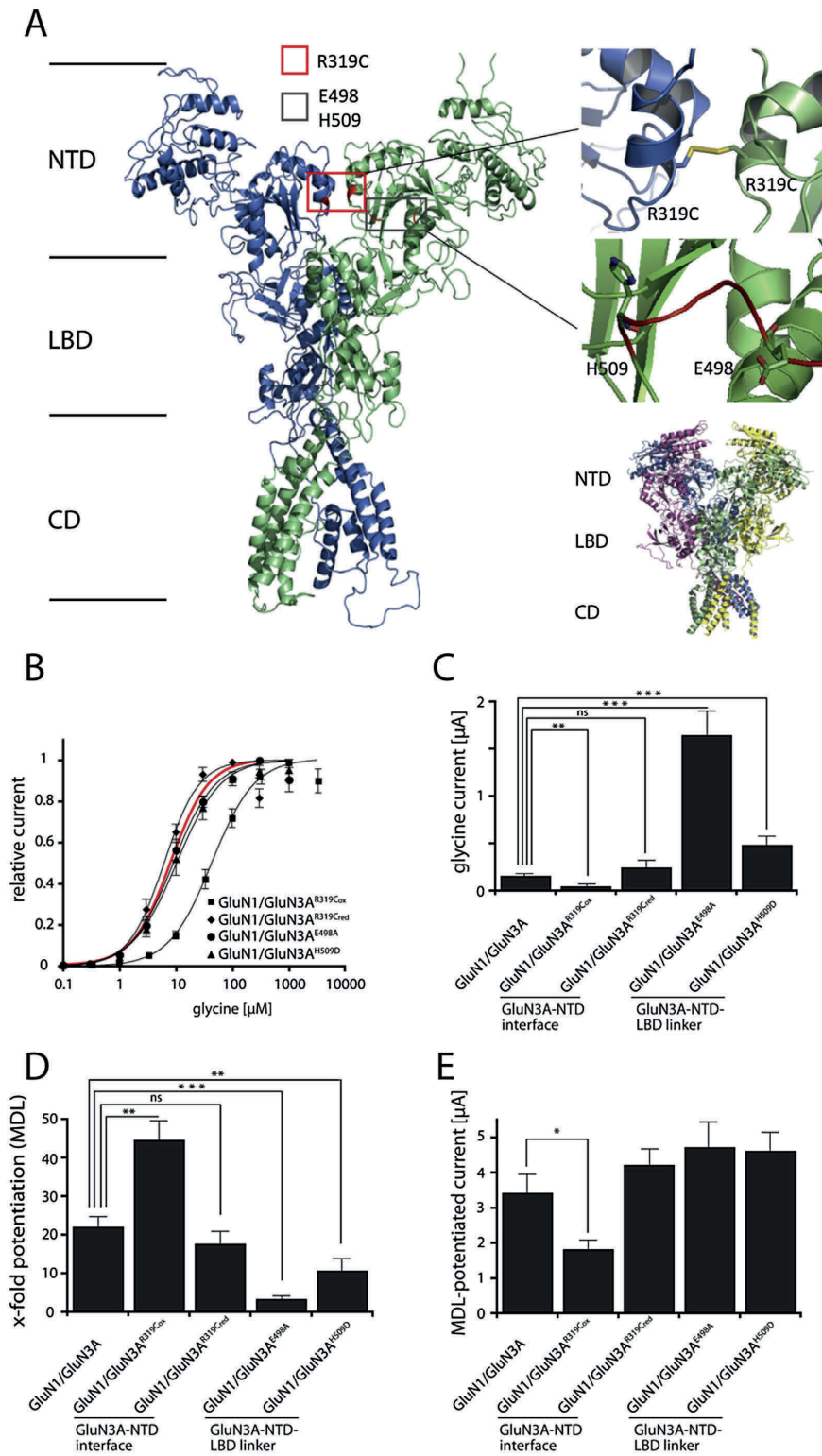
Fig. 2. Analysis of NTD-deleted GluN1/GluN3A and GluN1^{F466A}/GluN3A receptor combinations on maximal inducible receptor currents (I_{max}) and GluN1-glycine binding site antagonist (MDL)-induced potentiation. (A) Comparison of superimposed glycine- (black) and glycine/MDL-induced (gray) current traces of wt and NTD-deleted GluN1/GluN3A and GluN1^{F466A}/GluN3A receptors. (B) Quantification of maximal glycine-induced GluN1/GluN3A receptor currents (I_{max} ; ***, $p < 0.001$; $n = 7-16$). Data from GluN1/GluN3A and GluN1^{ΔNTD}/GluN3A^{ΔNTD} receptors are taken from Fig. 1A. (C) Quantification of glycine-induced currents shows that GluN1/GluN3A and GluN1^{ΔNTD}/GluN3A receptors were much stronger potentiated by MDL (0.2 μM) than GluN1/GluN3A^{ΔNTD}, GluN1^{ΔNTD}/GluN3A^{ΔNTD}, GluN1^{F466A}/GluN3A and GluN1^{F466A}/GluN3A^{ΔNTD} receptors. (D) Analysis of MDL-potentiated glycine currents (1 mM) from wt and NTD-deleted GluN1/GluN3A mutant receptors. Note that all GluN1/GluN3A receptor combinations tested generated similar maximal inducible currents in response to saturating glycine and MDL concentrations (between 2.4 and 3.8 μA ; $p > 0.05$).

binding site mutant GluN1^{F466A} (Madry et al. 2007a) with the GluN3A and GluN3A^{ΔNTD} subunits resulted in large glycine currents which were not potentiated in the presence of MDL (Fig. 2A,C). Strikingly, GluN1^{F466A}/GluN3A and GluN1^{F466A}/GluN3A^{ΔNTD} receptor currents resembled those seen with GluN1/GluN3A and GluN1^{ΔNTD}/GluN3A receptors in the presence of MDL, and with GluN1/GluN3A^{ΔNTD} and GluN1^{ΔNTD}/GluN3A^{ΔNTD} receptors in the absence of MDL (Fig. 2B,D). Hence we attribute the decrease in current potentiation by MDL seen upon deletion of the GluN3A NTDs to the selective loss of agonist-evoked auto-inhibition caused by glycine binding to the GluN1 subunit.

3.3. Oxidative crosslinking of the GluN3A NTD and mutations within the GluN3A NTD-LBD-linker region affect GluN1/GluN3A receptor efficacy

To identify molecular determinants within the GluN3-NTDs determining GluN1/GluN3A receptor efficacy, we generated a homology model of the GluN1/GluN3A receptor (Fig. 3A inset). This GluN1/GluN3A model is based on the recently published crystal structure of the GluN1/GluN2B NMDA receptor, which implicates the existence of a homophilic intersubunit interface between the GluN2B-NTDs conferring conformational mobility at the level of the NTDs (Lee et al., 2014). Based on our model, we introduced a single amino acid substitution into the $\alpha 5$ helix of the predicted interface of GluN3A NTDs by exchanging arginine 319 by a cysteine residue (GluN3A^{R319C}; see Fig. 3A with enlargement). This substitution is homologous to mutation lysine 216 to cysteine in the GluN2B subunit (GluN2B^{K216C}), a substitution assumed to decrease NTD-flexibility by forming an intersubunit disulfide bond between

the two GluN2B NTDs under non-reducing conditions (Lee et al., 2014). To investigate whether oxidative crosslinking of the GluN3A^{R319C} NTDs affects glycine efficacy, we tested for spontaneous disulfide bond formation between the GluN3A NTDs by measuring the currents of GluN1/GluN3A^{R319C} mutant receptors elicited by a saturating concentration of glycine (1 mM) in the absence or presence of the reducing agent dithiothreitol (DTT). Co-expression of the GluN3A NTD interface mutant GluN3A^{R319C} with the wt GluN1 subunit resulted in glycine-gated maximal currents that in the absence of DTT were about 4-fold smaller than those of the wt GluN1/GluN3A receptor (GluN1/GluN3A: $0.15 \pm 0.02 \mu A$, GluN1/GluN3A^{R319C}: $0.039 \pm 0.02 \mu A$; $p < 0.01$; Fig. 3C and Table 1). Notably, in the presence of 2 mM DTT the peak amplitude of glycine-induced GluN1/GluN3A^{R319C} receptor currents was increased to wt levels (GluN1/GluN3A^{R319C}: $0.24 \pm 0.09 \mu A$; Fig. 3C and Table 1), whereas the I_{max} values of wt GluN1/GluN3A receptors were not affected by DTT treatment (data not shown). This indicates that under oxidizing conditions the cysteine substitution R319C in the GluN3A NTD allows for the formation of an intersubunit disulfide bond that strengthens interface interactions amongst GluN3A NTDs by simultaneously weakening their mobility and thereby reduces agonist responses. In the presence of DTT, this disulfide bond is cleaved, and hence the I_{max} value of GluN1/GluN3A^{R319C} receptors is comparable to that of the wt GluN1/GluN3A receptor. Furthermore, the apparent glycine affinity of GluN1/GluN3A^{R319C} receptors determined in the absence of DTT was significantly lower than that of both the wt and the GluN1/GluN3A^{R319C} receptors (EC_{50} : $55 \pm 6 \mu M$ vs. 5.2 ± 0.9 and $6.5 \pm 1.2 \mu M$; $p < 0.01$; Fig. 3B and Table 1). Next we examined the effect of DTT treatment on the MDL-mediated potentiation of



glycine-gated currents of the GluN1/GluN3A^{R319C} receptor. Whereas in its oxidized, cross-linked state MDL evoked a ~45-fold potentiation with an I_{\max} of $1.81 \pm 0.3 \mu\text{A}$, it potentiated GluN1/GluN3A^{R319Cred} currents only to about wt receptor levels (~17-fold) with an I_{\max} of $4.1 \pm 0.7 \mu\text{A}$ in the presence of DTT (Fig. 3D,E and Table 1). Thus, conformational changes within the GluN3A NTDs are essential for regulating GluN1/GluN3A gating efficacy and apparent glycine affinity.

To investigate the functional impact of the GluN3A NTD-LBD linker region for transmitting conformational flexibility from the extracellular NTD domains to the LBDs, which has been shown in GluN1/GluN2 receptors (Gielen et al., 2009; Yuan et al., 2009b) to mediate NTD signaling, we introduced point mutations in a region of GluN3A which is homologous to the NTD-LBD linker region of the GluN1/GluN2B NMDA receptor (Lee et al., 2014, Fig. 3A; residues 493–512). We focussed on i) the negatively charged residue GluN3AE498, as the homologous residue in GluN2 subunits play a crucial role in determining receptor kinetics in GluN1/GluN2 receptors (Gielen et al., 2009; Yuan et al., 2009b), and ii) the aromatic side chain GluN3AH509 which, relying on the homology model, stabilizes the linker by interacting with the GluN3A NTD. Analysis of the mutant GluN1/GluN3A^{E498A} and GluN1/GluN3A^{H509D} receptors revealed significantly larger glycine-evoked currents as compared to the wt GluN1/GluN3A receptor (~11- and ~3-fold, respectively; $p < 0.001$; Fig. 3C and Table 1), whereas no differences in apparent glycine EC_{50} values were found (Fig. 3B; Table 1). Remarkably, GluN1/GluN3A^{E498A} receptors displayed an I_{\max} similar to the one obtained upon deletion of the entire GluN3A NTD in GluN1/GluN3A^{ΔNTD} receptors (Fig. 3C; see also Fig. 2B). We also examined the MDL-mediated potentiation of glycine-gated currents in the two mutant receptors; in both, it was markedly decreased as compared to wt GluN1/GluN3A receptors (GluN1/GluN3A^{E498A}: ~3-fold; and GluN1/GluN3A^{H509D}: ~11-fold; $p < 0.001$ and $p < 0.01$, respectively; Fig. 3D and Table 1). Interestingly, in the presence of saturating glycine and MDL concentrations the maximal inducible currents of wt and GluN1/GluN3A linker mutant receptors were almost identical ($p > 0.05$; Fig. 2D). Thus, in addition to the GluN3A NTDs the region linking the GluN3-NTD to the GluN3-LBD functions as an important structural determinant of the efficacy of GluN1/GluN3A receptors.

4. Discussion

In the present study, we show that deletion of the GluN3A NTDs markedly increases maximal glycine-inducible currents of recombinant GluN1/GluN3 receptors whereas deletion of the NTD of the GluN1 subunit has no effect. Since current potentiation by the GluN1 glycine-site antagonist MDL was virtually abolished in GluN1^{ΔNTD}/GluN3A^{ΔNTD} and GluN1/GluN3A^{ΔNTD} receptors, and as neither receptor assembly nor cell surface expression were altered upon NTD deletion, we attribute this result to the selective loss of

agonist-evoked auto-inhibition caused by glycine-binding to the GluN1 subunit. Cysteine substitution of residue GluN3A^{R319} within the putative GluN3A NTD subunit interface and charge neutralization or inversion at residues GluN3A^{E498} and GluN3A^{H509} in the GluN3A NTD-LBD linker region affected specifically MDL-potentiation of the glycine-inducible currents of the mutant receptors. Therefore, we suggest that in GluN1/GluN3A receptors both the putative GluN3A NTD subunit interface and the GluN3A NTD LBD linker region participate in regulating the efficacy of glycine at the GluN1 LBDs.

4.1. Roles of NTDs in NMDAR assembly and function

Although there have been numerous reports on the process of NMDA receptor assembly, its mechanism remains controversial. Some results obtained on conventional GluN1/GluN2 receptors imply that NTD interactions mediate the initial association of two subunits into a homo-dimer (Papadakis et al., 2004; Qiu et al., 2005; Farina et al., 2011). This is presumably followed by the association of the GluN1 and GluN2 homo-dimers into the final tetrameric NMDAR, an idea which is based on studies of AMPA and kainate receptor assembly (Hansen et al., 2010). However, we and others have shown that deleting the NTDs does not affect the assembly of conventional GluN1/GluN2 receptors (Fayyazuddin et al., 2000; Hu and Zheng, 2005; Madry et al., 2007b), which supports the view that the NTDs of conventional NMDARs are primarily structural determinants involved in the allosteric regulation of the open probability of the ion channel and of the agonist response by modulatory compounds (Costa et al., 2011; Zhu et al., 2013). In line with this conclusion reached for conventional GluN1/GluN2 receptors, our present and previous studies (Schuler et al., 2008; Madry et al., 2008) of the less examined glycine-gated GluN1/GluN3A receptors also demonstrate that deletion of the NTDs affect mainly receptor efficacy and not cell-surface expression. However, since interactions between the GluN3A NTDs are not required for Zn^{2+} modulation (Madry et al., 2008), differences in modulatory Zn^{2+} binding sites have to exist between conventional GluN1/GluN2 and glycine-gated GluN1/GluN3 NMDA receptors (Paoletti and Neyton, 2007). In summary, our data strengthen the view that the NTDs are not required for the formation of either glutamate- and glycine-gated NMDA receptors.

Based on the results presented here, we suggest that the major role of the GluN3-NTDs in GluN1/GluN3 NMDA receptors is to reduce the efficacy of glycine-induced channel opening. Our results clearly show that the GluN1 and the GluN3 NTDs do not equally participate in determining GluN1/GluN3A receptor efficacy; rather the GluN3A NTD constitutes the important domain (see Fig. 2). Our results are in line with studies on conventional GluN1/GluN2 NMDA receptors, where it was shown that in particular the NTDs of GluN2 subunits control subunit-specific receptor gating by undergoing large-range conformational changes, thereby dictating

Fig. 3. Effects of GluN3A NTD crosslinking and GluN3A NTD-LBD linker region mutations on the functional properties of GluN1/GluN3A receptors. (A) Lateral view of two GluN3A subunits (shown in blue and green, respectively) within the tetrameric GluN1/GluN3A receptor complex (for simplicity, only the GluN3A dimer of the tetrameric receptor is shown). The approximate positions of the GluN3A NTD-interface (red square) and NTD-LBD-linker (gray square) with the respective mutations introduced are indicated. Enlargements: Detailed views of the GluN3A NTDs with the $\alpha 5$ helix showing the intersubunit R319C disulfide bond in yellow, and of the assumed GluN3A NTD-LBD linker region with residues E498 and H509 in red. Inset, lower right: Overall view of the homology model of the GluN1/GluN3A NMDA receptor based on the crystal structure of GluN1/GluN2B receptors (Lee et al., 2014). The tetrameric GluN1/GluN3A receptor is arranged as dimer of GluN1/GluN3A-heterodimers. GluN1 and GluN3A subunits are shown in red and yellow, and blue and green, colors, respectively. Note that the model lacks the cytoplasmic residues. (B) Glycine-dose response curves of GluN1/GluN3A^{R319Cox} (■), GluN1/GluN3A^{R319Cred} (in the presence of 2 mM DTT) (◆), GluN1/GluN3A^{E498A} (●) and GluN1/GluN3A^{H509D} receptors (▲). WT dose-response curve is shown in red. (C) Maximal inducible currents induced by application of 1 mM glycine for GluN1/GluN3A^{R319C} (oxidized and reduced form), GluN1/GluN3A^{E498A} and GluN1/GluN3A^{H509D} receptors. GluN1/GluN3A^{E498A} and GluN1/GluN3A^{H509D} receptors exhibit significantly increased receptor currents as compared to the wt GluN1/GluN3A receptor. (D) Quantification of MDL-mediated potentiation of 1 mM glycine-induced currents for wt and GluN3A NTD mutant receptors. (E) MDL-induced glycine I_{\max} values of wt and mutant GluN1/GluN3A receptors. Note that in the absence of 2 mM DTT only GluN1/GluN3A^{R319Cox} receptors showed a significant change in maximal inducible current in the presence of saturating MDL and glycine concentrations ($p < 0.05$). NTD, N-terminal domain; LBD, ligand-binding domain; CD, channel domain. (For interpretation of the references to color in this figure legend, the reader is referred to the web version of this article.)

parameters such as agonist affinity, deactivation time course, channel open probability and desensitization kinetics of the receptor (Yuan et al., 2009b; Gielen et al., 2009; Madry et al., 2007b). Based on the recent X-ray crystal structure of a GluN1/GluN2 receptor complex, which revealed a unique arrangement of the GluN2 NTDs with distinct intersubunit interactions, it is assumed that the GluN2 NTDs exert their actions via affecting the GluN1/GluN2 LBD interfaces (Lee et al., 2014). However, the importance of these dimer interfaces in subunit-specific receptor regulation is still poorly understood. Based on the results presented here we suggest that i) conformational stability of the homophilic intersubunit interactions of the GluN3 NTDs is important for the auto-inhibitory effect of the GluN1 LBD, and ii) that agonist-dependent auto-inhibition of the GluN1/GluN3 receptors originates from the interaction between GluN3 NTDs rather than by interactions between GluN1/GluN3 LBDs alone.

2. Roles of the NTD-LBD linker region and the putative NTD-NTD interface in determining NMDAR efficacy

As discussed above, it is well known that the GluN2 NTDs modulate the kinetic properties of conventional NMDARs (Yuan et al., 2009b; Gielen et al., 2009; Madry et al., 2007b). Additionally, the region linking the GluN2 NTDs and LBDs has been shown to participate in the regulation of GluN1/GluN2 channel properties (Yuan et al., 2009b; Gielen et al., 2009). When swapping the NTDs, and thereby their modulatory properties, between different GluN2 subtypes, it was necessary to in addition transpose the linker regions in order to achieve a full functional switch (Yuan et al., 2009b; Gielen et al., 2009). However, the exact mechanism that couples the modulatory properties of the GluN2 NTDs and their NTD-LBD linker regions to channel activation is yet unknown. Similar to the aforementioned findings obtained for the GluN2 NTD-LBD linkers, we observed that substitutions within the GluN3A NTD-LBD linker region markedly enhance the glycine efficacy of GluN1/GluN3A receptors. Since detailed information about the structure and information of the linker of any of the iGluR members is lacking, we assume that specific side-chain interactions within the NTD-3D linker regions are important for regulatory interdomain interactions (Yuan et al., 2009b; Gielen et al., 2009; Furukawa, 2012).

Sterical restriction of the putative homophilic GluN3A NTD interface by oxidative crosslinking of GluN1/GluN3^{R319C} receptors led to a decreased glycine I_{max} . The importance of this GluN3 NTD interface in reducing receptor efficacy becomes also obvious when comparing the I_{max} values of the GluN1/GluN3A and GluN1/GluN3B receptors with that of heterotrimeric GluN1/GluN3A/GluN3B receptors, which lack a homophilic GluN3 NTD interface (Madry et al., 2010; Smothers and Woodward, 2007) and display much larger glycine-gated currents. Interestingly, co-expression of GluN3 with the classical GluN1 and GluN2 receptor subunits seems to result in reduced maximal agonist-inducible currents, suggesting that GluN3 subunits might serve as dominant-negative regulators of NMDARs (Chatterton et al., 2002; Das et al., 1998). Hence, although the role of GluN2/GluN3 NTD interactions in such tri-heteromeric NMDA receptors is still enigmatic, they are likely to play an important role in regulating the efficacy of NMDARs containing both GluN2 and GluN3 subunits. Notably, the NTD is structurally the most diverse domain in the iGluR subunits, and the tetrameric arrangement of the NTDs has been shown to differ significantly between non-NMDARs and NMDARs (Sobolevsky et al., 2009; Dutta et al., 2012; Karakas and Furukawa, 2014). Clearly further structural studies of the NTD-interfaces are required to unravel how NTD interactions determine the functional properties of NMDARs.

Since the NTDs of NMDA receptors provide binding sites for modulators and are involved in the fine-tuning of receptor gating

and pharmacological properties, cleavage of the NTDs should have significant impact on NMDA receptor function. Interestingly, proteolytic cleavage of the GluN2 NTDs of NMDA receptors by tissue-plasminogen activator (tPA) has been suggested to result in altered pharmacological properties under pathological conditions (Yuan et al., 2009a; Ng et al., 2012). Similarly, proteolytic processing of GluN3 subunits within the NTD-LBD linker region could result in profound functional alterations of GluN3-containing NMDA receptors. For the GluN1 subunit, an activity-dependent cleavage of the extracellular domain by matrix metalloproteases has been reported previously (Pauly et al., 2008).

4.3. Conclusions

The present study establishes a prominent role of the GluN3 NTDs and NTD/LBD linker regions in determining the glycine efficacy of GluN1/GluN3 NMDA receptors. In contrast to deletion of the GluN1 NTD, deletion of the GluN3A (and B) NTDs resulted in strong increases of glycine-induced maximal currents by abolishing glycine-mediated receptor auto-inhibition. Together, our results disclose differential roles of the different NMDA receptor subunit NTDs and emphasize the importance of the GluN3 NTDs in regulating GluN1/GluN3 receptor function. Drugs which target the GluN3 NTD might provide powerful tools for the selective modulation of glycine-activated NMDA receptors *in vivo*.

Conflicts of interest

The authors declare that they have no conflicts of interest with the contents of this article.

Authors contributions

IM, CM, KG and MB designed and performed experiments; IM, KG and BL analyzed data; CM, HB and BL prepared the manuscript. All authors approved the final version of the manuscript.

Acknowledgments

This study was supported by the Max-Planck Gesellschaft (H.B.), Deutsche Forschungsgemeinschaft (B.L., LA 1086/4-2) and Gemeinnützige Hertie-Stiftung (B.L.).

M.B. and B.L. acknowledge funding by the LOEWE project iNAPO of the Hessen State Ministry of Higher Education, Research and the Arts.

References

- Awobuluyi, M., Yang, J., Ye, Y., Chatterton, J.E., Godzik, A., Lipton, S.A., Zhang, D., 2007. Subunit-specific roles of glycine-binding domains in activation of NR1/NR3 N-methyl-D-aspartate receptors. *Mol. Pharmacol.* 71, 112–122.
- Bordoli, L., Kiefer, F., Arnold, K., Benkert, P., Battey, J., Schwede, T., 2009. Protein structure homology modeling using SWISS-MODEL workspace. *Nat. Protoc.* 4, 1–13.
- Borschel, W.F., Murthy, S.E., Kasperek, E.M., Popsu, G.K., 2011. NMDA receptor activation requires remodelling of intersubunit contacts within ligand-binding heterodimers. *Nat. Commun.* 2, 498.
- Chatterton, J.E., Awobuluyi, M., Premkumar, L.S., Takahashi, H., Talantova, M., Shin, Y., Cui, J., Tu, S., Sevarino, K.A., Nakanishi, N., Tong, G., Lipton, S.A., Zhang, D., 2002. Excitatory glycine receptors containing the NR3 family of NMDA receptor subunits. *Nature* 415, 793–798.
- Costa, B.M., Irvine, M.W., Fang, G., Eaves, R.J., Mayo-Martin, M.B., Laube, B., Jane, D.E., Monaghan, D.T., 2011. Structure-activity relationships for allosteric NMDA receptor inhibitors based on 2-naphthoic acid. *Neuropharm.* 62, 1730–1736.
- Das, S., Sasaki, Y.F., Rothe, T., Premkumar, L.S., Takasu, M., Crandall, J.E., Dikkes, P., Conner, D.A., Rayudu, P.V., Cheung, W., Chen, H.S., Lipton, S.A., Nakanishi, N., 1998. Increased NMDA current and spine density in mice lacking the NMDA receptor subunit NR3A. *Nature* 393, 377–381.
- Dingledine, R., Borges, K., Bowie, D., Traynelis, S.F., 1999. The glutamate receptor ion

- channels. *Pharmacol. Rev.* 51, 7–61.
- Dutta, A., Shrivastava, I.H., Sukumaran, M., Greger, I.H., Bahar, I., 2012. Comparative dynamics of NMDA- and AMPA-glutamate receptor N-terminal domains. *Structure* 20, 1838–1849.
- Farina, A.N., Blain, K.Y., Maruo, T., Kwiatkowski, W., Choe, S., Nakagawa, T., 2011. Separation of domain contacts is required for heterotetrameric assembly of functional NMDA receptors. *J. Neurosci.* 31, 3565–3579.
- Fayyazuddin, A., Villarroel, A., Le Goff, A., Lerma, J., Neyton, J., 2000. Four residues of the extracellular N-terminal domain of the NR2A subunit control high-affinity Zn²⁺ binding to NMDA receptors. *Neuron* 25, 683–694.
- Furukawa, H., 2012. Structure and function of glutamate receptor amino terminal domains. *J. Physiol.* 590, 63–72.
- Furukawa, H., Singh, S.K., Mancusso, R., Gouaux, E., 2005. Subunit arrangement and function in NMDA receptors. *Nature* 438, 185–192.
- Gielen, M., Le Goff, A., Stroebel, D., Johnson, J.W., Neyton, J., Paoletti, P., 2008. Structural rearrangements of NR1/NR2A NMDA receptors during allosteric inhibition. *Neuron* 57, 80–93.
- Gielen, M., Siegler Retchless, B., Mony, L., Johnson, J.W., Paoletti, P., 2009. Mechanism of differential control of NMDA receptor activity by NR2 subunits. *Nature* 459, 703–707.
- Guex, N., Peitsch, M.C., 1997. SWISS-MODEL and the Swiss-PdbViewer: an environment for comparative protein modeling. *Electrophoresis* 18, 2714–2723.
- Hansen, K.B., Furukawa, H., Traynelis, S.F., 2010. Control of assembly and function of glutamate receptors by the amino-terminal domain. *Mol. Pharmacol.* 78, 535–549.
- Hu, B., Zheng, F., 2005. Molecular determinants of glycine-independent desensitization of NR1/NR2A receptors. *J. Pharmacol. Exp. Ther.* 313, 563–569.
- Inanobe, A., Furukawa, H., Gouaux, E., 2005. Mechanism of partial agonist action at the NR1 subunit of NMDA receptors. *Neuron* 47, 71–84.
- Karakas, E., Furukawa, H., 2014. Crystal structure of a heterotetrameric NMDA receptor ion channel. *Science* 344, 992–997.
- Kuryatov, A., Laube, B., Betz, H., Kuhse, J., 1994. Mutational analysis of the glycine-binding site of the NMDA receptor: structural similarity with bacterial amino acid-binding proteins. *Neuron* 12, 1291–1300.
- Laube, B., Hirai, H., Sturgess, M., Betz, H., Kuhse, J., 1997. Molecular determinants of agonist discrimination by NMDA receptor subunits: analysis of the glutamate binding site on the NR2B subunit. *Neuron* 18, 493–503.
- Laube, B., Kuhse, J., Betz, H., 1998. Evidence for a tetrameric structure of recombinant NMDA receptors. *J. Neurosci.* 18, 2954–2961.
- Lee, C.-H., Lü, W., Michel, J.C., Goehring, A., Du, J., Song, X., Gouaux, E., 2014. NMDA receptor structures reveal subunit arrangement and pore architecture. *Nature* 511, 191–197.
- Lynagh, T., Kunz, A., Laube, B., 2013. Propofol modulation of $\alpha 1$ glycine receptors does not require a structural transition at adjacent subunits that is crucial to agonist-induced activation. *ACS Chem. Neurosci.* 4, 1469–1478.
- Madry, C., Betz, H., Geiger, J., Laube, B., 2010. Potentiation of Glycine-Gated NR1/NR3A NMDA receptors Relieves Ca²⁺-dependent outward rectification. *Front. Mol. Neurosci.* 3, 1–8.
- Madry, C., Betz, H., Geiger, J.R., Laube, B., 2008. Supralinear potentiation of NR1/NR3A excitatory glycine receptors by Zn²⁺ and NR1 antagonist. *Proc. Natl. Acad. Sci. U. S. A.* 105, 12563–12568.
- Madry, C., Mesić, I., Bartholomäus, I., Nicke, A., Betz, H., Laube, B., 2007a. Principal role of NR3 subunits in NR1/NR3 excitatory glycine receptor function. *Biochem. Biophys. Res. Commun.* 354, 102–108.
- Madry, C., Mesić, I., Betz, H., Laube, B., 2007b. Formation of NR1/NR2 and NR1/NR3 heterodimers constitutes the initial step in N-methyl-D-aspartate receptor assembly. *Mol. Pharmacol.* 72, 1535–1544.
- Mayer, M.L., 2006. Glutamate receptors at atomic resolution. *Nature* 440, 456–462.
- Ng, K.-S., Leung, H.-W., Wong, P., Low, C.-M., 2012. Cleavage of the NR2B subunit amino terminus of N-methyl-D-aspartate (NMDA) receptor by tissue plasminogen activator. *J. Biol. Chem.* 287, 25520–25529.
- Paoletti, P., Neyton, J., 2007. NMDA receptor subunits: function and pharmacology. *Curr. Opin. Pharmacol.* 7, 39–47.
- Papadakis, M., Hawkins, L.M., Stephenson, F.A., 2004. Appropriate NR1-NR1 disulfide-linked homodimer formation is requisite for efficient expression of functional, cell surface N-methyl-D-aspartate NR1/NR2 receptors. *J. Biol. Chem.* 279, 14703–14712.
- Pauly, T., Ratliff, M., Pietrowski, E., Neugebauer, R., Schlicksupp, A., Kuhse, J., 2008. Activity-dependent Shedding of the NMDA receptor glycine binding site by matrix metalloproteinase 3: a putative mechanism of postsynaptic plasticity. *PLoS ONE* 3, e2681.
- Qiu, S., Hua, Y.L., Yang, F., Chen, Y.Z., Luo, J.H., 2005. Subunit assembly of N-methyl-D-aspartate receptors analyzed by fluorescence resonance energy transfer. *J. Biol. Chem.* 280, 24923–24930.
- Schuler, T., Mesić, I., Madry, C., Bartholomäus, I., Laube, B., 2008. Formation of NR1/NR2 and NR1/NR3 heterodimers constitutes the initial step in N-Methyl-D-aspartate receptor assembly. *J. Biol. Chem.* 283, 37–46.
- Smothers, C.T., Woodward, J.J., 2007. Pharmacological characterization of glycine-activated currents in HEK 293 cells expressing N-methyl-D-aspartate NR1 and NR3 subunits. *J. Pharmacol. Exp. Ther.* 322, 739–748.
- Smothers, C.T., Jin, C., Woodward, J.J., 2013. Deletion of the N-terminal domain alters the ethanol inhibition of N-methyl-D-aspartate receptors in a subunit-dependent manner. *Alcohol Clin. Exp. Res.* 37, 1882–1890.
- Sobolevsky, A.I., Rosconi, M.P., Gouaux, E., 2009. X-ray structure, symmetry and mechanism of an AMPA-subtype glutamate receptor. *Nature* 462, 745–756.
- Yuan, H., Vance, K.M., Junge, C., Geballe, M., Snyder, P., Hepler, J., Yepes, M., Low, C.-M., Traynelis, S.F., 2009a. The serine protease plasmin cleaves the amino-terminal domain of the NR2A subunit to relieve zinc inhibition of the N-methyl-D-aspartate receptors. *J. Biol. Chem.* 284, 12862–12873.
- Yuan, H., Hansen, K.B., Vance, K.M., Ogden, K.K., Traynelis, S.F., 2009b. Control of NMDA receptor function by the NR2 subunit amino-terminal domain. *J. Neurosci.* 29, 12045–12058.
- Zhu, S., Stroebel, D., Yao, C.A., Taly, A., Paoletti, P., 2013. Allosteric signaling and dynamics of the clamshell-like NMDA receptor GluN1 N-terminal domain. *Nat. Struct. Mol. Biol.* 20, 477–485.

Chapter III: Gating the channel pore of ionotropic glutamate receptors with bacterial substrate binding proteins: functional coupling of the ectoine binding protein EhuB to GluR0

This chapter has been published as a preprint in:

Bernhard, Max; Laube, Bodo. *Gating the channel pore of ionotropic glutamate receptors with bacterial substrate binding proteins*. bioRxiv 2021.01.27.428399 (2021).

doi:10.1101/2021.01.27.428399

Contributions:

M.B. hat das Manuskript geschrieben. M.B. hat alle Abbildungen erstellt. M.B. hat alle Experimente und Analysen durchgeführt.

M.B. und B.L. waren an der Konzipierung der Experimente beteiligt.

B.L. betreute das Projekt und überarbeitete das Manuskript.

Gating the channel pore of ionotropic glutamate receptors with bacterial substrate binding proteins

Max Bernhard¹, Bodo Laube^{1,2}

¹Department of Biology, Neurophysiology and Neurosensory Systems, Technical University of Darmstadt, Schnittspahnstrasse 3, 64287 Darmstadt, Germany

²Centre for Synthetic Biology, Technical University of Darmstadt, 64283 Darmstadt, Germany

Corresponding author: laube@bio.tu-darmstadt.de; Tel.: +49-6151-16-20970

Author contributions: M.B. designed and performed the experiments and analyzed the data. M.B. and B.L. wrote the paper.

Competing interests: The authors declare no competing interests.

Acknowledgements: This work has been supported in the frame of the LOEWE project iNAPO by the Hessen State Ministry of Higher Education, Research and the Arts. The authors acknowledge support by the German Research Foundation and the Open Access Publishing Fund of Technische Universität Darmstadt.

Data availability: All data supporting the findings of this study are available within the article or are available from the corresponding author upon reasonable request. All cDNA constructs are available from the corresponding author based on reasonable request.

Ethical approval: All procedures involving animals were in accordance with the guidelines and regulations of the local animal care and use committee. Methods were approved by the Technical University of Darmstadt (II25.3-19c20/15, RP Darmstadt, Germany).

Abbreviations: AMPA, α -amino-3-hydroxy-5-methyl-4-isoaxazolepropionic acid; CTD; C-terminal domain; iGluR, ionotropic glutamate receptor; LBD, ligand binding domain; NTD, N-terminal domain; RMSD, root-mean-square deviation; SBD, substrate binding domain; SBP, substrate binding protein; TMD, transmembrane domain

Competing interests: The authors declare no competing financial interest.

Abstract: Tetrameric ionotropic glutamate receptors (iGluRs) mediate excitatory neurotransmission in the mammalian central nervous system and are involved in learning, memory formation, and pathological processes. Based on structural and sequence similarities of the ligand-binding and channel domains of iGluR subunits to bacterial binding proteins and potassium channels, iGluRs are thought to have originally arisen from their fusion. Here we report the functional coupling of the bacterial ectoine binding protein EhuB to the channel pore-forming transmembrane domains of the bacterial GluR0 receptor by stabilization of dimeric binding domains. Insertion of a disulfide bridge in the dimer interface abolished desensitization of the channel current analogous to mammalian iGluRs. These results demonstrate the functional compatibility of bacterial binding proteins to the gate of the channel pore of an iGluR. Moreover, our results highlight the modular structure and crucial role of binding domain dimerization in the functional evolution of iGluRs.

Introduction

Tetrameric ionotropic glutamate receptors (iGluR) mediate the majority of excitatory neurotransmission in the central nervous system by converting a chemical signal (neurotransmitter) into an electrical signal (Traynelis et al., 2010). Based on their pharmacological properties, vertebrate iGluRs can be subdivided into four subfamilies: α -amino-3-hydroxy-5-methyl-4-isoaxazolepropionic acid (AMPA), kainate (KA), N-methyl-D-aspartate (NMDA), and δ -receptors. Additional members of the iGluR family can be found among the entire animal kingdom (Ramos-Vicente et al., 2018), in plants (Lam et al., 1998) and bacteria (Chen et al., 1999). Despite their diverse physiological functions, all eukaryotic iGluRs share the same modular architecture (Fig 1a). They consist of an extracellular N-terminal domain (NTD), an extracellular ligand-binding domain (LBD), a transmembrane domain (TMD; M1, M3, M4) including the pore loop (M2) and an intracellular C-terminal domain (CTD). The LBD is a two-lobed domain composed of an extracellular region (called D1 or S1) preceding the first transmembrane domain M1 and a second extracellular region (called D2 or S2) connecting the transmembrane segments M3 and M4. Glutamate occupation of the LBDs, which are arranged as two dimers in a “back-to-back” fashion in the tetrameric receptor, induces a closure of both clamshell-like domains that is transduced towards the TMD and results in permeation of Na^+ , K^+ and Ca^{2+} - ions across the cell membrane (Armstrong et al., 2006; Dürr et al., 2014; Sobolevsky et al., 2009a). Nevertheless, the emergence of their modular architecture remains most widely unknown. The shared complex architecture of eukaryotic iGluRs suggests an ancient separation of the protein family (Lam et al., 1998; Price et al., 2012) with a common ancestor that can be traced back as far as bacteria (Chen et al., 1999; Janovjak et al., 2011). Prokaryotic iGluR subunits, such as GluR0 (Chen et al., 1999), display a simplified architecture, lacking the third transmembrane segment M4 and an NTD, while also exhibiting unique functional and pharmacological features, including a potassium selectivity filter and the ability to be activated by a broad range of amino acids. Interestingly, individual domain segments of iGluRs share structural similarities with other prokaryotic protein families. Thus, the LBD of iGluRs are structural homologue to class II bacterial solute binding proteins (SBP) (Felder et al., 1999) and the TMD displays an inverted architecture of tetrameric K^+ -channels (Doyle et al., 1998; Sobolevsky et al., 2009b), leading to the proposal that iGluRs possibly arose by the fusion of SBP and potassium channels. Recent findings

confirm the general kinship between K⁺-channels and iGluRs by coupling an iGluR LBD to a small viral K⁺-channel (Schönrock et al., 2019), highlighting a conserved activation mechanism of the channel pore in both protein families. However, the overall sequence identities between iGluRs and SBPs are low (Tikhonov and Magazanik, 2009) and the evolutionary link between SBP and iGluR remains unclear. SBP mediate the uptake of a large variety of substances across the cell membrane (Tam and Saier, 1993) and is further involved in chemotaxis and DNA regulation (Lewis et al., 1996). Despite a low sequence similarity, SBP display, like iGluR LBDs, a highly conserved three-dimensional clamshell-like structure composed of two α/β domains (D1 and D2), connected by a small hinge with one to three interconnecting strands. Based on their topological arrangements SBPs can be divided into two classes (Fukami-Kobayashi et al., 1999) or more recently in seven clusters (Berntsson et al., 2010; Scheepers et al., 2016). Ligand binding takes place between the interface of the D1 and D2 subdomains and initiates a closure in a venus fly-trap mechanism (Mao and McCammon, 1984), a key element in ligand recognition and signal transduction in all SBP associated protein families.

Although iGluR LBDs and SBPs share some similarities in their overall structure and ligand recognition the functional compatibility of SBP to gate the channel pore of an iGluR has not been investigated. Here, we coupled in a proof of principle concept the bacterial ectoine binding protein EhuB to the channel pore of GluR0, building a functional ectoine activated receptor. With this approach, we provide the first experimental evidence that iGluRs originated by the fusion of an amino acid SBP to an ion channel. Further, our results highlight a conserved ligand binding mechanism in both protein families and the role of LBD dimerization in the functional evolution of iGluR from SBPs.

Results

Identification of an iGluR LBD structure-homologous SBP

The structural and molecular requirements for SBPs to build a LBD that is functionally linked with an (iGluR) channel pore to connect ligand binding with channel opening, which may provide insights into the evolution of iGluRs, remains widely unknown. To study these requirements, we wanted to create a functional chimeric receptor by replacing the LBD of the bacterial GluR0 receptor with a structurally related class II

bacterial SBP. The bacterial GluR0 receptor was chosen due to its less complex architecture compared to eukaryotic iGluRs, characterized by the lack of an NTD, a M4 helix and an CTD, possibly displaying an evolutionary link between potassium channels, SBP and iGluRs (Chen et al., 1999). In the first step, we wanted to identify a SBP related to the GluR0 LBD. Due to the high number of SBPs and their low sequence identity, commonly below 20% (Berntsson et al., 2010), we decided to identify related bacterial SBPs based on their structural similarities using the Vast(+) algorithm (Madej et al., 2014). For protein identification, it must be considered that the extent of LBD closure must be conserved since it possibly contributes to a sufficient receptor activation (Neali Armstrong and Gouaux, 2000; Gill et al., 2008) and that additional SBDs that are part of enzyme complexes or gene regulators with different functional adaptations could be identified. Therefore, we used the structure of the glutamate-bound closed GluR0-LBD conformation (Mayer et al., 2001) (PDB ID: 1ii5) as a search template to ensure a similar extent of domain closure upon ligand binding (see Materials and Methods section). The 391 identified structures with root-mean-square deviation (RMSD) values up to 4 Å were further manually inspected to remove duplicates and open or unliganded structures, as well as structures of enzymes and gene regulators. To analyze the structural relationship and features between SBP and iGluR LBDs, the RMSD values of the 94 remaining SBPs and SBDs were further used to create a structural distance tree using the kitsch program (Fig. 1b, Supplementary Table S1). In general, the structures can be divided into 3 clusters according to Berntsson et al., 2010. The largest cluster F comprises of SBPs with two hinge segments (8-10 amino acids each) that bind a wide variety of substrates including amino acids, trigonal planar anions, compatible solutes and iron, and all iGluR LBDs. Interestingly, all iGluR LBDs form a small sub-cluster with a branching order supporting the current assumption with GluR0 representing a bacterial iGluR archetype and the freshwater bdelloid rotifer AvGluR1 (Janovjak et al., 2011) as a transitional stage between pro- and eukaryotic iGluRs. The third cluster D, which displays only SBPs, is characterized by two short hinge segments (4-5 amino acids each) and binds various substances like sugars, phosphates, iron and molybdate. Cluster E is placed between clusters D and F, exhibiting exclusively SBDs of TRAP- and TT-transporters. Interestingly, almost all SBPs that are structurally closely related to the iGluR bind amino acids or derivatives. Further analysis revealed that a common feature of this amino acid binding protein group is a

short C-terminus with a similar length as found in GluR0, relatively to position Ser366 in the GluR0 LBD (Fig 1c), compared to non-amino acid binding proteins ($p < 0.0001$, Student's two-tailed, unpaired t-test with Welch's correction). The extended C-termini of non-amino acid binding proteins often attached to the upper D1-lobe, forming the LBD interface in iGluRs. Surprisingly, the ectoine binding protein EhuB is listed as the most related non-amino acid SBP to the GluR0 LBD within cluster II. EhuB is part of ABC transporter system Ehu from *Sinorhizobium meliloti*, that mediates the uptake of the compatible solutes ectoine and hydroxyectoine with high affinity ($K_d = 1.6 \mu\text{M}$) under osmotic stress (Hanekop et al., 2007). Despite a sequence identity of only 17 %, EhuB shows an almost identical overall structure to the GluR0 LBD with a RMSD of 2.2 Å and 216 of 258 superimposed amino acids (Figure 1c). Furthermore, both binding domains share a similar rotation angle in the closed, liganded conformation. These convenient features provided for us the basis of a proof-of-concept approach to combine the ectoine binding protein EhuB (PDB ID 2Q88) with the channel pore of GluR0. Since EhuB presumably evolved in absence of any adaptive constraints to gate the pore of ion channels it substantiate the general mechanistic and evolutionary capability of SBPs to gate an ion channel by converting chemical information into an electric signal.

Replacement of the GluR0 LBD with the ectoine binding protein

To examine whether GluR0 can serve as a foundation for functionally coupling the ectoine binding protein EhuB to its channel pore, we first expressed the codon optimized GluR0 receptor containing a GluR6 signal peptide and a N-terminal c-Myc tag in *Xenopus laevis* oocytes. Injected oocytes produced glutamate dependent inward currents at -80 mV in potassium ringer solution (100 mM KCl, 1 mM CaCl₂, 5 mM HEPES, pH 7.4) with maximum peak currents of 162.5 ± 51.2 nA (mean \pm SEM; $n = 4$) and an EC₅₀ value of 29.9 ± 5 μM . After testing the applicability of GluR0 for receptor chimera design, we first asked if the fusion of the unmodified EhuB binding protein with the GluR0 TMD is sufficient to gate the channel pore. This chimeric receptor is further termed GluR0EhuB. In GluR0, the LBD is subdivided into two subdomains separated by the TMD and connected by two linkers. In the absence of a full-length GluR0 crystal structure, we estimated the connection position between the GluR0 linkers and the prospective EhuB LBD by superposition of the crystal structures of both binding domains (Fig. 2a,b). The previously described ends of the GluR0 LBD lobes (P139, A255) (Mayer et al., 2001) were set as a reference point

and EhuB was fused at position K132 and N135 with the GluR0 S1-M1 and M2-S2 linkers. To maintain the original GluR0 linker length, positions K133, G134 in EhuB were deleted in the GluR0EhuB receptor. Additionally, the construct was codon optimized and the native EhuB signal peptide was replaced by a GluR6 signal peptide, followed by a c-Myc tag (see materials and methods section). The construct was expressed in oocytes and measured in potassium ringer solution without sodium chloride (100 mM KCl, 1 mM CaCl₂, 5 mM HEPES, pH 7.4) at -80 mV. Unfortunately, we could not observe a ligand dependent current after the application of various ectoine concentrations (1 nM – 1 mM). Analyzing the total and surface expression by surface biotinylation and western blot (Fig. 2d) revealed a clear band at the calculated molecular weight of approximately 40 kDa. We therefore concluded that the GluR0EhuB chimera was expressed at the cell surface, indicating that receptor folding and assembly is not impaired.

Optimization of the ectoine binding protein as LBD

The LBDs of iGluRs exhibit extensive intermolecular interactions within the D1 lobe, responsible for LBD dimerization between two adjacent subunits (N Armstrong and Gouaux, 2000; Sobolevsky et al., 2009c; Yelshanskaya et al., 2014). After ligand binding, the dimerization interface maintaining the D1-lobes in a back-to-back dimer arrangement, allowing the D2-lobes to separate from each other. This separation is a key step to induce the transduction of the conformational change within the LBD towards the membrane pore. Therefore, the LBD interface is crucial for channel activity by converting conformational changes within the LBD to channel opening, a feature that is probably missing in the bacterial EhuB SBP in the absence of any specific evolutionary adaption. In GluR0, the dimerization interface is characterized by several hydrogen bonds and van der Waals contacts mainly formed by 9 amino acids (V113, A118, E348, N349, Q353, K354, L361, N362, Y365) (Mayer et al., 2001). Further, EhuB exhibits an extended C-terminus, compared to the GluR0 LBD, formed by three helices (10-12), interacting with the same D1 area that promotes LBD dimerization in iGluRs. We speculated that the missing LBD dimer-interface and the large C-terminus in GluR0EhuB might prevent a specific D1-D1 LBD dimerization, resulting in a non-functional receptor chimera. Therefore, we decided to design a receptor chimera containing the GluR0 LBD dimer-interface in the fused ectoine-binding domain, hereinafter termed as GluR0EhuB_{Int} (Int for interface). By structural superposition, we identified the amino acid positions in EhuB congruent with the

amino acids mediating LBD dimerization in GluR0 (Fig. 2b,c). Due to the low deviations between the α -atoms of both structures in the interface region (0.7 to 1.9 Å), we substituted the corresponding amino acids in the EhuB-binding domain (positions M108V, C113A, K235E, E238N, R241Q, D242K, A249L, K250N and E254Y according to EhuB) to reconstruct the GluR0 LBD dimerization interface. Since the C-terminal helices 10-12 in the original EhuB binding protein presumably interfere with LBD dimerization, we additionally deleted this part in the GluR0EhuB_{Int} receptor chimera. GluR0EhuB_{Int} was also well expressed and located at the cell surface, as indicated by western blot and surface biotinylation (Fig. 2d). Application of 10 μ M ectoine (Fig. 2e), which lies in the physiological recognition range of EhuB, led to a ligand dependent inward current of 347 ± 120 nA (mean \pm SEM; n = 6) in oocytes and 79.3 ± 47.1 pA (mean \pm SEM; n = 4) in HEK293 cells with a rapid inactivation. Unfortunately, receptor currents were tremendously reduced or not longer detectable after reapplying ectoine in a timespan of up to 20 min in oocytes or HEK293 cells. Our observations give evidence that the ectoine binding protein EhuB is capable to gate the channel pore of GluR0, leading to an ectoine dependent current with maximum currents comparable to GluR0. These findings imply that our chimeric receptor maintained its tetrameric assembly to form a functional ion channel that could be gated by the LBD upon ligand binding. Further, our data suggest that the formation of the inserted LBD dimerization interface is crucial to couple changes within the LBD to channel gating.

Stabilization of the ectoine binding protein dimer interface

The insertion of a dimerization interface in GluR0EhuB_{Int} was sufficient to activate the receptor in the presence of ectoine. However, the modifications within the LBD in GluR0EhuB_{Int} resulted in a receptor with an impaired reactivation. We excluded the possibility that the ligand gets entrapped inside the binding domain after binding and cannot be washed out, caused by the introduced molecular changes in the ectoine-binding domain, since we did not observe a change in the leak current after receptor activation. Although the α -backbones of the GluR0 LBD and EhuB are highly congruent, there are some minor structural differences in the exchanged amino acid positions, especially at C113A (1.9 Å), D242K (1.6 Å), A249L (1.6 Å) and E226Y (1.7 Å). It is likely that side chains of some substituted amino acids are not capable to form intermolecular interactions, weakening the dimerization interface. Therefore, we assumed that the dimerization interface gets disrupted to an extent incapable to

reorganize after the first activation that traps the receptor in a closed, non-activable state. To test this hypothesis, we decided to strengthen the LBD dimerization interface by covalently coupling the D1-D1 subdomains by introducing a disulfide bond at position P119C and L376C (called GluR0EhuB_{Int,P119C,L376C}). This position (Fig. 3a) is functionally conserved in all AMPA- and Kainate-receptors and, if substituted with Cys or Tyr, prevents receptor desensitization by stabilizing the LBD dimers (L. Chen, K. Dürr, 2014; Sun et al., 2002; Weston et al., 2006). Application of ectoine (Fig. 3b, c) in GluR0EhuB_{Int,P119C,L376C} expressing HEK293 cells induced a concentration-dependent activation with a maximum current response of 65.1 ± 10.7 pA and an EC₅₀ value of 14.1 ± 7.3 nM (mean \pm SEM, n = 4). GluR0EhuB_{Int,P119C,L376C} evoked currents resembled some characteristics of GluR0, such as slow receptor activation, a high efficient dose-dependent activation, as well as a decreased desensitization upon prolonged applications (3 s) of ectoine, which is in agreement with previous studies on other members of the iGluR family (L. Chen, K. Dürr, 2014; Sun et al., 2002; Weston et al., 2006). Thus, by stabilizing the dimerization interface, we were able to retain receptor activity over multiple ectoine reapplications. Together, our results demonstrate the functional capability of the bacterial ectoine binding protein EhuB to gate the channel pore of GluR0 by specific changes in the amino acid sequence of the EhuB-binding domain, resulting in ligand and concentration dependent receptor currents.

Discussion

Although it has long been proposed that the LBDs of iGluRs are derived from bacterial SBPs (Felder et al., 1999), the evolutionary and functional compatibility of SBPs as an ancient module for ligand recognition in iGluRs has not yet been investigated. In this study, we characterized the basic molecular requirements to functionally couple a SBP to the channel pore of an iGluR, substantiating the functional compatibility and evolutionary kinship between both protein families. Our results indicate (i) a conserved ligand binding mechanism between SBPs and iGluR LBDs, (ii) that the formation of a LBD dimerization interface is a key step in iGluR evolution to couple ligand binding to channel gating and (iii) that iGluRs probably evolved by the fusion of class F amino acid binding proteins with potassium channels.

All iGluRs consist of at least two domains: the LBD and the ion channel-forming TMD. The common molecular architecture is most likely the result of different protein precursors, which fused during the evolution of iGluRs. It has been clearly shown that potassium channels display several similarities in their overall structure, topology and sequence with the pore domains of iGluRs (Chen et al., 1999; Kuner et al., 2003; Wood et al., 1995) and share a common gating mechanism (Schönrock et al., 2019), underscoring a common origin. Felder and colleagues first proposed over 20 years ago (Felder et al., 1999) that SBPs represent a blueprint of modern iGluR LBDs by sharing a common ligand binding mechanism. However, due to their high functional diversity and low sequence identity, it is insufficient to draw conclusions about a common origin of both protein domains. By coupling the ectoine binding protein EhuB to the channel pore of GluR0 in a semi-rational approach we emphasize a common origin and ligand binding mechanism of SBPs and iGluRs. In iGluRs, ligand binding can induce either a partial closure of the clamshell shaped LBD, as found in pre-active states, or a full closure that is associated with the active state. The extent of receptor activation depends on both the capability to induce a full LBD closure and the fraction of time the LBD occupies this fully closed conformation. In contrast, incomplete domain closure results in unproductive conformations and a decreased activity, as seen for partial agonists (Ahmed et al., 2011; Lau and Roux, 2011; Maltsev et al., 2008; Salazar et al., 2017; Twomey and Sobolevsky, 2018; Zhang et al., 2008). Interestingly, even SBPs sample a wide range of conformations of partial-closed structures, that are actively involved in substrate transport, as well as non-transported ligands adopting a distinct conformation to those that are actively transported (Boer et al., 2019; Gouridis et al., 2014; Tang et al., 2007). It is therefore evident that both the GluR0 LBD and EhuB must adopt a similar fully closed conformation in the presence of the TMD, to open the GluR0 channel pore. Furthermore, the functionality of our chimeric receptors suggests that the general mechanism of ligand binding and domain closure must be similar in EhuB and GluR0, exhibiting a comparable amount of free energy to stabilize the ligand and a similar probability to occupy the fully closed conformation. These findings highlight the general modular architecture of iGluRs and support the common hypothesis that the LBD originates from a bacterial SBP. It further suggests that the underlying mechanism of full- and partial agonism, as well as competitive inhibition in iGluRs, could be traced back to its bacterial precursors.

Further, our data sheds light on the minimum molecular requirements to obtain receptor function after a potential fusion event and govern the physiological properties of modern iGluR LBDs. The formation and maintenance of the back-to-back dimer arrangement by the D1-D1 interface is crucial for iGluR gating. During activation, the interface is responsible to adhere two adjacent LBDs. This allows the D2 lobes within the LBD dimers to separate from each other to transfer the conformational change via the linkers to the ion channel (Armstrong et al., 2006; Dürr et al., 2014; Sobolevsky et al., 2009a). In contrast, the same force that creates strain on the connecting linker upon ligand binding can lead to a partial or full rupture of the dimerization interface, known as desensitization. The rupture of the LBD dimerization interface results in a reorientation of the LBD dimer, allowing the D2 lobes to adopt a closed state-like conformation that disconnects the closed LBD conformation from channel activation (Meyerson et al., 2014; Plested, 2016; Schauder et al., 2013; Sun et al., 2002). Our data suggest that the bare fusion of a SBP to an ion channel pore is insufficient to form a functional receptor. We suppose that the TMD of the GluR0EhuB receptor assembles as a tetramer, since it is displayed at the plasma membrane, forming a putative functional channel pore. Since it has not been reported that EhuB assembles as dimers or oligomers in solution (Hanekop et al., 2007) and in the absence of any evolutionary pressure, it is unlikely that functional interactions are formed within the LBD layer of the GluR0EhuB receptor, holding the dimers in a fixed position during receptor gating. Therefore, we assume that ligand binding to the EhuB binding domain is decoupled from channel gating, since the force generated by clamshell closure cannot be used to separate the D2 lobes and transferred by the linkers. This is consistent with previous studies, showing that a complete rupture of the D1 dimerization interface by covalently connecting the D2 lobes, leads to a decoupling of agonist binding from ion channel gating (Armstrong et al., 2006). Remarkably, the change of a few amino acids within the putative LBD dimerization interface is sufficient to gain basic receptor activity, as seen in GluR0EhuB_{Int}. However, the GluR0 LBD and EhuB protein are not completely homologues in their spatial structure. It is most likely that the inserted artificial dimerization interface is too weak to prevent a full rupture of the interface upon ligand binding that locks the receptor in a non-active conformation where ligand binding is disengaged from channel gating. This is in agreement that even minor perturbations of the dimerization interface by single point mutations enhance desensitization and

can lead to a delayed receptor recovery (Fleck et al., 2003; Horning and Mayer, 2004; Partin et al., 1996; Sun et al., 2002). By covalently stabilizing the LBD dimerization interface in GluR0EhuB_{Int,P119C,L376C}, we demonstrated that the impaired activation mechanism can be overcome and resulted in a receptor chimera that is capable to undergo a full gating cycle from activation to deactivation and recovery. Moreover, the activation and deactivation kinetics observed in GluR0EhuB_{Int,P119C,L376C} resemble the slow activation of GluR0 and the constitutive activity upon a prolonged ligand application observed in LBD stabilized AMPA- and kainite receptors. In conclusion, these findings reveal the dimerization interface as the key element in the molecular evolution of iGluRs that is crucial to couple the clamshell closure of the binding domain to ion channel gating. The requirement of only minor adaptations to form a LBD dimerization interface to obtain a functional iGluR archetype is presumably an advantage in the functional evolution and physiological adaptation of iGluRs to fulfill different tasks among bacteria, plants, amoebas and metazoans.

The structural distance tree only provides limited information about the direct phylogenetic relationship of proteins, since it is only based on structural derivations and not on sequence comparisons. However, structural derivations are a result of changes in their protein sequence. We therefore can make some assumptions about the evolutionary origin of iGluR LBDs. It should be emphasized that the closest structural related SBPs in cluster F all bind amino acids or amino acid derivatives. This finding is less surprising since GluR0 as well as AvGluR1, two putative links between the evolution of modern metazoan iGluRs from SBPs and potassium channels, are activated by several polar amino acids (Chen et al., 1999; Janovjak et al., 2011). Furthermore, the LBD of AMPA receptors and GluR0 share a weak amino acid sequence homology with the glutamine binding protein from *Escherichia coli* (Chen et al., 1999). For that reason, it is most likely that the ancient SBP precursor belongs to class F SBPs. It is notable that all identified class F amino acid and amino acid derivative SBPs display a relatively short C-terminus compared to all non-amino acid binding proteins found in the more distant classes D and E. These extended C-termini often pack to the D1 lobe, masking the same helices that mediate LBD dimerization in iGluRs. Presumably, it was advantageous in the evolution of iGluRs, that the putative LBD dimer interface was freely accessible in amino acid binding proteins that facilitated a rapid functional adaptation of dimer-dimer interactions without

extensive changes in the protein structure. Moreover, the short C-termini of amino acid binding proteins possibly served as a putative S2-M4 linker to couple the additional M4 helix in later evolutionary iGluR stages.

In summary, by functionally coupling the ectoine binding protein EhuB to the GluR0 channel pore we substantiate the compatibility between both protein families and shedding light on the functional and molecular evolution of iGluRs from bacterial SBPs and potassium channels. Our results may help in the mechanistic understanding of ligand recognition in both protein families and drug design. Finally, our approach, combined with the diversity of recognized ligands and the structural adaptability of SBPs could be used as a versatile tool in the design of biosensor with a high specificity and efficiency.

Materials and Methods

Identification of homologous SBP and structural distance tree

For structure identification and building a structural distance tree, we used the previously described method from Scheepers et al., 2016 with some modifications. To identify SBPs that are structurally homologous to the LBD of GluR0, we used the ligand-bound LBD conformation (1ii5) as a search template against the Molecular Modeling Database (MMDB) using the Vector Alignment Search Tool (VAST+) (Madej et al., 2014). The resulting 354 PDB codes were matched against the UniProt IDs to filter out multiple structures of the same protein. Additionally, unliganded structures, enzymes and gene regulators were filtered out by manual inspection. This search resulted in about 94 SBP- and iGluR LBD-structures similar to the GluR0 LBD (Supplementary Table S1). The remaining structures were pairwise aligned using the PDBeFold server (Krissinel and Henrick, 2004). To build the structural distance tree, the RMSD values obtained from PDBeFold were loaded into the KITSCH program of the PHYLIPS package with default parameters (Felsenstein, 2004). Protein clusters were verified by visual inspection using UCSF Chimera (Pettersen et al., 2004) according to Berntsson et al., 2010 and the structural distance tree was visualized using iTOL (<https://itol.embl.de/>). For the determining the C-termini lengths of amino acid and non-amino acid SBP, structures were pairwise aligned to the GluR0 LBD (1ii5) and inspected using UCSF Chimera. The relative C-terminus was specified relative to position Ser366 in the GluR0 LBD. Statistical significance was determined at the $p \leq 0.05$ (*), $p \leq 0.01$ (**), $p \leq 0.001$ (***) and $p \leq 0.01$ (****), levels using a Student's two-tailed, unpaired t-test with Welch's correction. Equality of variances was tested using a F-test.

Protein engineering

In this study, we used the sequences from GluR0 (UniProt ID P73797) and EhuB (UniProt ID Q92WC8). Signal peptide cleavage site was predicted using SignalP v. 4.1 (Nielsen et al., 1997). The intrinsic GluR0 (residues 1-19) or EhuB signal peptides (residues 1 – 27) were replaced by the GluR6 signal peptide (MRILCRQIVLLFSGFWGLAMG), followed by a c-myc tag (EQKLISEED) and a short linker (SGTPT). For GluR0EhuB, EhuB D1 domain (residues 28 – 132) was fused to the N-terminal and the D2 domain (residues 135 – 283) to the C-terminal end of the GluR0 TMD, including the linker (residues 139 – 255). For GluR0EhuB_{Int}, the

positions M81V, C86A, K208E, E211N, R214Q, D215K, A222L, K223N and E226Y were substituted and residues 266 – 283 were deleted (positions corresponding to the original EhuB protein). For receptor expression in eukaryotic expression systems, the sequences of all constructs were codon-optimized for *Xenopus laevis*. GluR0, GluR0EhuB and GluR0EhuB_{Int} DNA strings were synthesized (GeneArt, Thermo Fisher Scientific, Regensburg, Germany) and subsequently cloned into the vector pCDNA3.1(+) via included *NheI* and *XhoI* restriction sites. For GluR0EhuB_{Int,P119C,L376C}, the primers P119C forward (ATTGTTTGTCAAGTGTGAGAGAGCCGCT) and reverse (AGCGGCTCTCTCACACTTGAC AAACAAT), as well as L376C forward (TGATGTTGAACTCTGTAATCTGAAATACTCCG) and reverse (CGGAGTATTTTCAGATTACAGAGTTCAACATCA) were used for mutagenesis polymerase chain reaction (PCR). PCR reaction parameters were as follows: initial denaturation at 95 °C for 60 s; 30 cycles at 95 °C and 30 s, 56 °C for 15 s and 72 °C for 150 s; and one cycle at 72 °C for 180 s. All constructs were confirmed by sequencing (Seqlab, Göttingen, Germany).

Sequences

GluR0EhuB:

MRIICRQIVLLFSGFWGLAMGEQKLISEEDLSGTPTDENKLEELKEQGFARIAIANEP
PFTAVGADGKVS GAAPDVAREIFKRLGVADVVASISEYGAMIPGLQAGRHDITAGL
FMKPERCAAVAYSQPILCDAEAFALKGKPVSLWERFSPFFGIAALSSAGVLTLLLFLV
GNLIWLAEHRKNPEQFSPHYPEGVQNGMWFALVTLTTVGYGDRSPRTKLGQLVAG
VWMLVALLSFSSITAGLASAFSTALSEASNPLGLKSYKDIADNPDAKIGAPGGGTEE
KLALEAGVPRDRVIVPDGQSGLKMLQDGRIDVYSLPVLSINDLVSKANDPNVEVLA
PVEGAPVYCDGA AFRKGDEALRDAFDVELAKLKESGEFAKIIIEPYGFSAKAAMSTTR
EKLCAAK

GluR0EhuB_{Int}

MRIICRQIVLLFSGFWGLAMGEQKLISEEDLSGTPTDENKLEELKEQGFARIAIANEP
PFTAVGADGKVS GAAPDVAREIFKRLGVADVVASISEYGAMIPGLQAGRHDITAGL
FVKPERAAAVAYSQPILCDAEAFALKGKPVSLWERFSPFFGIAALSSAGVLTLLLFLV
GNLIWLAEHRKNPEQFSPHYPEGVQNGMWFALVTLTTVGYGDRSPRTKLGQLVAG
VWMLVALLSFSSITAGLASAFSTALSEASNPLGLKSYKDIADNPDAKIGAPGGGTEE

KLALEAGVPRDRVIVVPDQSGSLKMLQDGRIDVYSLPVLVLSINDLVSKANDPNVEVLA
PVEGAPVYCDGAAFREGDNALQKAFDVELLNLKYSGEFAKIIIEPYG

Heterologous expression in X. laevis oocytes

Constructs were expressed in *X. laevis* oocytes as described previously (Schönrock et al., 2019). In brief, all constructs in pCDNA3.1(+) were linearized with NotI and cRNA was synthesized using the AmpliCap-Max™ T7 High Yield Message Maker Kit (Cellscript, Madison, WI, USA). Surgically obtained oocytes from female *X. laevis* were enzymatically separated and defolliculated using 0.8 mg collagenase in ringer solution (96mM NaCl, 2 mM KCl, 1mM CaCl₂, 1mM MgCl₂, 5mM HEPES; pH 7.4) for 12 h and reaction was stopped with Ca²⁺-free ringer solution. 50 ng of capped and polyadenylated RNA with 50 nl water was microinjected in defolliculated stage IV – V oocytes and incubated 3 – 7 days in ND-96 solution (96 mM NaCl, 2 mM KCl, 1 mM MgCl₂, 5 mM HEPES, 50-mg ml⁻¹ gentamycin; pH 7.5) at 18 °C. Related oocyte experiments (for example total and surface expression) were performed with the same oocyte batches on the same day.

Heterologous expression in HEK293 cells

HEK293 cells were cultured in minimum essential medium (MEM) supplemented with 10 % (v/v) FCS, 2 mM L-glutamine and streptomycin (100 µg/ml). Before transfection, 5x10⁵ cells were reseeded into T25 flask and transfected using TurboFect (Thermo Fisher Scientific, Waltham, MA, USA) and 4 µg plasmid DNA per flask of the respective construct in pCDNA3.1(+) and pEGFP-N1 as a transfection control with a ratio of 4:1. After transfection, cells were incubated for 48-72 h at 37 °C and 5% CO₂.

Surface biotinylation

For surface biotinylation, 20 oocytes per construct were injected as described above and incubated for 3 days in ND-96 solution at 18 °C. Oocytes were washed three times with PBS (100 mM phosphate buffer, 150 mM NaCl; pH 7.2) and surface proteins were biotinylated using 0.5 mg/ml Sulfo-NHS-SS-Biotin (Thermo Fisher Scientific) in PBS for 40 min at room temperature. Reaction was stopped with 50 mM Tris/HCl; pH 8.0. Oocytes were mechanically homogenized and membrane proteins were extracted using DDM (100 mM phosphate buffer, 150 mM NaCl 0.5 % n-dodecyl-β-D-maltoside, SIGMAFAST Protease Inhibitor Cocktail (Sigma-Aldrich, St. Louis, MO, USA); pH 8.0) for 15 min at 4°C. Biotinylated membrane proteins were

purified using Streptavidin High Performance Spintrap columns (GE Healthcare, Chicago, IL, USA).

Western blotting

For total protein expression, 10 oocytes per construct were injected and incubated for 3 days. Oocytes were washed with 0.1 M sodium phosphate buffer, pH 8.0 and mechanically homogenized. Membrane proteins were solubilized with 25 μ l lysis buffer (0.1 M sodium phosphate buffer pH 8.0, 0.5 % DDM, 0.01% pefa block) for 10 min at 4 °C and subsequently centrifuged with 1000 x g at 4°C. HEK293 cells were transfected by electroporation as described above and incubated 48 h. Cells were scraped, lysed with 200 μ l lysis buffer and subsequently centrifuged 20 min with 16000 xg at 4°C. For SDS-PAGE and western blot, total and surface labeled proteins were separated using a 10% sodium dodecyl sulfate polyacrylamide gel electrophoresis (SDS-PAGE) and transferred to a PVDF membrane (Bio-Rad, Feldkirchen, Germany). The membrane was blocked for 1 h in PBS-T supplemented with 5% skim milk and afterward incubated with 1:600 primary c-Myc-tag Polyclonal antibody (sc-789, Santa Cruz Biotechnology, Dallas, TX, USA) in PBS-T containing 1% skim milk over night at 4 °C. After washing with PBS-T, the secondary goat anti-rabbit IgG-HRP (1:10000) (sc-2054, Santa Cruz Biotechnology) was incubated in TBS-T containing 1% skim milk for 1 h at room temperature. The membrane was washed three times in TBS-T and the signal was visualized using Pierce Western Blotting Substrate (Thermo Fisher Scientific) and detected with a CCD camera.

Electrophysiological recordings of X. laevis oocytes using two-electrode voltage clamp

3-7 days after injection, whole-cell currents were recorded by two-electrode voltage-clamp at -80 mV using microelectrodes filled with 3M KCl (resistance 0.8–2.5 M Ω). Data were sampled at 5 kHz after low-pass filtering at 200 Hz using an Axoclamp 900A amplifier connected to a Digidata 1550A digitizer and recorded with Clampex 10.7 (Molecular Devices, San Jose, USA). Oocytes were placed in a perfusion chamber and rinsed with high potassium Ringer's solution (100 mM KCl, 1 mM CaCl₂, 5 mM HEPES, pH 7.4 with KOH). Ectoine (10 μ M to 0.1 nM) or L-glutamate (1 mM to 1 μ M) was applied to the oocytes in external solution. For dose-response analysis, normalized current responses were plotted against the agonist concentration and fitted with a sigmoidal Hill equation

$I/I_{max} = 100 \times x^h / (x^h + EC_{50}^h)$ in GraphPad Prism 9 (GraphPad Software Inc., La Jolla, USA) where I/I_{max} is the normalized current, x the concentration, h the Hill coefficient and EC_{50} the agonist concentration resulting in a half-maximal response. Data and graphs presented in mean \pm SEM.

Electrophysiological recordings using Port-a-patch

Electrophysiological recordings in HEK293 cells were performed using the Port-a-Patch system (Nanion Technologies, München, Germany). Adherent HEK293 cells were harvested 48-72 h after transfection using 1% accutase solution. The reaction was stopped with MEM and the cell suspension was centrifuged at 100 xg for 3 min. Cells were resuspended in extracellular solution (140 mM KCl, 1 mM MgCl₂, 2 mM CaCl₂, 5 mM D-glucose, 10 mM HEPES; pH 7.4; osmolarity 298 mOsmol) with a final concentration of 2×10^6 - 3×10^6 cells/ml. Measurements were performed using a Port-a-Patch system with external perfusion system (Nanion Technologies) and NPC-1 chips (3-5 M Ω) according to the manufacturers instructions, connected to an EPC10 amplifier (HEKA, Ludwigshafen, Germany), PatchControl (Nanion Technologies) and Patchmaster software (HEKA). External solution and internal solution (50 mM KCl, 10 mM NaCl, 60 mM KF, 20 mM EGTA, 1 mM ATP, 10 mM HEPES; pH 7.2; osmolarity 285 mOsmol) were used for experiments and seal enhancer (80 mM NaCl, 3 mM KCl, 10 mM MgCl₂, 35 mM CaCl₂, 10 mM HEPES; pH 7.4; osmolarity 298 mOsmol) was used for sealing cells. For recording receptor currents, cells were clamped at -60 mV and continuously perfused with external solution during recording. Ectoine dilution series (10 μ M – 0.1 nM) was dissolved in external solution. Agonist was applied for 3 s, followed by 10 s of wash. Dose-response analysis was performed as described above. Data and graphs presented in mean \pm SEM.

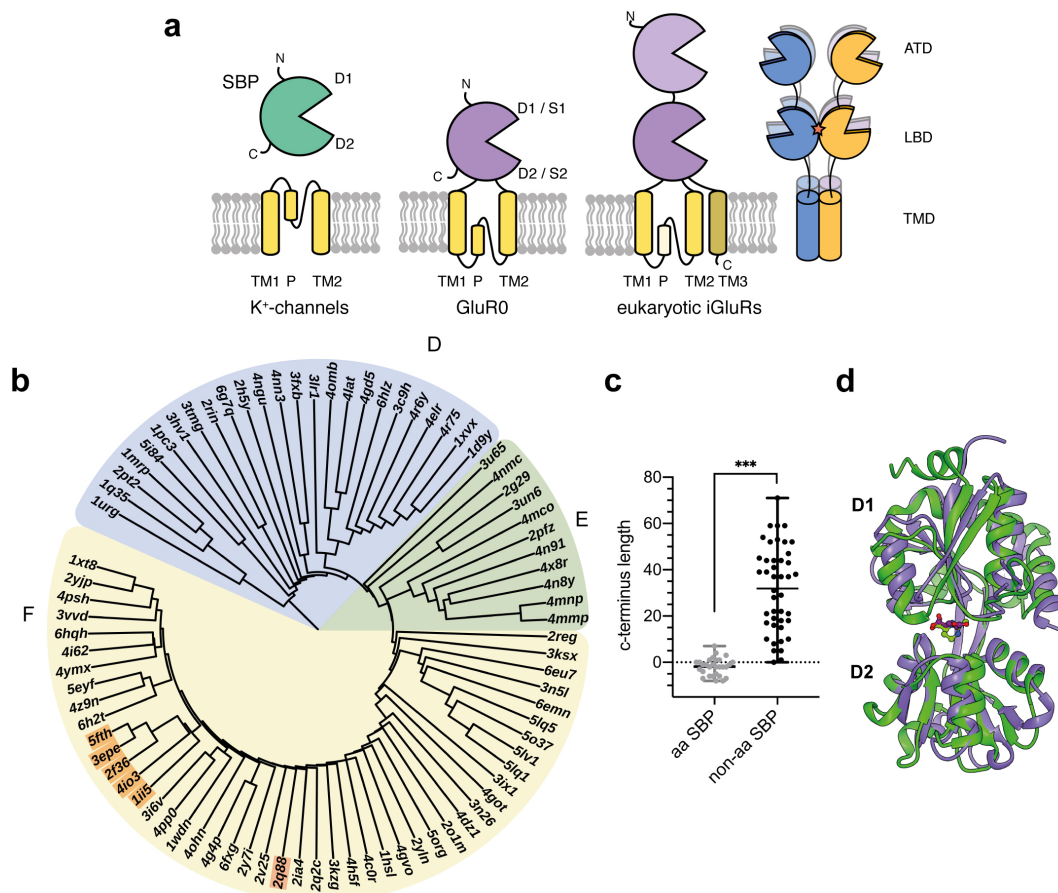


Figure 1: Structural relationship between iGluRs and SBP. **a** Modular organization of SBP, K⁺-channels and prokaryotic and eukaryotic iGluR (left) and tetrameric organization of metazoan iGluRs (right) including the amino-terminal domain (ATD), the ligand binding domain (LBD) with the dimerization interface (red star) and the transmembrane domain (TMD). **b** Structural distance tree of iGluR LBDs and SBPs structural homologous to the GluR0 LBD (1ii5). Clusters were categorized following the nomenclature of Bertsson et al. (Bertsson et al., 2010). The structural distance tree is subdivided into the following clusters: cluster F: two hinged SBPs including all iGluR LBDs (orange; GluR0:1ii5, AvGluR1:4io3, GluR5:2f36, GluR4:3epe, GluR2:5fth) and the ectoine binding protein EhuB (2q88), cluster E: SBDs from TRAP-transporters cluster D: short hinged SBPs. **c** Comparison of the C-terminus lengths between amino acid (aa) or aa derivate SBPs and non-amino acid SBPs relatively measured to position Ser366 in the GluR0 LBD ($p < 0.0001$, Student's two-tailed, unpaired t-test with Welch's correction). **d** Structural superposition between the ligand-bound, closed conformations of the GluR0 LBD (purple, 1ii5) and the ectoine binding protein EhuB (green, 2q88).

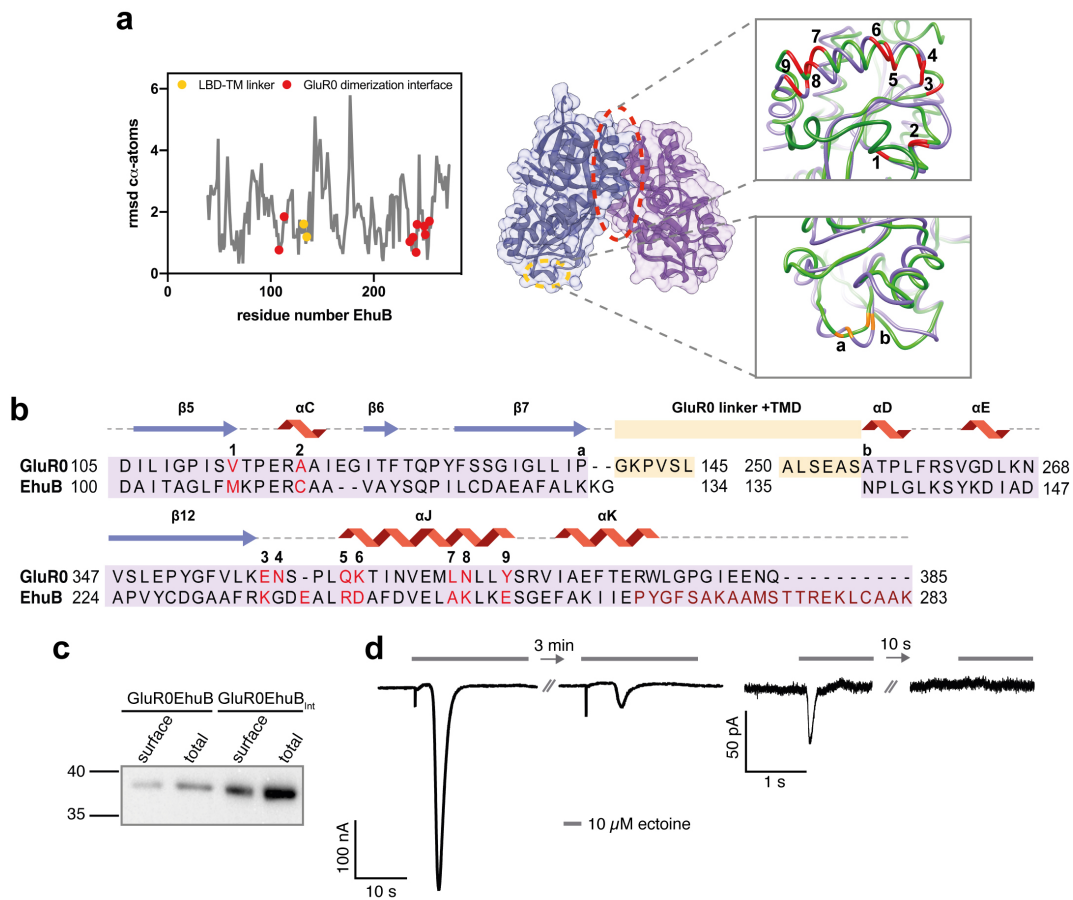


Figure 2: Design and expression of the chimeric GluR0EhuB and GluR0EhuB_{int} receptors. **a** Local RMSD of α -atoms between the GluR0 LBD and EhuB (left) and structural overview (right) of the exchanged amino acid positions within the EhuB LBD in GluR0EhuB and GluR0EhuB_{int}. The connection points to the LBD-TMD linkers (orange) and amino acid positions that are responsible for LBD dimerization in GluR0 and are exchanged in GluR0EhuB_{int} (red) are highlighted. **b** Structural sequence alignment of EhuB and the GluR0 LBD, including the linker positions (orange a,b), the substituted amino acid positions of the dimerization interface (red 1-9) and the deleted helices 10-12 (dark red) in GluR0EhuB_{int}. **c** Western blot of total and surface expression of GluR0EhuB (left) and GluR0EhuB_{int} (right) with a calculated molecular weight of 40 kDa and 38 kDa, respectively. Proteins were detected using a c-Myc tag located at the N-terminus after the signal peptide. **d** Representative traces of whole-cell currents of GluR0EhuB_{int} in *Xenopus* oocytes (left) and HEK293 cells (right) in response to 10 μ M ectoine. Arrow is indicating the reduced receptor response to a second application of ectoine after 3 min or 10 s wash out.

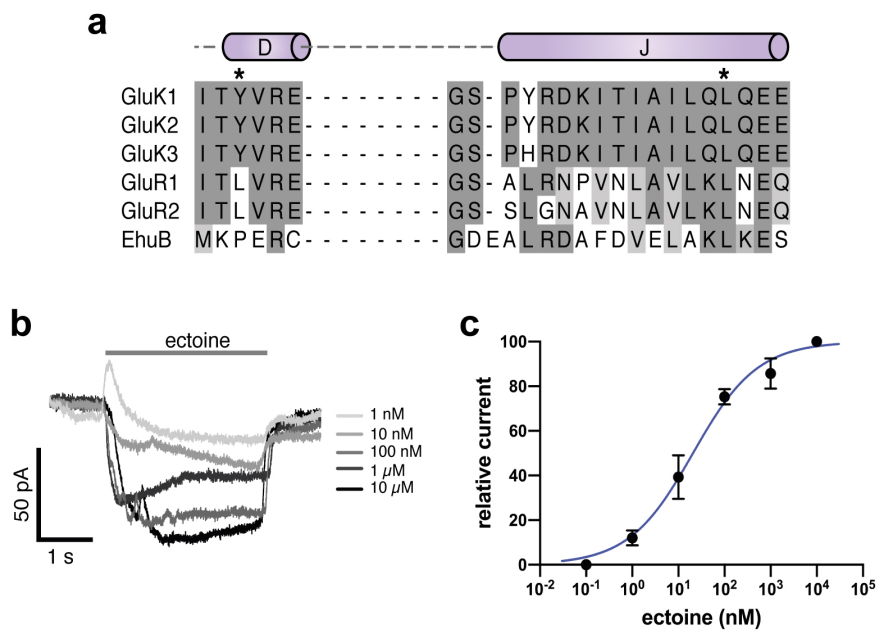


Figure 3: Stabilization of the LBD dimerization interface in GluR0EhuB_{Int,P119C,L376C} by disulfide bonds. **a** Sequence alignment of helices D and J of AMPA- and Kainate receptors that are involved in LBD dimerization interface formation. Previously published amino acid positions substituted with Cys or Tyr to covalently couple the D1 domain of each LBD-dimer in AMPA- and kainate receptors are highlighted with asterisks. **b** GluR0EhuB_{Int,P119C,L376C} responses to 3 s applications of 1 nM to 10 μM ectoine recorded from a single HEK293 cell. **c** Dose-response analysis of GluR0EhuB_{Int,P119C,L376C} revealed an EC₅₀ value of 14.1 ± 7.3 nM (mean ± SEM, n = 4).

- Ahmed AH, Wang S, Chuang HH, Oswald RE. 2011. Mechanism of AMPA receptor activation by partial agonists: disulfide trapping of closed lobe conformations. *J Biol Chem* **286**:35257–35266. doi:10.1074/jbc.M111.269001
- Armstrong Neali, Gouaux E. 2000. Mechanisms for Activation and Antagonism of an AMPA-Sensitive Glutamate Receptor. *Neuron* **28**:165–181. doi:10.1016/S0896-6273(00)00094-5
- Armstrong N, Gouaux E. 2000. Mechanisms for activation and antagonism of an AMPA-sensitive glutamate receptor: crystal structures of the GluR2 ligand binding core. *Neuron* **28**:165–181. doi:10.1016/S0896-6273(00)00094-5
- Armstrong N, Jasti J, Beich-Frandsen M, Gouaux E. 2006. Measurement of Conformational Changes accompanying Desensitization in an Ionotropic Glutamate Receptor. *Cell* **127**:85–97. doi:10.1016/j.cell.2006.08.037
- Berntsson RP a, Smits SHJ, Schmitt L, Slotboom DJ, Poolman B. 2010. A structural classification of substrate-binding proteins. *FEBS Lett* **584**:2606–2617. doi:10.1016/j.febslet.2010.04.043
- Boer M De, Gouridis G, Vietrov R, Begg SL, Schuurman-wolters GK, Husada F, Eleftheriadis N, Poolman B, Mcdevitt CA, Cordes T. 2019. Conformational and dynamic plasticity in substrate-binding proteins underlies selective transport in ABC importers. *Elife* **8**:1–28. doi:10.7554/eLife.44652
- Chen GQ, Cui C, Mayer ML, Gouaux E. 1999. Functional characterization of a potassium-selective prokaryotic glutamate receptor. *Nature* **402**:817–821. doi:10.1038/45568
- Doyle D a, Morais Cabral J, Pfuetzner R a, Kuo a, Gulbis JM, Cohen SL, Chait BT, MacKinnon R. 1998. The structure of the potassium channel: molecular basis of K⁺ conduction and selectivity. *Science* **280**:69–77. doi:10.1126/science.280.5360.69
- Dürr K, Chen L, Stein R, DeZorzi R, Folea IM, Walz T, Mchaourab H, Gouaux E. 2014. Structure and Dynamics of AMPA Receptor GluA2 in Resting, Pre-Open, and Desensitized States. *Cell* **158**:778–792. doi:10.1016/j.cell.2014.07.023
- Felder CB, Graul RC, Lee a Y, Merkle HP, Sadee W. 1999. The Venus flytrap of periplasmic binding proteins: an ancient protein module present in multiple drug receptors. *AAPS PharmSci* **1**:7–26. doi:10.1208/ps010202
- Felsenstein J. 2004. PHYLIP (Phylogeny Inference Package) version 3.6. Distributed by the author. <http://www.Evol.gs.washington.edu/phylip.html>.
- Fleck MW, Cornell E, Mah SJ. 2003. Amino-acid residues involved in glutamate receptor 6 kainate receptor gating and desensitization. *J Neurosci* **23**:1219–1227. doi:10.1523/jneurosci.23-04-01219.2003
- Fukami-Kobayashi K, Tateno Y, Nishikawa K. 1999. Domain dislocation: a change of core structure in periplasmic binding proteins in their evolutionary history. *J Mol Biol* **286**:279–290. doi:10.1006/jmbi.1998.2454
- Gill A, Birdsey-benson A, Jones BL, Henderson LP, Madden DR. 2008. Correlating AMPA Receptor Activation and Cleft Closure across Subunits : Crystal Structures of the GluR4 Ligand-Binding Domain in Complex with Full and Partial **47**:13831–13841. doi:10.1021/bi8013196
- Gouridis G, Schuurman-wolters GK, Ploetz E, Husada F, Vietrov R, Boer M De, Cordes T, Poolman B. 2014. Conformational dynamics in substrate-binding domains influences transport in the ABC importer GlnPQ. *Nat Publ Gr* **22**:57–64. doi:10.1038/nsmb.2929
- Hanekop N, Höing M, Sohn-Bösser L, Jebbar M, Schmitt L, Bremer E. 2007. Crystal Structure of the Ligand-Binding Protein EhuB from Sinorhizobium meliloti Reveals Substrate Recognition of the Compatible Solutes Ectoine and Hydroxyectoine. *J Mol Biol*

- 374**:1237–1250. doi:10.1016/j.jmb.2007.09.071
- Horning MS, Mayer ML. 2004. Regulation of AMPA Receptor Gating by Ligand Binding Core Dimers. *Neuron* **41**:379–388. doi:10.1016/S0896-6273(04)00018-2
- Janovjak H, Sandoz G, Isacoff EY. 2011. A modern ionotropic glutamate receptor with a K(+) selectivity signature sequence. *Nat Commun* **2**:232. doi:10.1038/ncomms1231
- Krissinel E, Henrick K. 2004. Secondary-structure matching (SSM), a new tool for fast protein structure alignment in three dimensions. *Acta Crystallogr Sect D Biol Crystallogr* **60**:2256–2268. doi:10.1107/S0907444904026460
- Kuner T, Seeburg PH, Guy HR. 2003. A common architecture for K+ channels and ionotropic glutamate receptors? *Trends Neurosci* **26**:27–32. doi:10.1016/S0166-2236(02)00010-3
- L. Chen, K. Dürr EG. 2014. X-ray structures of AMPA receptor–cone snail toxin complexes illuminate activation mechanism. *Science (80-)* **345**:1021–1026. doi:10.1126/science.1258409
- Lam HM, Chiu J, Hsieh MH, Meisel L, Oliveira IC, Shin M, Coruzzi G. 1998. Glutamate-receptor genes in plants. *Nature* **396**:125–126. doi:10.1038/24066
- Lau AY, Roux B. 2011. The hidden energetics of ligand binding and activation in a glutamate receptor. *Nat Struct Mol Biol* **18**:283–287. doi:10.1038/nsmb.2010
- Lewis M, Chang G, Horton NC, Kercher M a, Pace HC, Schumacher M a, Brennan RG, Lu P. 1996. Crystal structure of the lactose operon repressor and its complexes with DNA and inducer. *Science (80-)* **271**:1247–1254. doi:10.1126/science.271.5253.1247
- Madej T, Lanczycki CJ, Zhang D, Thiessen P a., Geer RC, Marchler-Bauer A, Bryant SH. 2014. MMDB and VAST+: Tracking structural similarities between macromolecular complexes. *Nucleic Acids Res* **42**:297–303. doi:10.1093/nar/gkt1208
- Maltsev AS, Ahmed AH, Fenwick MK, Jane DE, Oswald RE. 2008. Mechanism of Partial Agonism at the GluR2 AMPA Receptor : Measurements of Lobe Orientation in Solution. *Biochemistry* **47**:10600–10610. doi:10.1021/bi800843c
- Mao B, Mccammon A. 1984. Structural Study of Hinge Bending in L-Arabinose-binding Protein. *J Biol Chem* **259**:4964–4970.
- Mayer ML, Olson R, Gouaux E. 2001. Mechanisms for ligand binding to GluR0 ion channels: crystal structures of the glutamate and serine complexes and a closed apo state. *J Mol Biol* **311**:815–836. doi:10.1006/jmbi.2001.4884
- Meyerson JR, Kumar J, Chittori S, Rao P, Pierson J, Bartesaghi A, Mayer ML, Subramaniam S. 2014. Structural mechanism of glutamate receptor activation and desensitization. *Nature* **57**:328–334. doi:10.1038/nature13603
- Nielsen H, Engelbrecht J, Brunak S, von Heijne G. 1997. Identification of prokaryotic and eukaryotic signal peptides and prediction of their cleavage sites. *Protein Eng* **10**:1–6. doi:10.1142/S0129065797000537
- Partin KM, Fleck MW, Mayer ML. 1996. AMPA receptor flip/flop mutants affecting deactivation, desensitization, and modulation by cyclothiazide, aniracetam, and thiocyanate. *J Neurosci* **16**:6634–6647. doi:10.1523/jneurosci.16-21-06634.1996
- Pettersen EF, Goddard TD, Huang CC, Couch GS, Greenblatt DM, Meng EC, Ferrin TE. 2004. UCSF Chimera - A visualization system for exploratory research and analysis. *J Comput Chem* **25**:1605–1612. doi:10.1002/jcc.20084
- Plested AJR. 2016. Structural mechanisms of activation and desensitization in neurotransmitter-gated ion channels. *Nat Struct Mol Biol* **23**:494–502. doi:10.1038/nsmb.3214
- Price MB, Jelesko J, Okumoto S. 2012. Glutamate Receptor Homologs in Plants: Functions and Evolutionary Origins. *Front Plant Sci* **3**:1–10. doi:10.3389/fpls.2012.00235

- Ramos-Vicente D, Ji J, Gratacòs-Batlle E, Gou G, Reig-Viader R, Luís J, Demian B, Navas-Perez E, García-Fernández J, Fuentes-Prior P, Escriva H, Roher N, Soto D, Bayés Á. 2018. Metazoan evolution of glutamate receptors reveals unreported phylogenetic groups and divergent lineage-specific events. *Elife* **7**:1–36. doi:10.7554/eLife.35774
- Salazar H, Eibl C, Chebli M, Plested A. 2017. Mechanism of partial agonism in AMPA-type glutamate receptors. *Nat Commun* **8**:1–11. doi:10.1038/ncomms14327
- Schauder DM, Kuybeda O, Zhang J, Klymko K, Bartsaghi A, Borgnia MJ, Mayer ML, Subramaniam S. 2013. Glutamate receptor desensitization is mediated by changes in quaternary structure of the ligand binding domain. *Proc Natl Acad Sci U S A* **110**:5921–6. doi:10.1073/pnas.1217549110
- Scheepers GH, Lycklama a Nijeholt JA, Poolman B. 2016. An updated structural classification of substrate-binding proteins. *FEBS Lett* **590**:4393–4401. doi:10.1002/1873-3468.12445
- Schönrock M, Thiel G, Laube B. 2019. Coupling of a viral K⁺-channel with a glutamate-binding-domain highlights the modular design of ionotropic glutamate-receptors. *Commun Biol* **2**. doi:10.1038/s42003-019-0320-y
- Sobolevsky AI, Rosconi MP, Gouaux E. 2009a. X-ray structure, symmetry and mechanism of an AMPA-subtype glutamate receptor. *Nature* **462**:745–756. doi:10.1038/nature08624
- Sobolevsky AI, Rosconi MP, Gouaux E. 2009b. X-ray structure, symmetry and mechanism of an AMPA-subtype glutamate receptor. *Nature* **462**:745–756. doi:10.1038/nature08624
- Sobolevsky AI, Rosconi MP, Gouaux E. 2009c. X-ray structure , symmetry and mechanism of an AMPA-subtype glutamate receptor. *Nature* **462**. doi:10.1038/nature08624
- Sun Y, Olson R, Horning M, Armstrong N, Mayer M, Gouaux E. 2002. Mechanism of glutamate receptor desensitization. *Nature* **417**:245–253. doi:10.1038/417245a
- Tam R, Saier MH. 1993. Structural , Functional , and Evolutionary Relationships among Extracellular Solute-Binding Receptors of Bacteria. *Microbiol Rev* **57**:320–346.
- Tang C, Schwieters CD, Clore GM. 2007. Open-to-closed transition in apo maltose-binding protein observed by paramagnetic NMR **449**:1078–1082. doi:10.1038/nature06232
- Tikhonov DB, Magazanik LG. 2009. Origin and molecular evolution of ionotropic glutamate receptors. *Neurosci Behav Physiol* **39**:763–773. doi:10.1007/s11055-009-9195-6
- Traynelis SF, Wollmuth LP, McBain CJ, Menniti FS, Vance KM, Ogden KK, Hansen KB, Yuan H, Myers SJ, Dingledine R. 2010. Glutamate Receptor Ion Channels: Structure, Regulation, and Function. *Pharmacol Rev* **62**:405–496. doi:10.1124/pr.109.002451
- Twomey EC, Sobolevsky AI. 2018. Structural Mechanisms of Gating in Ionotropic Glutamate Receptors. *Biochemistry* **57**:267–276. doi:10.1021/acs.biochem.7b00891
- Weston MC, Schuck P, Ghosal A, Rosenmund C, Mayer ML. 2006. Conformational restriction blocks glutamate receptor desensitization. *Nat Struct Mol Biol* **13**:1120–1127. doi:10.1038/nsmb1178
- Wood MW, Vandongen HMA, Vandongen AMJ. 1995. Structural conservation of ion conduction pathways in K channels and glutamate receptors. *Proc Natl Acad Sci USA* **92**:4882–4886.
- Yelshanskaya M V., Li M, Sobolevsky a. I. 2014. Structure of an agonist-bound ionotropic glutamate receptor. *Science (80-)* **345**:1070–1074. doi:10.1126/science.1256508
- Zhang W, Cho Y, Lolis E, Howe JR. 2008. Structural and Single-Channel Results Indicate That the Rates of Ligand Binding Domain Closing and Opening Directly Impact AMPA Receptor Gating **28**:932–943. doi:10.1523/JNEUROSCI.3309-07.2008

Supplementary Table S1. Overview of GluR0 (1ii5) structure homologous substrate-binding proteins identified in the Molecular Modeling Database (MMDB) using the Vector Alignment Search Tool (VAST+) and used for the structural distance tree.

Cluster	PDB code	Uniprot	Organism	Ligand	Resolution (Å)	iGlu LBI
D	1SBP	P02906	<i>Salmonella enterica</i>	Sulfate	1.7	
D	3C9H	Q7CWZ6	<i>Agrobacterium fabrum</i>	Iron	1.9	
D	6HLZ	N/A	<i>Agrobacterium tumefaciens</i>	agropinic acid	1.89	
D	4R6Y	P96062	<i>Salmonella enterica</i>	Acetate	1.22	
D	4OMB	G3XDA8	<i>Pseudomonas aeruginosa</i>	Phosphate	1.5	
D	1XVX	A1JLH5	<i>Yersinia enterocolitica</i>	Iron	1.53	
D	3LR1	Q749P2	<i>Geobacter sulfurreducens</i>	Tungstate	1.8	
D	1PC3	P9WGU1	<i>Mycobacterium tuberculosis</i>	Phosphate	2.16	
D	2RIN	N/A	<i>Escherichia coli</i>	Acetylcholine	1.8	
D	2PT2	P72827	<i>Synechocystis sp.</i>	Iron	2.0	
D	4ELR	Q5SHV2	<i>Thermus thermophilus</i>	Iron	2.5	
D	1MRP	P35755	<i>Haemophilus influenzae</i>	Iron	1.6	
D	1Q35	Q9Z4N6	<i>Mannheimia haemolytica</i>	Iron	1.2	
D	4R75	A3N294	<i>Actinobacillus pleuropneumoniae</i>	Sedoheptulose-7-phosphate	1.28	
D	4GD5	A0A0H2YSI2	<i>Clostridium perfringens</i>	Phosphate	1.7	
D	6G7Q	Q10Z45	<i>Trichodesmium erythraeum</i>	Iron	1.2	
D	5UM2	Q8PNN7	<i>Xanthomonas citri</i>	Sulfate	1.14	
D	2H5Y	N/A	<i>Xanthomonas citri</i>	Molybdate	1.7	
D	5I84	Q8PM55	<i>Xanthomonas citri</i>	Phosphate	2.98	
D	1Y9U	Q7VXW9	<i>Bordetella pertussis</i>	Iron	1.39	
D	1URG	Q9RHZ6	<i>Alicyclobacillus acidocaldarius</i>	Maltose	1.8	
D	4KD5	Q18A64	<i>Clostridioides difficile</i>	Molybdenum	2.5	
E	2PFZ	J7G560	<i>Bordetella pertussis</i>	Pyroglutamate	1.8	
E	4N8Y	A5E8D2	<i>Bradyrhizobium sp.</i>	Alpha/Beta-d-galacturonate	1.5	
E	4MCO	Q21XD7	<i>Rhodiferax ferrireducens</i>	Malonate	1.6	
E	4X8R	A3PLM5	<i>Rhodobacter sphaeroides</i>	Glucuronate	1.9	
E	4NN3	C6BW16	<i>Desulfovibrio salexigens</i>	Orotic acid	1.4	
E	3FXB	Q5LUA7	<i>Ruegeria pomeroyi</i>	Ectoine	2.9	
E	4MNP	Q8RDN9	<i>Fusobacterium nucleatum</i>	Sialic Acid	2.5	
E	4N91	C7RDZ3	<i>Anaerococcus prevotii</i>	Apha/Beta d-glucuronate	1.7	
E	4NGU	Q311Q1	<i>Desulfovibrio alaskensis</i>	D-Alanine	2.5	
E	4MMP	N/A	<i>Pasteurella multocida</i>	Sialic Acid	1.57	
F	1ii5	P73797	<i>Synechocystis sp.</i>	Glutamate	1.6	Glu
F	4io3	E9P5T5	<i>Adineta vaga</i>	Aspartate	1.66	AvC A1
F	3epe	P19493	<i>Rattus norvegicus</i>	Glutamate	1.85	Glu
F	5fth	P19491	<i>Rattus norvegicus</i>	Glutamate	2.9	Glu
F	4f29	P19492	<i>Rattus norvegicus</i>	Glutamate	1.75	Glu
F	2f36	P22756	<i>Rattus norvegicus</i>	Glutamate	2.11	Glu
F	4Z9N	A0A0M3KL33	<i>Brucella ovis</i>	Glutathione	1.75	
F	5ORG	P0A4F8	<i>Agrobacterium tumefaciens</i>	Octopine	1.99	
F	2Q88	Q92WC8	<i>Sinorhizobium meliloti</i>	Ectoine	1.9	
F	4H5F	D6ZRZ2	<i>Streptococcus pneumoniae</i>	Arginine	1.9	

F	2IA4	A0A0H2UXX1	<i>Shigella flexneri</i>	Glutamate	1.5
F	4C0R	Q93DA5	<i>Streptococcus mutans</i>	Glutathione	1.55
F	5EYF	Q3XZW5	<i>Enterococcus faecium</i>	Glutamate	1.52
F	4F3S	Q8ZPA3	<i>Salmonella enterica</i>	Alanine	2.14
F	4I62	A0A0H2ZN67	<i>Streptococcus pneumoniae</i>	Arginine	1.05
F	3VVD	Q72JG5	<i>Thermus thermophilus</i>	Ornithine	2.05
F	4DZ1	N/A	<i>Salmonella enterica</i>	Alanine	1.9
F	6H2T	P96257	<i>Mycobacterium tuberculosis</i>	Glutamate	1.67
F	2yjp	Q5F5B5	<i>Neisseria gonorrhoeae</i>	Cysteine	2.26
F	4OHN	A0A0H2UKY8	<i>Streptococcus pneumoniae</i>	Histidine	1.37
F	1HSL	P0AEU0	<i>Escherichia coli</i>	Histidine	1.89
F	4G4P	Q837S0	<i>Enterococcus faecalis</i>	Glutamine	1.5
F	2YJP	Q5F5B5	<i>Neisseria gonorrhoeae</i>	Cysteine	2.26
F	6FXG	Q9CES5	<i>Lactococcus lactis</i>	Asparagine	1.7
F	1WDN	P0AEQ3	<i>Escherichia coli</i>	Glutamine	1.94
F	2Q2C	D0VWX8	<i>Geobacillus stearothermophilus</i>	Histidine	2.35
F	4F3P	Q3JIF9	<i>Burkholderia pseudomallei</i>	Glutamine	2.4
F	2Y7I	Q8ZKA9	<i>Salmonella enterica</i>	Arginine	1.9
F	3KZG	Q5ZV85	<i>Legionella pneumophila</i>	Arginine	2.06
F	1LAF	P02911	<i>Salmonella enterica</i>	Arginine	2.06
F	2YLN	Q5F9M1	<i>Neisseria gonorrhoeae</i>	Cysteine	1.12
F	4YMX	Q8RCC4	<i>Caldanaerobacter subterraneus</i>	Arginine	1.48
F	4PP0	P35120	<i>Agrobacterium fabrum</i>	Pyronopline	1.57
F	4EQ9	Q8DRG2	<i>Streptococcus pneumoniae</i>	Glutathione	1.4
F	4GVO	Q8Y4T3	<i>Listeria monocytogenes</i>	Cysteine	1.45
F	6HQH	A0A0F4FYR3	<i>Agrobacterium tumefaciens</i>	Deoxyfructosylglutamine	1.8
F	4OXV	A0A0J9X1Z1	<i>Pseudomonas aeruginosa</i>	Valinine	2.2
F	2V25	Q0P9X8	<i>Campylobacter jejuni</i>	Aspartate	1.49
F	6EU7	L0NML6	<i>Rhizobium sp</i>	Arsenite	3.0
F	5LV1	A3PDP9	<i>Prochlorococcus marinus</i>	Phosphite	2.12
F	2G29	P73452	<i>Synechocystis sp.</i>	Nitrate	1.5
F	3N5L	Q9HYL8	<i>Pseudomonas aeruginosa</i>	Phosphonate	1.97
F	2O1M	O34852	<i>Escherichia coli</i>	Arginine	2.0
F	2I4B	Q55460	<i>Synechocystis sp.</i>	Bicarbonate	1.35
F	6EMN	O69061	<i>Pseudomonas stutzeri</i>	Phosphite	1.25
F	5O37	O69052	<i>Pseudomonas stutzeri</i>	Methylphosphonate	1.37
F	5LQ1	Q119I9	<i>Trichodesmium erythraeum</i>	Methylphosphonate	1.41
F	3P7I	Q1R3F7	<i>Escherichia coli</i>	2-aminoethyl phosphonate	1.71
F	1D9Y	Q50964	<i>Neisseria gonorrhoeae</i>	Iron(III) ion	2.2
F	3I6V	Q5LTV6	<i>Ruegeria pomeroyi</i>	Lysine	2.0
F	3N26	Q9Z869	<i>Chlamydia pneumoniae</i>	Arginine	2.1
F	5LQ5	A3PC74	<i>Prochlorococcus marinus</i>	Phosphite	1.41
F	4PSH	Q9WZ62	<i>Thermotoga maritima</i>	Arginine	2.6
F	3KSX	Q8PHQ1	<i>Xanthomonas citri</i>	Alkanesulfonate	1.7
F	3UN6	Q2G1I5	<i>Staphylococcus aureus</i>	Zinc ion	2.01
F	4YAH	P28635	<i>Escherichia coli</i>	Methionine	1.6

F	4LAT	Q97Q31	<i>Streptococcus pneumoniae</i>	Phosphate	1.88
F	3HV1	Q5M4P7	<i>Streptococcus thermophilus</i>	Polar amino acids	1.9
F	2X26	P75853	<i>Escherichia coli</i>	Sulphonate	1.75
F	2REG	Q92N37	<i>Rhizobium meliloti</i>	Choline	1.9
F	4GOT	O32167	<i>Bacillus subtilis</i>	Methionine	1.95
F	3TMG	O51169	<i>Borrelia burgdorferi</i>	compatible solute Glycine Betaine	1.9
F	3IX1	Q9K9G5	<i>Bacillus halodurans</i>	N-formyl-4-amino-5-aminomethyl-2-methylpyrimidine	2.4

Chapter IV: Electrical Sensing of Phosphonates by Functional Coupling of Phosphonate Binding Protein PhnD to Solid-State Nanopores

This chapter has been published in:

Bernhard M, Diefenbach M, Biesalski M, Laube B. *Electrical Sensing of Phosphonates by Functional Coupling of Phosphonate Binding Protein PhnD to Solid-State Nanopores*. ACS Sens. 2020 Jan 24;5(1):234-241. doi: 10.1021/acssensors.9b02097.

Contributions:

M.B. hat das Manuskript geschrieben (Introduction; Materials and Methods: PhnD cloning, Overexpression and Purification of PhnD, Microscale Thermophoresis, Conjugation of PhnD to P(DMAA-co-NMAS, Coupling of Proteins to P(DMAA-co-NMAS) Functionalized Single Solid-State Nanopores, Microscopy, Mass Spectrometry, Electrical Recordings and Data Analysis; Results and Discussion; Conclusion).

M.B. hat folgende Abbildungen und Abbildungslegenden erstellt: Abstract Figure, Figure 1, Figure 2b und c, Figure 3, Figure 4.

M.B. hat folgende Experimente und Analysen durchgeführt: PhnD Cloning, Overexpression and Purification of PhnD, Microscale Thermophoresis, Coupling of Proteins to P(DMAA-co-NMAS) Functionalized Single Solid-State Nanopores, Microscopy, Electrical Recordings and Data Analysis

M.D. hat die Sektionen Fabrication of Single Solid-State Nanopores, Polymer Functionalization of Track-Etched Membranes geschrieben.

M.D. hat die Abbildung Figure 2a erstellt.

M.D. hat folgende Experimente durchgeführt: Fabrication of Single Solid-State Nanopores, Polymer Functionalization of Track-Etched Membranes.

M.B. und M.D. haben die Massenspektroskopischen Experimente durchgeführt.

M.B., M.D., M.Bi. und B.L. waren an der Konzipierung der Experimente beteiligt.

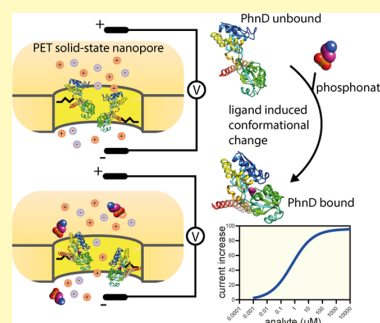
M.Bi. und B.L. betreuten das Projekt und überarbeiteten das Manuskript.

Electrical Sensing of Phosphonates by Functional Coupling of Phosphonate Binding Protein PhnD to Solid-State Nanopores

Max Bernhard,[†] Mathias Diefenbach,[‡] Markus Biesalski,^{‡,§} and Bodo Laube^{*,†,§}[†]Department of Biology, Neurophysiology and Neurosensory Systems, Technische Universität Darmstadt, Schnittspahnstrasse 3, 64287 Darmstadt, Germany[‡]Department of Chemistry, Laboratory of Macromolecular Chemistry and Paper Chemistry, Alarich-Weiss-Str. 8, 64287 Darmstadt, Germany

ABSTRACT: Combining the stability of solid-state nanopores with the unique sensing properties of biological components in a miniaturized electrical hybrid nanopore device is a challenging approach to advance the sensitivity and selectivity of small-molecule detection in healthcare and environment analytics. Here, we demonstrate a simple method to design an electrical hybrid nanosensor comprising a bacterial binding protein tethered to a solid-state nanopore allowing high-affinity detection of phosphonates. The diverse family of bacterial substrate-binding proteins (SBPs) binds specifically and efficiently to various substances and has been implicated as an ideal biorecognition element for analyte detection in the design of hybrid bionanosensors. Here, we demonstrate that the coupling of the purified phosphonate binding protein PhnD via primary amines to the reactive NHS groups of P(DMAA-co-NMAS) polymers inside a single track-etched nanopore in poly(ethylene terephthalate) (PET) foils results in ligand-specific and concentration-dependent changes in the nanopore current. Application of the phosphonate 2-aminoethylphosphonate (2AEP) or ethylphosphonate (EP) induces a large conformational rearrangement in PhnD around the hinge in a venus flytrap mechanism resulting in a concentration dependent increase of the single pore current with binding affinities of 27 and 373 nM, respectively. Thus, the specificity and stability of this simple hybrid sensor concept combine the advantages of both, the diversity of ligand-specific substrate-binding proteins and solid-state nanopores encouraging further options to produce robust devices amenable to medical or environmental high-throughput-based applications in nanotechnology.

KEYWORDS: PhnD, periplasmic binding proteins, substrate-binding proteins, protein immobilization, analyte sensing, phosphonates, solid-state nanopores



In the last decade, miniaturized electrical biosensors are a promising tool for analyzing and monitoring environmental pollutants and diagnostically relevant substances in personalized healthcare. Major advances in this field rely on synthetic fabricated solid-state nanopores,^{1–3} modified β -barrel pores,^{4,5} modified ion channels,^{6,7} and more recently on DNA origami.⁸ In general, molecules can be analyzed by the change in ionic current through a nanopore when they enter or interact with the pore surface under an externally applied voltage. While solid-state nanopores have some advantages over biological nanopores, for instance, easy manufacturing and enhanced physicochemical stability,⁹ they often lack the evolutionary evolved sensitivity and selectivity of proteins and protein domains. The combination of biologically active units with solid-state nanopores is widely used for sensing of large macromolecules, for instance, antibodies,¹⁰ protein toxins,¹¹ or whole proteins^{2,12,13} or for the catalytic oxidation of a target analyte by immobilized enzymes.¹⁴ Nevertheless, the specific detection and analysis of biologically relevant small molecules remain a major challenge. Therefore, one key element is the production and incorporation of a molecular detector to an electrical sensing platform.

Due to a wide range of recognized ligands and a conserved binding mechanism, bacterial substrate-binding proteins (SBPs) have been implicated as an ideal biorecognition element and may function as an active component for analyte recognition in the design of a new class of biosensors.^{15–20} SBPs are one of the largest prokaryotic protein families. They evolved for the specific and efficient binding and transport of various substances across the cell membrane and further mediate chemotactic responses.²¹ In general, they are thermal stable proteins up to 90 °C,^{22,23} consisting of two globular subdomains connected by a hinge region, forming a characteristic clamshell-like structure.²⁴ Ligand binding takes place between the interface of the two subdomains and induces a large conformational rearrangement around the hinge in a venus-flytrap mechanism,²⁵ which might result in a change of the molecular surface area.^{26,27} This large conformational change can be generally used to monitor different cognate ligands.^{15,28} Combining the advantages of solid-state nano-

Received: October 25, 2019

Accepted: December 12, 2019

Published: December 12, 2019

pores serving as sensing platform with the high sensitivity and selectivity of SBP as sensor elements may enable the robust analysis of various small compounds.²⁹

As an ideal candidate for a hybrid biosensor composed of a functionally coupled SBP to a solid-state nanopore, we choose the phosphonate binding protein PhnD, a member of class II SBPs, for sensing phosphonates as a proof-of-principle approach. Under phosphorus-limiting conditions, the SBP PhnD is part of a ABC transporter-mediated phosphonate uptake system in *Escherichia coli* and bind various compounds such as 2-aminoethylphosphonate (2AEP), ethylphosphonate (EP), phosphate, glyphosate, and the nerve agent degradation products ethylmethylphosphonic acid (EMPA), isopropylmethylphosphonic acid (IMPA), and pinacolyl methylphosphonic acid (PMPA).³⁰ Phosphonates are characterized by a stable carbon to phosphorous bond and include various natural and anthropogenic compounds. The most abundant natural phosphonate 2AEP is found as a precursor in phosphonolipid,³¹ phosphoglycan,³² and phosphonoprotein³³ biosynthesis. Synthetic phosphonates are mostly used as chelating agents in numerous industrial applications³⁴ and further include drugs like antibiotics³⁵ and antivirals,³⁶ the herbicide glyphosate, insecticides,³⁷ and degradation products of chemical warfare agents such as sarin, soman, and VX.³⁸ Despite the environmental and medical importance of phosphonates no reliable analytical methods with detection limits beneath the lower micromolar range are available.³⁴ Here, we demonstrate that the coupling of the phosphonate binding protein PhnD via P(DMAA-co-NMAS) polymers inside a single track-etched nanopore result in high-affinity ligand-specific and concentration-dependent change in the nanopore current. This highlights the use of PhnD, functionally immobilized inside solid-state nanopores, as a promising electrical hybrid nanosensor for the specific detection of phosphonates in particular and the potential application of SBPs as an easily exchangeable recognition element for the recognition of a wide range of analytes in diverse samples.

MATERIALS AND METHODS

PhnD Cloning. PhnD was constructed and cloned using Gibson assembly. Therefore, pET28a(+) vector was linearized by standard PCR using the following primers: GCTGTGATGATGATGATGATGG and TGGCTAGCATGACTGGTG. To remove the maternal vector DNA, the amplified PCR product was digested with DpnI and further purified by gel extraction using the QIAquick Gel Extraction Kit (Qiagen) according to the manufacturer's instruction. For further protein purification, an N-terminal 6X histidine-tag followed by a short linker sequence (SEPRS) was incorporated into the PhnD sequence (UniProt ID Q0T9T8). Synthesized PhnD fragment (GeneArt Gene Synthesis, Invitrogen) was cloned by Gibson assembly using the NEBuilder HiFi DNA Assembly Cloning Kit (New England Biolabs) according to the manufacturer's instruction. Gibson assembly mixture was transformed into *E. coli* Top10 by heat shock transformation. The identity of the clone was confirmed by sequencing.

Overexpression and Purification of PhnD. PhnD containing an N-terminal His₆-tag was expressed in *E. coli* BL-21 DE3 in LB medium at 37 °C and protein expression was induced with 1 mM IPTG at OD_{600nm} = 0.8. Three hours after IPTG induction, cells were harvested by centrifugation at 6000g for 20 min at 4 °C, resuspended in buffer A (40 mM Tris-HCl pH 8.0, 300 mM NaCl, 10 mM Imidazole), and lysed by sonification. Insoluble cell debris was removed by centrifugation at 20000g for 20 min at 4 °C. The supernatant was loaded in a 1 mL Ni-NTA Superflow Cartridge (Qiagen) equilibrated with buffer A, connected to an Äkta pure (GE

Healthcare). The column was washed with 6 CV buffer A supplemented with 40 mM imidazole. Protein was eluted in 6 CV buffer A supplemented with 250 mM imidazole, dialyzed overnight against 50 mM NaCl, 5% glycerol and 10 mM Tris-HCl pH 7.9, subsequently frozen in liquid nitrogen, and stored at -80 °C. Protein expression and purification were analyzed using a 12% sodium dodecyl sulfate-polyacrylamide gel electrophoresis (SDS-PAGE) stained with Roti Blue (Carl Roth). For western blot, separated proteins were transferred to PVDF membrane (Bio-Rad). The membrane was blocked for 1 h in TBS containing 0.05% (v/v) Tween 20 (TBS-T) supplemented with 5% skim milk. After the blockade, the membrane was incubated with 1:500 diluted primary His-Tag Antibody (HIS.H8) (Thermo Fisher Scientific) in TBS-T containing 1% skim milk overnight at 4 °C. The membrane was washed three times for 10 min with TBS-T and incubated with the appropriate secondary goat anti-rabbit IgG-HRP (sc-2054, Santa Cruz Biotechnology) in TBS-T containing 1% skim milk for 1 h at room temperature. The membrane was washed three times for 10 min in TBS-T. Signal was visualized by adding Pierce Western Blotting Substrate (Thermo Fisher Scientific) and detected with a CCD camera.

Microscale Thermophoresis. For determining the binding constants of PhnD by microscale thermophoresis, the buffer was exchanged to buffer B (100 mM KCl, 0.5 mM CaCl₂, and 10 mM Tris-HCl pH 7.4) using a Vivaspin 2000 (Sartorius). Protein concentration was determined by Pierce BCA Protein Assay Kit (Thermo Fisher Scientific). Microscale thermophoresis (MST) analysis was performed using a Nano Temper Monolith NT.115 instrument. Therefore, PhnD was diluted to a concentration of 200 nM in the appropriate buffer and was fluorescence-labeled using the Monolith NT His-Tag Labeling Kit RED-tris-NTA (Nano Temper Technologies). Labeled PhnD (final concentration 50 nM) was added in a 1:1 ratio to a 1:2 EP or 2AEP dilution series with a final EP concentration of 100 μM down to 3 nM and loaded into standard capillaries (Monolith NT.115 Capillaries). Thermophoresis was measured at 21 °C for 15 s with 40% LED power and 40% infrared laser power. Data were analyzed using the NT Analysis software (Nanotemper). Binding affinities were obtained by plotting the normalized fluorescence change against the 2AEP or EP concentration and fit with a nonlinear regression with variable Hill slope in GraphPad Prism 7 (GraphPad Software Inc.).

Fabrication of Single Solid-State Nanopores. Single solid-state nanopores were prepared using the track-etching technique. Therefore, circular poly(ethylene terephthalate) (PET) foils with a diameter of 30 mm and a thickness of 12 μm were irradiated with single swift heavy Au ions of kinetic energy 5.9 MeV/nucleon at the universal linear accelerator UNILAC (GSI Helmholtz Centre for Heavy Ion Research, Darmstadt, Germany). For cylindrical shaped channels, the protocol developed by Nguyen et al.³⁹ was used. Prior to etching, the heavy ion tracked membranes were irradiated with UV light at 312 nm for 1 h. Next, the membranes were immersed in a double-walled preheated beaker at 35 °C in 9 M NaOH solution for 25 min. After the membranes were removed from the etching solution, they were rinsed several times with distilled water. Finally, the membranes were extracted in millipore water overnight to remove the residues of the etching process and air-dried. The pore diameters were calculated from IV curves according to Cornelius et al.⁴⁰ with the formula for cylindrical nanopores.

Polymer Functionalization of Track-Etched Membranes. The functionalization of the membranes was done in four consecutive steps. In the first step, the carboxyl groups on the surface of the membrane were transformed into amine groups using the active ester chemistry described on these systems by Papra et al.⁴¹ Next, the CTA for the RAFT polymerization was coupled, which was introduced also as its active ester species, according to Chen et al.⁴² In the third step, the reactive copolymer was polymerized by a modified protocol of Jiang et al.⁴³ At last, the protein was coupled to the polymer. The reaction scheme is schematically outlined in Figure 2a. Briefly, the track-etched membranes were placed into a beaker and immersed in a freshly prepared solution of *N*-(3-dimethylaminopropyl)-*N'*-ethyl-

carbodiimide hydrochloride (EDC, 100 mM) and pentafluorophenol (PFP, 200 mM) in dry ethanol. The beaker was sealed and after 1 h at room temperature, the solution was replaced by ethylenediamine (EDA, 100 mM) in dry ethanol, sealed again, and left overnight. Subsequently, the membranes were washed with ethanol to remove any unbound species. The coupling of the CTA was done in the same setup as described for the amination before. In brief, the membranes were exposed to a solution of 4-cyano-4-(dithiobenzoyl)pentanoic acid *N*-succinimidyl ester (CPDB-NHS, 100 mM) in dry DMF overnight, after which they were washed with dry DMF and millipore water, and dried at ambient condition. In a 50 mL Schlenk tube, a PTFE sample holder, a stir bar, and one CTA coupled membrane were degassed by three high vacuum pump/N₂ refill cycles. An additional Schlenk flask was used to separately prepare the polymerization solution. In 144 mL dry 1,4-dioxane 40 mL destabilized *N,N*-dimethylacrylamide (DMAA), 3.36 g methacrylic acid *N*-hydroxysuccinimide ester (NMAS), 84 mg 4,4'-azobis(4-cyanopentanoic acid) (AIBN), and 0.36 g 4-cyano-4-(dithiobenzoyl)-pentanoic acid were dissolved and degassed by N₂ (g) bubbling for 30 min. This solution was syringed into the Schlenk tube containing the membrane, adding enough liquid to fully cover it. The flask was immersed in a preheated oil bath at 70 °C. After 6 h, the polymerization was stopped by immersing the membrane into ice-cold 1,4-dioxane and precipitation of the free polymer in the 10-fold volume of diethylether. The polymer was decanted off and dried in a vacuum while the membrane was extracted overnight in 1,4-dioxane and dried afterward. Both, the membrane and the free polymer were stored in the fridge until coupling to the protein. Yield: 35%; $M_n = 1000$ g/mol; MWD = 1.31.

Conjugation of PhnD to P(DMAA-co-NMAS). For conjugation of PhnD to free P(DMAA-co-NMAS), buffer was exchanged to buffer C (100 mM NaCl, 20 mM HEPES, pH 8.0). FITC (2 mg) conjugated 5% P(DMAA-co-NMAS) in 100 μ L buffer C was added to 100 μ L PhnD (2 mg/mL) and incubated at 18 or 30 °C for 24 h. Protein conjugation was analyzed as described above.

Coupling of Proteins to P(DMAA-co-NMAS) Functionalized Single Solid-State Nanopores. To functionally couple PhnD, BSA or GFP, 2 mL of a 1 mg/mL protein solution in buffer C was dropped to the prefucionalized single solid-state nanopore and incubated at 18 °C for 24 h. To eliminate all non-reacted NHS groups, the reaction was quenched by washing the foil with Tris-buffer (100 mM NaCl, 50 mM Tris-HCl pH 7.4) and incubated for 2 h at 18 °C.

Microscopy. GFP functionalized multipores were examined using a Leica TCS SP5 CLSM. Samples were excited at 488 nm and emission was detected at 525 nm. For 3D rendering, 83 pictures per stack with 0.13 μ m steps in z-axis were analyzed using ImageJ.

Mass Spectrometry. All spectra were recorded on an Autoflex speed TOF/TOF (Bruker Daltonik) using a DHAP matrix. Data were analyzed using the mMass software.

Electrical Recordings and Data Analysis. Prior electrical recordings of the prepared single nanopores, the foils were washed with recording buffer B. The recording setup consisted of two chambers with a volume of 500 μ L each, where the foil was fixed between. Before measurement, foils were incubated with the appropriate ligand in buffer B for 5 min. The current was recorded by IV measurements between -100 and 100 mV and current for K_d analysis was obtained at -80 mV using an eOne-VP amplifier (Elements) and Elements Data Reader 3 software. Data were sampled at 5 kHz. Analysis and statistical tests were carried out using GraphPad Prism 7 software (GraphPad Software Inc.). Binding affinities were obtained by plotting the current amplitude against 2AEP or EP concentration and fitted with nonlinear regression with variable Hill slope in Prism. Values given represent means \pm SEM. Statistical significance was determined at the $p < 0.05$ (*), $p < 0.01$ (**), and $p < 0.001$ (***) levels using a one-way ANOVA and a Dunnett post-hoc analysis.

RESULTS AND DISCUSSION

Heterologous Expression and Characterization of PhnD.

In this work, we used the SBP PhnD as a biological recognition element, which binds various phosphonates with high selectivity and sensitivity up to subnanomolar concentrations.⁴⁴ In the absence of a ligand, PhnD remains in an open conformation. Binding of a cognate ligand between the interface of the two-lobed PhnD subdomains results in a closure of the clamshell-like structure by rotating lobe 2 about 70° towards lobe 1^{15,45,46} (Figure 1a), resulting in a decrease in

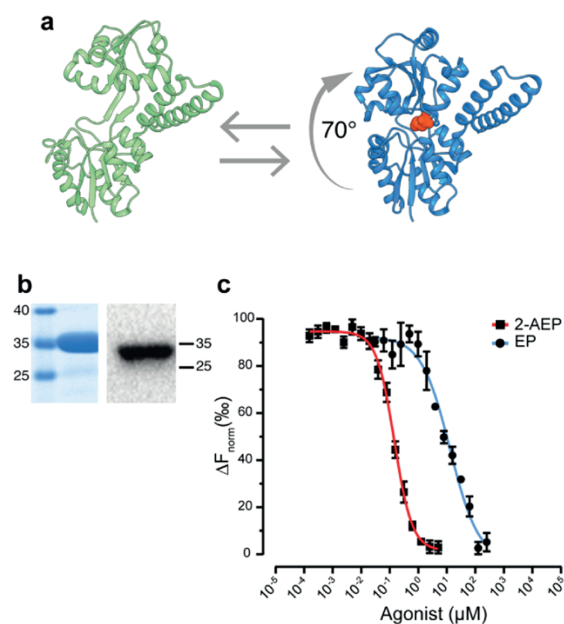


Figure 1. Characteristics of phosphonate binding protein PhnD. (a) Cartoon of PhnD displaying the open, ligand-free (green; PDB 3S4U) and closed 2AEP-bound conformation (blue; PDB 3P7I). Ligand (red) binding takes place between the interface of the two-lobed subdomains and induces a large conformational change by rotating the lower domain of the binding protein approximately 70° towards the upper domain. (b) Coomassie gel (left) and western blot (right) of Ni-NTA purified PhnD with a molar mass of 36 kDa. (c) MST binding curves of 2AEP ($n = 3$) and EP ($n = 4$) dilution series performed in 100 mM K⁺, 0.5 mM CaCl₂, 10 mM Tris-HCl set at pH 7.4. PhnD shows K_d values of 145 ± 10 nM and 8.1 ± 3.7 μ M in bulk for 2AEP and EP, respectively. Error bars represent the standard error from 3–4 independent experiments.

the accessible surface area of 7.7% from 14.3×10^3 to 13.2×10^3 \AA^2 . First, we examined whether our *E. coli* BL-21 (DE3) expressed His₆-PhnD generates a functional soluble phosphonate binding protein. SDS-PAGE and western blot analysis after Ni-NTA column purification revealed a single band of ~ 35 kDa indicating successful purification with high purity (Figure 1b). Next, we determined the substrate-binding thermodynamics of phosphonates in our purified PhnD by microscale thermophoresis. Analysis of the dissociation constants for 2AEP and EP revealed a K_d of 145 ± 10 nM and 8.1 ± 3.7 μ M with a Hill coefficient of approximately 1 (Figure 1c). Although these K_d values are slightly higher compared to previously described constants in sodium buffer,⁴⁴ our results demonstrate that our protein displays

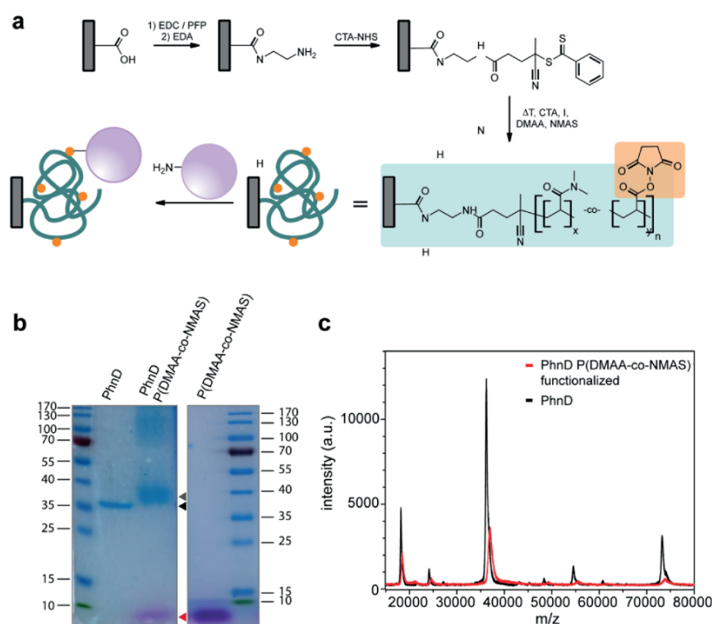


Figure 2. Coupling of PhnD to P(DMAA-*co*-NMAS). (a) Schematic description of the two-step anchoring of the chain transfer agent (CTA) prior to the surface-initiated RAFT polymerization of P(DMAA-*co*-NMAS) on the inner pore surface. The CTA is needed to be immobilized, ensuring that the surface-initiated polymer chains grow in a controlled manner. In addition, it serves as an anchor for the polymer chains. Due to the controlled character of the polymerization, there is a more homogeneous distribution of the polymer on the pore surface. The polymer (green lines) acts as a long and flexible linker for the proteins (purple circles). They react covalently with their primary amines on the protein surface to the reactive NHS group (orange dots) of P(DMAA-*co*-NMAS)-polymer. For further details of the surface polymerization refer to the experimental section. (b) SDS-PAGE of P(DMAA-*co*-NMAS) conjugated (grey arrow) and nonconjugated (black arrow) PhnD. Nonconjugated PhnD has a molecular weight of 36 kDa. Free P(DMAA-*co*-NMAS) is colored red (red arrow) and has an average mass of 1 kDa. (c) MALDI-TOF mass spectrometry of conjugated (red) and nonconjugated (black) PhnD. The main peak of PhnD is shifting from 36.2 to 37.04 kDa after conjugation. Mass increment corresponding to the mass of free P(DMAA-*co*-NMAS).

the specific binding properties and affinities of the wild-type PhnD.

Coupling of P(DMAA-*co*-NMAS) to PhnD. In general, our idea to functionalize a nanopore surface with proteins can be described in two steps (Figure 2a). In brief, carboxyl groups present at the surface of track-etched nanopore membranes are converted into amine groups by a simple amidation reaction.⁴⁷ In a subsequent step, a copolymer poly((*N,N'*-dimethylacrylamide)-*co*(methacrylic acid *N*-hydroxysuccinimide ester)), P(DMAA-*co*-NMAS), was in situ prepared by a surface-initiated RAFT polymerization. The copolymer contains small amounts of a reactive NHS group, where the composition of the copolymer is controlled by adjusting an appropriate monomer concentration of DMAA and NMAS monomer, respectively. In the subsequent step, the respective proteins are conjugated via primary amines to the reactive NHS groups to the nanopore surface. To characterize the protein–polymer conjugate within the pores, we analyzed the coupling efficacy by a reference measurement using a free copolymer, with an average molar mass of $M_n = 1000$ Da and PhnD with a molecular weight of 36 kDa, respectively. The resulting conjugates were analyzed using SDS-PAGE and MALDI-TOF mass spectrometry (Figure 2b,c). A shift in molecular weight about 1–3 kDa in SDS-PAGE analysis and 800 Da in MALDI-TOF mass spectrometer analysis of FITC-conjugated P(DMAA-*co*-NMAS)-coupled PhnD compared to uncoupled protein could be observed. Furthermore, an additional band above 70 kDa could be seen in SDS-PAGE, caused by the

conjugation of at least two proteins per polymer strand. This is possible because the polymer contains statistically more than one NMAS group, and therefore a single macromolecule can link to two adjacent proteins. This strongly indicates a successful and efficient NHS-conjugation of PhnD to P(DMAA-*co*-NMAS) polymer.

Functional Coupling of PhnD to Solid-State Nanopores. To demonstrate the coupling-capability of proteins inside a P(DMAA-*co*-NMAS)-functionalized solid-state nanopore, we, therefore, used the fluorescent protein GFP with a similar mass (28 kDa) as PhnD. Confocal microscopy images show a defined GFP-mediated fluorescence signal at the pore surface that can be detected nearly in its entire length (Figure 3a). Since only a faint GFP signal could be seen on the foil surface, this may indicate that protein coupling is relieved within the nanopore. However, whether this may be due to a differential coupling efficiency or distribution pattern of carboxy groups between the foil and pore surfaces has not been investigated so far. In the next step, we covalently attached PhnD with a short P(DMAA-*co*-NMAS)-polymer linker to the surface of a single solid-state nanopore. The nanopores were fabricated in a 12 μ M PET foil with a track-etching method by irradiation of the foil with a single heavy ion and subsequent etching in alkaline solution.⁴⁸

For the 2AEP experiments, pores with a diameter of 148, 197, 220, and 340 nm, and for EP experiments, pores with a diameter of 130 and 180 nm were used. The principle idea of our hybrid sensor is that the large conformational protein

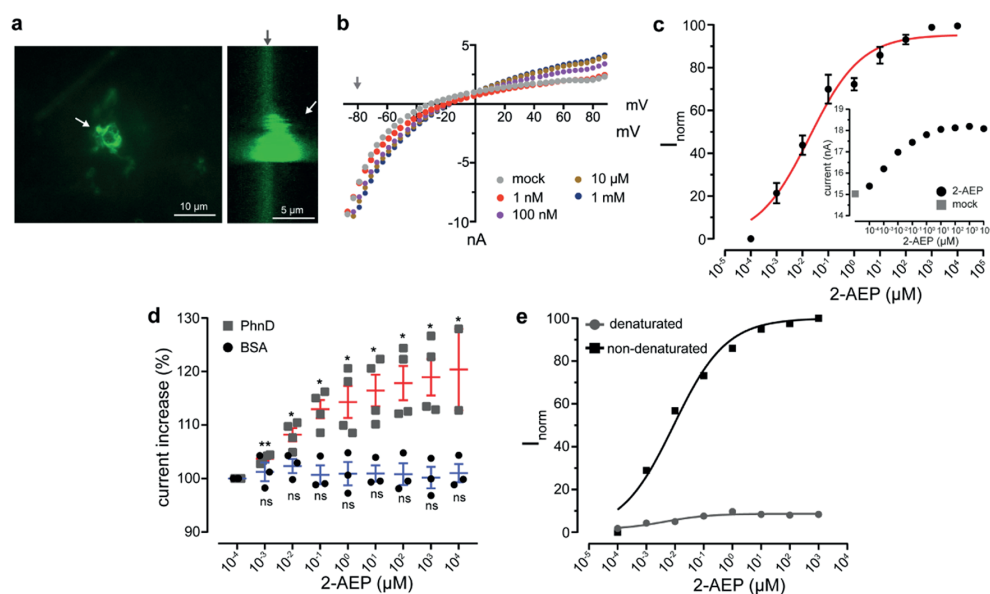


Figure 3. Functional characterization of the single solid-state nanopore-based phosphonate sensor. (a) Confocal microscopy images of protein immobilization at the pore surface by coupling GFP to a P(DMAA-*co*-NMAS)-functionalized nanopore. GFP signal is enriched inside the nanopore (white arrow) and can be detected nearly at its entire length (stacked X-axis (right)). Foil surface is marked with a gray arrow. (b) IV curve of a PhnD-functionalized nanopore without (mock) and with increasing 2AEP concentrations. For all electrical recordings, a solution with 100 mM KCl, 0.5 mM CaCl₂, and 10 mM Tris-HCl at pH 7.4 was used. For K_d values, data points were obtained at -80 mV (gray arrow). (c) Dose dependency of the phosphonate sensor to increasing concentrations of 2AEP at -80 mV with a calculated K_d of 27 ± 17 nM. Error bars represent the standard error of four independent nanopores. Inset shows an example measurement of currents without (mock) and with increasing 2AEP concentrations. (d) Analysis of putative nonspecific adsorption effects of 2AEP on nanopore currents. While PhnD-coupled nanopores display concentration-dependent current changes ($p < 0.05$; one-way ANOVA test, $n = 4$), BSA functionalized nanopores show no effect ($p > 0.05$; one-way ANOVA test; $n = 3$). (e) 2AEP dose–response curve of a PhnD-functionalized nanopore before and after denaturation (70 °C and 2% SDS (w/v)).

transition of PhnD upon ligand binding inside the nanopore can be monitored as an altered ionic current when a bias voltage is applied. Therefore, in our experimental setup the PET foil containing the functionalized nanopore was clamped between two chambers, containing 100 mM KCl, 0.5 mM CaCl₂, and 10 mM Tris-HCl set at pH 7.4. Equimolar ratios of increasing ligand concentrations were added to the cis and trans side of the chamber and the K_d was determined at -80 mV upon analyzing IV curves (Figure 3b). The addition of 2AEP and EP lead to a concentration depended on increase of the single pore current with an average maximal current change of 3.3 ± 0.8 nA. Binding affinities for 2AEP (27 ± 17 nM; independent experiments from $n = 4$ different nanopores) (Figure 3c) and EP (827 and 125 nM; independent experiments from $n = 2$ different nanopores) were obtained by fitting the concentration-dependent current increase to a Hill function with a coefficient of around 0.5. Since PhnD harbors only a single binding site,⁴⁵ Hill coefficients below 1 may indicate a mixed protein population with different binding affinities inside the nanopore. In general, it has been shown that polymer conjugation to proteins can affect conformational stability and kinetic properties.^{49,50} Since the conjugation of P(DMAA-*co*-NMAS) to the putative 27 accessible primary amines at the protein surface is probably more random, the individual conjugation sites may differently affect ligand binding. Because of its polar nature and the tendency for strong surface adsorption,⁵¹ we further analyzed nonspecific binding and interactions between 2AEP and the nanopore

surface, the polymer matrix and the protein surface. We, therefore, coupled BSA instead of PhnD to functionalized nanopores with similar pore diameters used in the 2AEP experiments. Likewise PhnD, also BSA could be conjugated to P(DMAA-*co*-NMAS) (not shown). No change in the current amplitude could be observed after the addition of 2AEP, indicating that there is no nonspecific adsorption of the ligand to the pore surface or polymer matrix (Figure 3d). Additionally, to ensure that the phosphonate-induced current change is caused by the specific binding and subsequent conformational protein change, nanopores functionalized with PhnD were thermally denatured in the presence of SDS. Denaturation resulted in a drastic decrease of the signal amplitude (Figure 3e). Altogether, our results indicate that (i) proteins confined inside nanopores remain functional and (ii) the specific binding of cognate ligands to conjugated PhnD induces a specific change in the nanopore current.

CONCLUSIONS

Here, we demonstrate that PhnD immobilized inside a single solid-state nanopore is capable of transducing and amplifying specifically the binding of phosphonates into a proportionate electrical signal. Interestingly, the polymer conjugation seems not to alter the binding properties of PhnD, indicating that (i) PhnD confined inside nanopores remain biologically functional and (ii) that the conformational stability and pharmacokinetic are not different inside the nanopore compared to bulk. Common analytical assays for phosphonates are mainly based

on ion-chromatography in combination with the detection of post-column reacted Fe(III)-complexes or with pulsed amperometric detection for amine-containing phosphonates and exhibit detection limits above $1 \mu\text{M}$.³⁴ The detection limit of our constructed phosphonate hybrid sensor is by a factor of 10^2 to 10^3 for EP and 2AEP lower than classical analytical methods, respectively. Due to the distinct binding selectivity and affinity of SBPs, it should be possible to distinguish between different ligands in solution and to estimate their concentration by our hybrid nanosensor system. Following this strategy, solid-state nanopores with coupled SBPs as a molecular sensor domain might be integrated in miniaturized low cost and portable electrical devices for real-time measurements with high selectivity and affinity. Figure 4 illustrates the

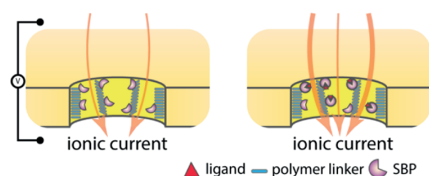


Figure 4. Principle of a hybrid sensor by functionally coupling SBPs into a single solid-state nanopore. SBPs (purple) are covalently immobilized by a short polymer linker (blue) to the inner wall of a nanopore. The binding of cognate ligands (red) to coupled PhnD induces a large conformational change by rotating the lower subdomain towards the upper subdomain. This conformational compression culminates in a decrease in the surface area, which results in an increase of ionic current through the nanopore.

basic principle of such constructed SBP biosensors. The SBPs are covalently attached with a short polymer linker P(DMAA-co-NMAS) to the surface of a single solid-state nanopore fabricated in a $12 \mu\text{M}$ PET foil. The NHS-conjugation to abundantly found primary amines at the protein surface enables a simple covalent immobilization of SBPs inside the nanopore without excessive protein engineering. Thus, since our approach uses highly soluble native proteins and does not require elaborated genetic engineering and expensive equipment, this allows overexpression and harvesting of SBPs in large quantities at low cost. Furthermore, compared to the use of SBPs in sensing analytes via fluorescence detection, surface-tethered fluorescence resonance energy transfer (FRET)-based detection, enzymatic detection, surface plasmon resonance, quartz crystal microbalance analysis or potentiometry, incorporation of SBPs in solid-state nanopores allows label-free signal amplification by measuring simple ionic currents with the potential of high-throughput screening. The conformational transition of the SBPs inside the nanopore upon ligand binding can be monitored as an increased ionic current when a bias voltage is applied. Remarkably, upon application of 2AEP, we obtained in our PhnD-coupled solid-state nanopore a relatively large change in current amplitude (up to several nA) compared to the change seen in a biological pore coupled to a single SBP (few pA).¹⁵ This difference may be attributed to (i) an accumulating effect of the higher amount of PhnD proteins coupled inside our nanopore and/or (ii) the large conformational change of our PhnD SBP upon binding. However, the current changes upon conformational rearrangement are probably mediated by alterations in the accessible surface area of the SBP although the net charge of the surface area is only slightly altered by 6.41×10^{-19} C. In

conclusion, the variety of myriad of ligands naturally recognized by SBPs enables a broad range of application areas for real-time detection of biologically relevant analytes from biological or environmental samples upon incorporation in solid-state nanopores.

■ AUTHOR INFORMATION

Corresponding Author

*E-mail: laube@bio.tu-darmstadt.de. Phone: +49-6151-16-20970.

ORCID

Markus Biesalski: 0000-0001-6662-0673

Bodo Laube: 0000-0002-2482-3189

Author Contributions

M.B., M.D., M.Bi., and B.L. conceived and designed the experiments; M.B. and M.D. performed the experiments; M.B. and M.D. analyzed the data; M.B., M.Bi., and B.L. wrote the paper.

Funding

This work has been supported in the frame of the LOEWE project iNAPO by the Hessen State Ministry of Higher Education, Research and the Arts. The authors acknowledge support by the German Research Foundation and the Open Access Publishing Fund of Technische Universität Darmstadt.

Notes

The authors declare no competing financial interest.

■ ACKNOWLEDGMENTS

The authors thank Professors Wolfgang Ensinger and Gerhard Thiel (TU Darmstadt, Germany) for their support. They also thank Prof. C. Trautmann, Department of Materials Research at GSI Helmholtz-Institute for Heavy Ion Research for providing the heavy ion irradiated PET membranes.

■ ABBREVIATIONS

2AEP, 2-aminoethylphosphonate; EP, ethylphosphonate; SBP, substrate-binding protein

■ REFERENCES

- (1) Dekker, C. Solid-State Nanopores. *Nat. Nanotechnol.* **2007**, *2*, 209–215.
- (2) Wei, R.; Gatterdam, V.; Wieneke, R.; Tampé, R.; Rant, U. Stochastic Sensing of Proteins with Receptor-Modified Solid-State Nanopores. *Nat. Nanotechnol.* **2012**, *7*, 257–263.
- (3) Knoll, W.; Ali, M.; Yameen, B.; Azzaroni, O.; Neumann, R.; Ensinger, W. Synthetic Proton-Gated Ion Channels via Single Solid-State Nanochannels Modified with Responsive Polymer Brushes. *Nano Lett.* **2009**, *9*, 2788–2793.
- (4) Soskine, M.; Biesemans, A.; Maglia, G. Single-Molecule Analyte Recognition with ClyA Nanopores Equipped with Internal Protein Adaptors. *J. Am. Chem. Soc.* **2015**, *137*, 5793–5797.
- (5) Willems, K.; Van Meervelt, V.; Wloka, C.; Maglia, G. Single-Molecule Nanopore Enzymology. *Philos. Trans. R. Soc., B* **2017**, No. 20160230.
- (6) Moreau, C. J.; Dupuis, J. P.; Revilloud, J.; Arumugam, K.; Vivaudou, M. Coupling Ion Channels to Receptors for Biomolecule Sensing. *Nat. Nanotechnol.* **2008**, *3*, 620–625.
- (7) Reiner, A.; Levitz, J.; Isacoff, E. Y. Controlling Ionotropic and Metabotropic Glutamate Receptors with Light: Principles and Potential. *Curr. Opin. Pharmacol.* **2015**, *20*, 135–143.
- (8) Hernández-Ainsa, S.; Keyser, U. F. DNA Origami Nanopores: Developments, Challenges and Perspectives. *Nanoscale* **2014**, *6*, 14121–14132.

- (9) Lepoitevin, M.; Ma, T.; Bechelany, M.; Janot, J. M.; Balme, S. Functionalization of Single Solid State Nanopores to Mimic Biological Ion Channels: A Review. *Adv. Colloid Interface Sci.* **2017**, *250*, 195–213.
- (10) Sexton, L. T.; Horne, L. P.; Sherrill, S. A.; Bishop, G. W.; Baker, L. A.; Martin, C. R. Resistive-Pulse Studies of Proteins and Protein/Antibody Complexes Using a Conical Nanotube Sensor. *J. Am. Chem. Soc.* **2007**, *129*, 13144–13152.
- (11) Gu, L. Q.; Ding, S.; Gao, C. L. Capturing Single Molecules of Immunoglobulin and Ricin with an Aptamer-Encoded Glass Nanopore. *Anal. Chem.* **2009**, *81*, 6649–6655.
- (12) Yusko, E. C.; Johnson, J. M.; Majd, S.; Prangkio, P.; Rollings, R. C.; Li, J.; Yang, J.; Mayer, M. Controlling Protein Translocation through Nanopores with Bio-Inspired Fluid Walls. *Nat. Nanotechnol.* **2011**, *6*, 253–260.
- (13) Fologea, D.; Ledden, B.; McNabb, D. S.; Li, J. Electrical Characterization of Protein Molecules by a Solid-State Nanopore. *Appl. Phys. Lett.* **2007**, *91*, No. 053901.
- (14) Rocchitta, G.; Spanu, A.; Babudieri, S.; Latte, G.; Madeddu, G.; Galleri, G.; Nuvoli, S.; Bagella, P.; Demartis, M. L.; Fiore, V.; et al. Enzyme Biosensors for Biomedical Applications: Strategies for Safeguarding Analytical Performances in Biological Fluids. *Sensors* **2016**, *16*, 780.
- (15) Van Meervelt, V.; Soskine, M.; Singh, S.; Schuurman-Wolters, G. K.; Wijma, H. J.; Poolman, B.; Maglia, G. Real-Time Conformational Changes and Controlled Orientation of Native Proteins Inside a Protein Nanoreactor. *J. Am. Chem. Soc.* **2017**, *139*, 18640–18646.
- (16) Wada, A.; Mie, M.; Aizawa, M.; Lahoud, P.; Cass, A. E. G.; Kobatake, E. Design and Construction of Glutamine Binding Proteins with a Self-Adhering Capability to Unmodified Hydrophobic Surfaces as Reagentless Fluorescence Sensing Devices. *J. Am. Chem. Soc.* **2003**, *8*, 16228–16234.
- (17) Gilardl, G.; Zhou, L. I. Q.; Hibbert, L.; Cass, A. E. G. Engineering the Maltose Binding Protein for Reagentless Fluorescence Sensing. *Anal. Chem.* **1994**, *66*, 3840–3847.
- (18) Dwyer, M. A.; Hellinga, H. W. Periplasmic Binding Proteins: A Versatile Superfamily for Protein Engineering. *Curr. Opin. Struct. Biol.* **2004**, *14*, 495–504.
- (19) Der, B. S.; Dattelbaum, J. D. Construction of a Reagentless Glucose Biosensor Using Molecular Exciton Luminescence. *Anal. Biochem.* **2008**, *375*, 132–140.
- (20) Solscheid, C.; Kunzelmann, S.; Davis, C. T.; Hunter, J. L.; Nofer, A.; Webb, M. R. Development of a Reagentless Biosensor for Inorganic Phosphate, Applicable over a Wide Concentration Range. *Biochemistry* **2015**, *5054*–5062.
- (21) Tam, R.; Saier, M. H. Structural, Functional, and Evolutionary Relationships among Extracellular Solute-Binding Receptors of Bacteria. *Microbiol. Rev.* **1993**, *57*, 320–346.
- (22) Silva, Z.; Sampaio, M.; Henne, A.; Böhm, A.; Gutzat, R.; Boos, W.; Costa, M. S.; Santos, H. The High-Affinity Maltose / Trehalose ABC Transporter in the Extremely Thermophilic Bacterium *Thermus thermophilus* HB27 Also Recognizes Sucrose and Palatinose. *J. Bacteriol.* **2005**, *187*, 1210–1218.
- (23) Ausili, A.; Staiano, M.; Dattelbaum, J.; Varriale, A.; Capo, A.; D'Auria, S. Periplasmic Binding Proteins in Thermophiles: Characterization and Potential Application of an Arginine-Binding Protein from *Thermotoga maritima*: A Brief Thermo-Story. *Life* **2013**, *3*, 149–160.
- (24) Berntsson, R. P. A.; Smits, S. H. J.; Schmitt, L.; Slotboom, D. J.; Poolman, B. A Structural Classification of Substrate-Binding Proteins. *FEBS Lett.* **2010**, *584*, 2606–2617.
- (25) Quirocho, F. A.; Ledvina, P. S. Atomic Structure and Specificity of Bacterial Periplasmic Receptors for Active Transport and Chemotaxis: Variation of Common Themes. *Mol. Microbiol.* **1996**, *20*, 17–25.
- (26) Radka, C. D.; Labiuk, S. L.; DeLucas, L. J.; Aller, S. G. Structures of the Substrate-Binding Protein YfeA in Apo and Zinc-Reconstituted Holo Forms. *Acta Crystallogr., Sect. D Biol. Crystallogr.* **2019**, *75*, 831–840.
- (27) Millet, O.; Hudson, R. P.; Kay, L. E. The Energetic Cost of Domain Reorientation in Maltose-Binding Protein as Studied by NMR and Fluorescence Spectroscopy. *Proc. Natl. Acad. Sci. U.S.A.* **2003**, *100*, 12700–12705.
- (28) Galenkamp, N. S.; Soskine, M.; Hermans, J.; Wloka, C.; Maglia, G. Direct Electrical Quantification of Glucose and Asparagine from Bodily Fluids Using Nanopores. *Nat. Commun.* **2018**, *9*, No. 4085.
- (29) Ensinger, W.; Ali, M.; Nasir, S.; Duznovic, L.; Trautmann, C.; Toimil-molares, E.; Distefano, G. R.; Laube, B.; Bernhard, M.; Mikosch-Wersching, M.; et al. The INAPO Project: Biomimetic Nanopores for a New Generation of Lab - on - Chip Micro Sensors. *Int. J. Theor. Appl. Nanotechnol.* **2018**, *6*, 21–28.
- (30) Metcalf, W. W.; Wanner, B. L. Mutational Analysis of an *Escherichia coli* Fourteen-Gene Operon for Phosphonate Degradation, Using Tnp_{phoA} Elements. *J. Bacteriol.* **1993**, *175*, 3430–3442.
- (31) Baer, E.; Stanacey, N. Z. Phosphonolipids: I. SYNTHESIS OF A PHOSPHONIC ACID ANALOGUE OF CEPHALIN. *J. Biol. Chem.* **1964**, *239*, 3209–3214.
- (32) Yu, X.; Price, N. P. J.; Evans, B. S.; Metcalf, W. W. Purification and Characterization of Phosphoglycans from *Glycomyces* Sp. Strain NRRL B-16210 and *Stackebrandtia nassauensis* NRRL B-16338. *J. Bacteriol.* **2014**, *196*, 1768–1779.
- (33) Stevenson, K. J.; Gibson, D.; Dixon, G. H. Amino Acid Analyses of Chymotrypsin-Like Proteases From the Sea Anemone (*Metridium senile*). *Can. J. Biochem.* **1974**, *52*, 93–100.
- (34) Nowack, B. Environmental Chemistry of Phosphonates. *Water Res.* **2003**, *37*, 2533–2546.
- (35) Mata, J. M.; Hernandez, S. M. S. Phosphonomycin, a New Antibiotic Produced by Strains of *Streptomyces*. *Science* **1967**, *166*, 20–22.
- (36) Benveniste, E.; Black, R.; Tsai, C.; Follis, K. E.; Sabo, A.; Rice, W. G.; Nat, P.; Sci, A. Prevention of SIV Infection in Macaques by (R)-9-(2-Phosphonylmethoxypropyl)Adenine. *Science* **1995**, *22*, 10–12.
- (37) Racke, K. D. Environmental Fate of Chlorpyrifos. *Rev. Environ. Contam. Toxicol.* **1993**, *131*, 1–150.
- (38) Munro, N. B.; Talmage, S. S.; Griffin, G. D.; Waters, L. C.; Watson, A. P.; King, J. F.; Hauschild, V. The Sources, Fate, and Toxicity of Chemical Warfare Agent Degradation Products. *Environ. Health Perspect.* **1999**, *107*, 933–974.
- (39) Nguyen, Q. H.; Ali, M.; Bayer, V. Charge-Selective Transport of Organic and Protein Analytes through Synthetic Nanochannels. *Nanotechnology* **2010**, *21*, No. 365701.
- (40) Cornelius, T. W.; Apel, P. Y.; Schiedt, B.; Trautmann, C.; Toimil-Molares, M. E.; Karim, S.; Neumann, R. Investigation of Nanopore Evolution in Ion Track-Etched Polycarbonate Membranes. *Nucl. Instrum. Methods Phys. Res., Sect. B* **2007**, *265*, 553–557.
- (41) Papra, A.; Hicke, H. G.; Paul, D. Synthesis of Peptides onto the Surface of Poly(Ethylene Terephthalate) Particle Track Membranes. *J. Appl. Polym. Sci.* **1999**, *74*, 1669–1674.
- (42) Chen, G.; Ma, B.; Wang, Y.; Xie, R.; Li, C.; Dou, K.; Gong, S. CuS-Based Theranostic Micelles for NIR-Controlled Combination Chemotherapy and Photothermal Therapy and Photoacoustic Imaging. *ACS Appl. Mater. Interfaces* **2017**, *9*, 41700–41711.
- (43) Jiang, X.; Zhang, J.; Zhou, Y.; Xu, J.; Liu, S. Facile Preparation of Core-Crosslinked Micelles from Azide-Containing Thermoresponsive Double Hydrophilic Diblock Copolymer via Click Chemistry. *J. Polym. Sci., Part A: Polym. Chem.* **2009**, *46*, 860–871.
- (44) Rizk, S. S.; Cuneo, M. J.; Hellinga, H. W. Identification of Cognate Ligands for the *Escherichia coli* PhnD Protein Product and Engineering of a Reagentless Fluorescent Biosensor for Phosphonates. *Protein Sci.* **2006**, *15*, 1745–1751.
- (45) Alicea, I.; Marvin, J. S.; Miklos, A. E.; Ellington, A. D.; Looger, L. L.; Schreier, E. R. Structure of the *Escherichia coli* Phosphonate Binding Protein PhnD and Rationally Optimized Phosphonate Biosensors. *J. Mol. Biol.* **2011**, *414*, 356–369.
- (46) Gouridis, G.; Schuurman-wolters, G. K.; Ploetz, E.; Husada, F.; Vietrov, R.; De Boer, M.; Cordes, T.; Poolman, B. Conformational

Dynamics in Substrate-Binding Domains Influences Transport in the ABC Importer GlnPQ. *Nat. Struct. Mol. Biol.* **2015**, *22*, 57–64.

(47) Ali, M.; Bayer, V.; Schiedt, B.; Neumann, R.; Ensinger, W. Fabrication and Functionalization of Single Asymmetric Nanochannels for Electrostatic / Hydrophobic Association of Protein Molecules. *Nanotechnology* **2008**, No. 485711.

(48) Siwy, Z.; Gu, Y.; Spohr, H. A.; Baur, D.; Wolf-Reber, A.; Spohr, R.; Apel, P.; Korchev, Y. E. Rectification and Voltage Gating of Ion Currents in a Nanofabricated Pore. *Europhys. Lett.* **2002**, *60*, 349–355.

(49) Lawrence, P. B.; Billings, W. M.; Miller, M. B.; Pandey, B. K.; Stephens, A. R.; Langlois, M. I.; Price, J. L. Conjugation Strategy Strongly Impacts the Conformational Stability of a PEG-Protein Conjugate. *ACS Chem. Biol.* **2016**, *11*, 1805–1809.

(50) Luk, Y. Y.; Tingey, M. L.; Dickson, K. A.; Raines, R. T.; Abbott, N. L. Imaging the Binding Ability of Proteins Immobilized on Surfaces with Different Orientations by Using Liquid Crystals. *J. Am. Chem. Soc.* **2004**, *126*, 9024–9032.

(51) Stone, A. T.; Knight, M. A.; Nowack, B. Speciation and Chemical Reactions of Phosphonate Chelating Agents in Aqueous Media. *ACS Symp. Ser.* **2002**, *806*, 59–94.

4. General Discussion and Conclusion

The functional coupling of a sensor domain with an electrical switch for the detection of small molecules is a major challenge in nanopore based biosensor design¹⁻³ for the development of (portable) devices in medical diagnostics and environmental analysis. Specialized proteins like SBPs or LGICs are predestined to function as such recognition elements, since the high affinity and selective binding of ligands induces a large conformational transition that evolved over billions of years⁴. Moreover, both protein families are able to recognize a variety of different biologically relevant substances like heavy metal ions, pharmaceuticals, neurotoxins (sarin, soman, VX), diagnostic markers (glucose, glutamate) or explosives (TNT)⁴⁻⁷. In the scope of this work, we studied basic aspects of ligand recognition and modulation in GlyRs and NMDARs to further exploit LGICs and SBPs as sensing elements in electrical biosensors with new binding properties for medical and environmental analysis (Fig. 7). Here, we show that i) partial and full agonists induce different conformational transitions in GlyRs that affect apparent affinity and ii) the GluN3A NTD constitutes a crucial role in the glycine-dependent autoinhibition in GluN1/GluN3 NMDARs. We further demonstrated the design of two new classes of biosensors by iii) coupling the ectoine SBP EhuB to the channel pore of GluR0 and iv) by tethering the phosphonate SBP PhnD inside artificial solid state nanopores. In addition, we v) provide evidence for the crucial role of binding domain dimerization in the functional evolution of iGluRs by the fusion of SBPs and potassium channels and vi) expanded the biophysical toolset for the characterization of the structural impacts of ligand-binding in LGICs by thermophoretic analysis of functional solubilized GlyRs in SMA-copolymer nanodiscs.

The direct usage or engineering of LGICs as sensor elements requires a deep mechanistic understanding of ligand recognition and modulation in different receptor subtypes. LGICs recognize a wide range of endogenous ligands, pharmaceuticals and toxins⁸⁻¹⁰, rendering them as a natural occurring electrical screening system with high therapeutic potential. Recent advances in functional and structural studies elucidated remarkable details in the binding mechanism of SBPs and LGICs¹¹. Nevertheless, these findings are only gradually leading to exploitation of LGICs in biosensor design since core aspects in gating of several receptor subtypes and their technical feasibility as biological sensor at the organismic and synthetic level are poorly understood¹²⁻¹⁷. Our results provide a considerable contribution to the mechanistic understanding of receptor gating in the PLGIC and iGluR family by investigating (i) the structural impact and mechanism(s) of full and partial agonism in glycine receptors in its native lipid environment and (ii) the modulatory role of the GluN3A

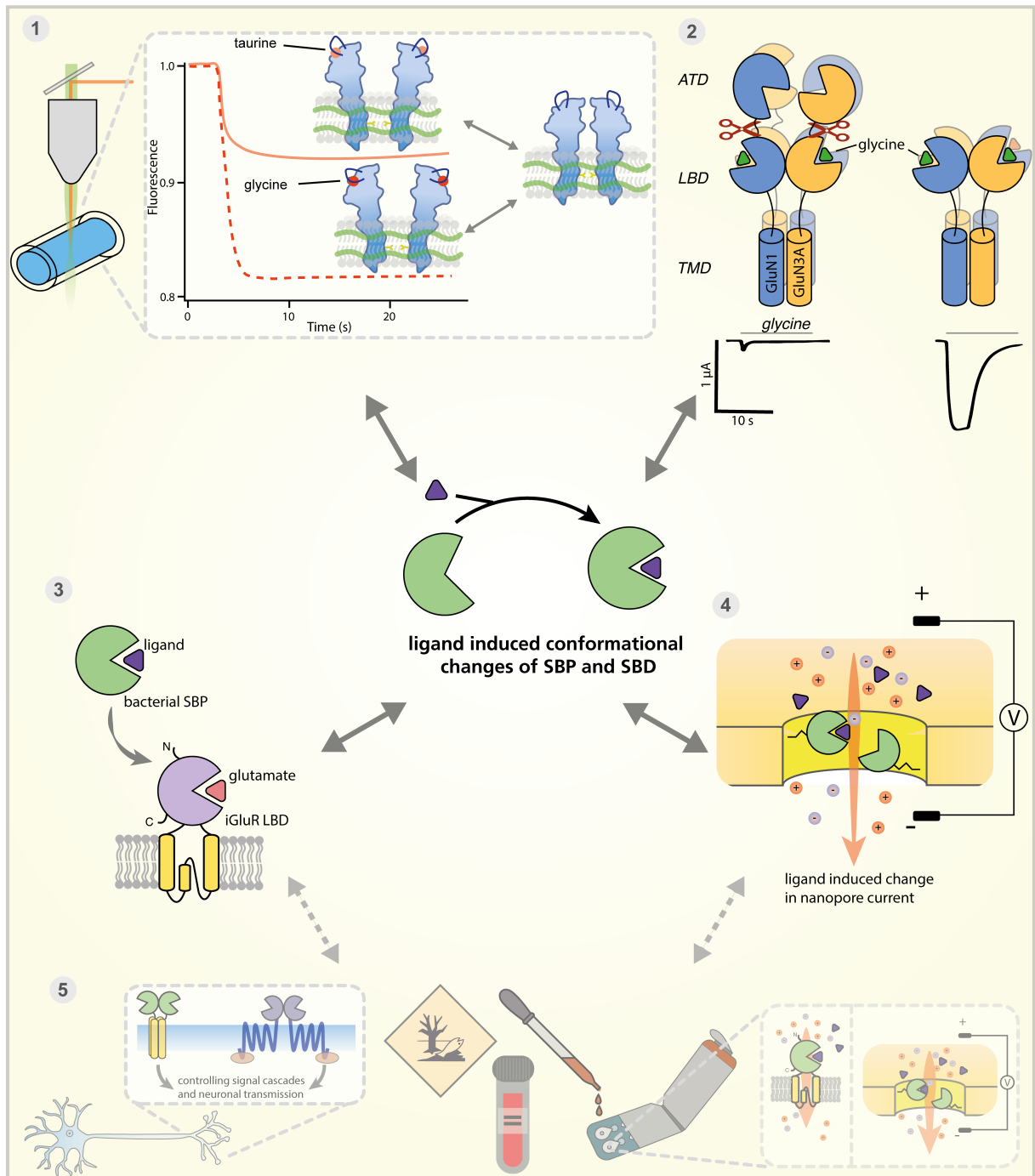


Figure 7. Schematic overview and perspective to study and exploit the ligand induced conformational change of bacterial substrate binding proteins (SBP) and receptor substrate binding domains (SBD) as sensor elements for biological and artificial nanopores. **1** Thermophoretic analysis of the GlyR $\alpha 1$ in SMA-copolymer nanodiscs showed that the full agonist glycine and the partial agonists taurine induced two distinct conformational transitions. **2** Deleting the N-terminal domains (NTDs) of GluN1/GluN3A receptors revealed that the GluN3A NTD has a major role in GluN1/GluN3A receptor regulation by reducing the efficacy of glycine-dependent receptor activation via agonist-evoked auto-inhibition. **3** Design of artificial receptors with new binding properties by fusing the bacterial SBP EhuB to the channel pore of GluR0. **4** Electrical sensing of phosphonates by coupling the phosphonate SBP PhnD to a single solid-state nanopore. **5** Future perspective to use SBP coupled ionotropic and metabotropic receptors to study and control neuronal transmission and

signal cascading at the cellular and organismic level (left) and the utilization of modified receptors and SBP functionalized solid-state nanopores for the development of sensor devices for medical and environmental monitoring (right).

NTD in the glycine dependent GluN1/GluN3 NMDAR auto-inhibition. These functional and structural insights into the mechanisms of activation and modulation in GlyRs and NMDARs might help in the specific design and usage of LGICs as sensors in personal healthcare by detecting therapeutically relevant neurotransmitters and pharmaceuticals, as for instance anesthetics (propofol, ketamine)^{18,19} or neuroprotectants (memantine, ifenprodil)^{20,21}. Furthermore, it may help to enhance the specificity and affinity of these receptors and to eliminate unwanted matrix effects, e.g., caused by the binding of positive and negative (allosteric) modulators, in biological samples.

The demonstrated combination of detergent-free solubilization of functional active receptors with thermophoretic measurements of conformational changes upon ligand binding expands the toolbox of biophysical methods that could lead to novel perspectives in the functional roles of LGICs in physiology and disease and may help in the development of new therapeutics. Since the function of LGICs incorporated into small lipid nanodiscs is preserved, it could be envisioned to couple receptor-SMALPs over reactive polymer side chains²² directly into artificial nanopores that enables their potential usage as biosensors in miniaturized devices. However, the incorporation of LGICs in nanopore systems and the effect of nanodiscs on their ion conductance must remain an active field of research for years to come.

Our results demonstrate that SBPs and LGICs provide an excellent starting point for the development of new classes of electric biosensors. In this work, two proof-of-principle concepts have been demonstrated to use SBPs and SBDs as a molecule detector when connected to an electrical switch by (i) couple the ectoine binding protein EhuB to the channel pore of GluR0 to design receptor-based biosensor with a high efficiency and (ii) coupling the phosphonate binding protein PhnD directly into a solid-state nanopore that combines the high affinity and selectivity of SBPs with the robustness of artificial nanopores. The functional compatibility between SBPs and iGluRs highlight the modular design and role of LBD dimerization in the functional evolution of iGluRs by the fusion of a SBP and an ion channel. This type of artificial receptor with new binding properties enables the specific and concentration dependent detection of ligands in down to a sub-nanomolar range and can be applied in organismic or synthetic systems. This approach could allow the detection of a wide range of compounds that are naturally recognized by type II SBPs²³. In addition, the unique activation mechanism of NMDARs that requires two ligands for activation might be exploited to design two-component sensing systems by exchanging the LBDs of different

NMDAR subtypes with two different SBPs. This would allow the measurement of integrated signals where a current is only given in the presence or absence of a second analyte. In contrast to iGluRs, the venus flytrap domains (VFD) of metabotropic glutamate receptors (mGluRs), metabotropic GABA-B receptors and calcium-sensing G protein-coupled receptors are structural homologous to type I SBPs^{24,25}. Following this strategy, the replacement of the VFD in these G protein-coupled receptor families could be envisioned. This would expand the usage of SBPs coupled receptors to orthogonally control cellular pathways and processes via G proteins^{26,27} as well as the variety of potential detectible ligands.

Although the concept of coupling proteins into solid-state nanopores is not entirely new, most approaches have been aimed to analyze the translocation of large macromolecules, such as DNA or antibodies, through the stochastic sensing of the blocked current by single molecules^{1-3,28,29}. In other approaches binding proteins are electro osmotically captured into biological nanopores for molecule detection^{15,16}. However, these approaches rely on two disadvantages: they either depend on a lipid bilayer and only allow the stable measurement for a few minutes to hours³ or, as in case of solid-state nanopores, they lack the specificity of biological units^{1,2}. The approach demonstrated here, to couple the phosphonate binding protein PhnD into a solid-state nanopore combines the stability of solid-state nanopores with the unique sensing properties of SBPs to analyze small molecules. This hybrid sensor is capable to detect ligand-specific and concentration-dependent changes of phosphonates in a nanomolar range. Since the nanopores are fabricated in PET membranes, they have the potential to be easily interfaced into electronic devices and may allow the fabrication of portable, low-cost sensor systems and multiplex arrays². As mentioned above, due to the diversity of ligand-specific type I and type II SBPs that can be incorporated into solid-state nanopores without major molecular adaptations, this approach has a high potential for the development of robust miniaturized devices.

In conclusion, the ideas described here and the approach to use SBPs and LGICs as sensor domains are an important step towards the specific detection of small molecules and expand the application field of biological and solid-state nanopores. This possibly allows fast and label-free measurements of medically and environmentally important analytes with a proportional, specific and reversible electrical signal and a high signal-to-noise ratio. Beyond that, our approaches enhance the repertoire of biophysical methods for basic and applied science that may help to gain a better understanding of the functions of LGICs at the molecular, synaptic and systemic level.

1. Lepoitevin, M., Ma, T., Bechelany, M., Janot, J. M. & Balme, S. Functionalization of single solid state nanopores to mimic biological ion channels: A review. *Adv. Colloid Interface Sci.* **250**, 195–213 (2017).
2. Dekker, C., Article, R. & Dekker, C. Solid-state nanopores. *Nat. Nanotechnol.* **2**, 209–215 (2007).
3. Willems, K., Meervelt, V. Van, Wloka, C., Maglia, G. & Maglia, G. Single-molecule nanopore enzymology. *Philos. Trans. R. Soc. B-BIOLOGICAL Sci.* **372**, (2017).
4. Rizk, S. S., Cuneo, M. J. & Hellinga, H. W. Identification of cognate ligands for the Escherichia coli phnD protein product and engineering of a reagentless fluorescent biosensor for phosphonates. *Protein Sci.* **15**, 1745–51 (2006).
5. Tam, R. & Saier, M. H. Structural, functional, and evolutionary relationships among extracellular solute-binding receptors of bacteria. *Microbiol. Rev.* **57**, 320–346 (1993).
6. Looger, L., Dwyer, M., Smith, J. & Hellinga, H. Computational design of receptor and sensorproteins with novel functions. *Nature* **423**, 185–190 (2003).
7. Tian, Y. *et al.* Structure-based design of robust glucose biosensors using a Thermotoga maritima periplasmic glucose-binding protein. *Protein Sci.* **16**, 2240–2250 (2007).
8. Traynelis, S. F. *et al.* Glutamate Receptor Ion Channels: Structure, Regulation, and Function. *Pharmacol. Rev.* **62**, 405–496 (2010).
9. Overington, J. P., Al-lazikani, B. & Hopkins, A. L. How many drug targets are there ? *Nat. Rev. Drug Discov.* **5**, 993–996 (2006).
10. Kandel, E. R., Schwartz, J. H., Jessell, T. M. & Professor of Biochemistry and Molecular Biophysics Thomas M Jessell, M. D. *Essentials of Neural Science and Behavior*. (McGraw-Hill, 1995).
11. Plested, A. J. R. Structural mechanisms of activation and desensitization in neurotransmitter-gated ion channels. *Nat. Struct. Mol. Biol.* **23**, 494–502 (2016).
12. Dwyer, M. a. & Hellinga, H. W. Periplasmic binding proteins: A versatile superfamily for protein engineering. *Curr. Opin. Struct. Biol.* **14**, 495–504 (2004).
13. Reiner, A., Levitz, J. & Isacoff, E. Y. Controlling ionotropic and metabotropic glutamate receptors with light: Principles and potential. *Curr. Opin. Pharmacol.* **20**, 135–143 (2015).
14. Moreau, C. J., Dupuis, J. P., Revilloud, J., Arumugam, K. & Vivaudou, M. Coupling ion channels to receptors for biomolecule sensing. *Nat. Nanotechnol.* **3**, 620–625 (2008).
15. Van Meervelt, V. *et al.* Real-Time Conformational Changes and Controlled Orientation of Native Proteins Inside a Protein Nanoreactor. *J. Am. Chem. Soc.* **139**, 18640–18646 (2017).
16. Galenkamp, N. S., Soskine, M., Hermans, J., Wloka, C. & Maglia, G. Direct electrical quantification of glucose and asparagine from bodily fluids using nanopores. *Nat. Commun.* **9**, 1–8 (2018).
17. Moreau, C. J., Niescierowicz, K., Caro, L. N., Revilloud, J. & Vivaudou, M. *Ion channel reporter for monitoring the activity of engineered GPCRs. Methods in Enzymology* **556**, (Elsevier Inc., 2015).
18. Nury, H. *et al.* X-ray structures of general anaesthetics bound to a pentameric ligand-gated ion channel. *Nature* **469**, 428–431 (2011).
19. Pan, J. *et al.* Structure of the pentameric ligand-gated ion channel GLIC bound with anesthetic ketamine. *Structure* **20**, 1463–1469 (2012).
20. Sugaya, N. *et al.* A randomized controlled study of the effect of ifenprodil on alcohol use in patients with alcohol dependence. *Neuropsychopharmacol. Reports* **38**, 9–17 (2018).

-
21. Witt, A., Macdonald, N. & Kirkpatrick, P. Memantine hydrochloride. *Nature Reviews Drug Discovery* **3**, 109–110 (2004).
 22. Lindhoud, S., Carvalho, V., Pronk, J. W. & Aubin-Tam, M. E. SMA-SH: Modified Styrene-Maleic Acid Copolymer for Functionalization of Lipid Nanodiscs. *Biomacromolecules* **17**, 1516–1522 (2016).
 23. Berntsson, R. P. a, Smits, S. H. J., Schmitt, L., Slotboom, D. J. & Poolman, B. A structural classification of substrate-binding proteins. *FEBS Lett.* **584**, 2606–2617 (2010).
 24. O’Hara, P. J. *et al.* The ligand-binding domain in metabotropic glutamate receptors is related to bacterial periplasmic binding proteins. *Neuron* **11**, 41–52 (1993).
 25. Felder, C. B., Graul, R. C., Lee, a Y., Merkle, H. P. & Sadee, W. The Venus flytrap of periplasmic binding proteins: an ancient protein module present in multiple drug receptors. *AAPS PharmSci* **1**, 7–26 (1999).
 26. Alexander, G. M. *et al.* Remote control of neuronal activity in transgenic mice expressing evolved G protein-coupled receptors. *Neuron* **63**, 27–39 (2009).
 27. Pei, Y., Rogan, S. C., Yan, F. & Roth, B. L. Engineered GPCRs as tools to modulate signal transduction. *Physiology* **23**, 313–321 (2008).
 28. Wei, R., Gatterdam, V., Wieneke, R., Tampé, R. & Rant, U. Stochastic sensing of proteins with receptor-modified solid-state nanopores. *Nat. Nanotechnol.* **7**, 257–263 (2012).
 29. Yusko, E. C. *et al.* nanopores with bio-inspired fluid walls. **6**, 253–260 (2011).

III Abbreviations

2-AEP	2-aminoethylphosphonate
AA	amino acids
AMPA	2-Amino-3-(3-hydroxy-5-methyl-isoxazol-4-yl)propanoic acid
ATD	amino terminal domain
BSA	bovine serum albumin
CLR	cys-loop receptor
CLSM	confocal laser scanning microscope
CTD	C-terminal domain
DMAA	N,N-dimethylacrylamide
DNA	deoxyribonucleic acid
ECD	extracellular domain
EMPA	ethylmethylphosphonic acid
EP	ethylphosphonate
GFP	green fluorescent protein
GlyR	glycine receptor
HEK293	human embryonic kidney cell 293
HEPES	2-[4-(2-hydroxyethyl)piperazin-1-yl]ethanesulfonic acid
ICD	intracellular domain
iGluR	ionotropic glutamate receptor
IMPA	isopropylmethylphosphonic acid
LBD	ligand binding domain
LGIC	ligand gated ion channel
MEM	minimum essential media
mGluR	metbotropic glutamate receptor
MST	microscale thermophoresis

NMAS	N-hydroxysuccinimide ester
NMDA	(2R)-2-(Methylamino)butanedioic acid
NTD	N-terminal domain
PBG	phosphate buffered saline with gelatine
PBS	phosphate buffered saline
PDB	protein data bank
PET	polyethylene terephthalate
pLGIG	pentameric ligand-gated ion channel
PMPA	pinacolyl methylphosphonic acid
RMSD	root-mean-square deviation
SBD	substrate binding domain
SBP	substrate binding protein
SD	standard derivation
SDS-PAGE	sodium dodecyl sulphate–polyacrylamide gel electrophoresis
SEM	standard error of the mean
SMA	styrene-maleic acid
SMALP	styrene maleic acid lipid particle
TMD	transmembrane domain
TRAP transporter	tripartite ATP-independent periplasmic transporters
TTT	tripartite tricarboxylate transporters

IV Acknowledgement

Zuallererst möchte ich Prof. Dr. Bodo Laube danken, der mir die Forschung und Promotion an so einem interessanten Thema ermöglicht hat, mir den Freiraum gegeben hat meine eigenen Ansätze zu verfolgen und an meinem Projekt zu wachsen und für die Vielzahl an hilfreichen Denkanstößen und Diskussionen bei scheinbar unlösbaren Problemen und der Verfassung der Manuskripte.

Ich möchte ich Prof. Dr. Gerhard Thiel für die Übernahme des Zweitgutachters, sowie meinen Prüfern danken.

Ich möchte Dr. Mathias Diefenbach und Prof. Dr. Markus Biesalski für die gute Zusammenarbeit im Rahmen des iNAPO Projekts danken.

Des Weiteren möchte ich mich beim Forschungsförderungsprogramm LOEWE des Landes Hessen für die Finanzierung des Projektschwerpunkts iNAPO bedanken, dass mir die Möglichkeit der Erstellung dieser Arbeit ermöglichte.

Ich danke meinen motivierten Bachelor Studenten Dorina, Viktoria und Juliane deren Arbeit ich betreuen durfte.

Ich danke insbesondere meinen Bürokumpanen Raj, Basti und Alex für die unzähligen verrückten Momente und anregenden Gespräche und den restlichen (ehemaligen) AG Mitgliedern Michi, Kai, Gabi, Axel, Selina, Juliane, Nina, Kiki, Vito, Katja und Kirsten für die unvergessliche Zeit in der AG.

Zu aller letzte möchte ich mich bei meinen Eltern, meiner Familie und meinen Freunden, insbesondere Salomé, Tanya, Jascha, Mathias, Marina und Patrick danken, die mich immer über all die Jahre unterstützt und mich in den letzten 5 Jahren auf diesem Weg begleitet haben.